



NCCR QSIT Junior Meeting 2017

Passugg, 12-14 June, 2017



FONDS NATIONAL SUISSE
DE LA RECHERCHE SCIENTIFIQUE

Contact

Heidi Potts
EPFL
Laboratory of Semiconductor Materials
Tel.: +41 21 69 37361
E-Mail: heidi.potts@epfl.ch

Luca Francaviglia
EPFL
Laboratory of Semiconductor Materials
Tel.: +41 21 69 37324
E-Mail: luca.francaviglia@epfl.ch

Cover image: With kind permission of Chur Tourismus (www.churtourismus.ch)

Contents

Contents	3
1 Program	5
2 Abstracts	7
2.1 Mudit Sinhal: <i>“Precision measurements on single molecules using quantum technologies”</i>	8
2.2 Raban Iten: <i>“Quantum Circuits for Quantum Channels”</i>	10
2.3 Giorgio Nicolí: <i>“Transport Spectroscopy of Quantum Dots Coupled to a Fermionic Cavity”</i>	12
2.4 Sigurd Flagan: <i>“Cavity Quantum Electrodynamics with Diamond”</i>	14
2.5 Eric Bonvin: <i>“Near-field Microscopy of Superconducting Single Photon Detectors”</i>	16
2.6 Michael Peper: <i>“Long-range Rydberg molecules bound by electron-atom scattering”</i>	18
2.7 Irene Sanchez Arribas: <i>“Fabry-Perot cavities for enhancing Stokes-anti-Stokes correlations in hexagonal boron nitride”</i>	20
2.8 Natascha Hedrich: <i>“Magnetic Sensing with Single Spins in Diamond”</i>	22
2.9 Roberto Mottola: <i>“Atomic memory for semiconductor quantum dot single photons”</i>	24
2.10 Matthieu Perrenoud: <i>“Supraconducting Nanowire Single Photon Detectors in MoSi”</i>	26
2.11 Barbara Cilenti: <i>“Towards non-destructive, real-time transport measurements of interacting Fermi Gas”</i>	28
2.12 Antonio Ortu: <i>“Broadband Raman Heterodyne Spectroscopy of Rare Earth-doped Crystals for Quantum Memory Applications”</i>	30
2.13 Matteo Soriente: <i>“Two methods analysis of the driven, dissipative Dicke mode”</i>	32
2.14 Dominik Windey: <i>“Levitated Nanoparticles in a Microcavity”</i>	34

2.15	Marius Palm: “Imaging of Current Flow at the Nanoscale”	36
2.16	Tobias Wolf: “Scattering of Dirac Fermions on hexagonal periodic structures in 2D”	38
2.17	Paolo Molognini: “New dynamical phase of matter from parametric driving of a BEC in a cavity” . .	40
2.18	Patrick Knüppel: “Quantum Hall Polaritons”	42
2.19	Roy Haller: “Detection of topological superconductivity via phase tunable noise in Josephson junctions”	44
2.20	Yatu Tsuchimoto: “Quantum interface between single optical and microwave photons”	46
2.21	Fabiana Settembrini: “Correlation measurement of THz photons using GaAs based waveguide”	48
2.22	Manisha Thakurathi: “Floquet Majorana and Para-Fermions in Driven Rashba Nanowires”	50
2.23	Martin Wörnle: “Nanoscale imaging of magnetic structures with a diamond magnetometer”	52
2.24	David Indolese: “Topological states in graphene superconducting hybrid devices”	54
2.25	Carolin Gold: “Spatial Imaging of Electronic States in Cavities using Scanning Gate Microscopy”	56
2.26	Timothy Camenzind: “Towards Majorana Fermions in Graphene Nanoribbons”	58
2.27	Florian Froning: “Hole Spin Qubits in Ge/Si nanowires”	60
2.28	Shima Rajabali: “Graphene cyclotron polaritons and the Dicke Model”	62
2.29	Chiara Decaroli: “A double junction segmented ion trap with integrated optical delivery”	64
2.30	Felix Tebbenjohanns: “Towards Ground State Cooling of Optically Levitated Nanoparticle”	66
2.31	Roland Matt: “Scalable cryogenic experiment for trapped-ion quantum computing”	68
2.32	Felice Appugliese: “Photovoltaic THz photoresponse of high mobility two-dimensional electronic mate- rials due to cyclotron resonance”	70
2.33	Katharina Höveler: “Towards quantum scattering at low collision energies with merged beams”	72
2.34	Ants Remm: “Scaling up a superconducting qubit quantum computer architecture”	74
2.35	Boris Décamps: “EPR steering in a Bose Einstein Condensate”	76
2.36	Aroosa Ijaz: “Realization of an atomically thin mirror using monolayer MoSe ₂ ”	78

Program

	12.06.2016	13.06.2016	14.06.2016
8:00		Breakfast	Breakfast
9:00		Antonio Ortu	Manisha Thakurathi
9:15		Matteo Soriente	Marius Palm
9:30		Dominik Windey	David Indolese
9:45		Martin Wörnle	Carolin Gold
10:00		Tobias Wolf	Timothy Camenzind
10:15		Coffee break	Coffee break
10:45		Paolo Mognini	Florian Froning
11:00		Patrick Knüppel	Shima Rajabali
11:15		Roy Haller	Chiara Decaroli
11:30	Registration	Yatu Tsuchimoto	Felix Tebbenjohanns
11:45		Fabiana Settembrini	Roland Matt
12:30	Lunch	Lunch package	Lunch
13:30	Welcome	Afternoon activities & conference dinner	Felice Appugliese
13:45	Mudit Sinhal		Katharina Höveler
14:00	Raban Iten		Ants Remm
14:15	Giorgio Nicoli		Boris Décamps
14:30	Sigurd Flagan		Aroosa Ijaz
14:45	Eric Bonvin		Closing remarks
15:00	Coffee break		xx:49 Departure
15:30	Michael Peper		
15:45	Irene Sanchez Arribas		
16:00	Natascha Hedrich		
16:15	Roberto Mottola		
16:30	Matthieu Perrenoud		
16:30	Barbara Cilenti		
	Dinner & Poster Session		

Precision measurements on single molecules using quantum technologies

M. Sinhal,¹ K. Najafian,¹ G. Hegi,¹ and S. Willitsch¹

¹*Department of Chemistry, University of Basel, Basel, Switzerland*

The application of coherent quantum manipulations to the spectroscopy of trapped atomic ions has enabled the determination of atomic properties at unprecedented levels of precision¹. Recently, molecules have been proposed as suitable candidates for testing possible time-variation of fundamental constants²⁻⁶, e.g. the m_e/m_p ratio, and enabling long coherence time qubits. We are establishing a complete toolbox for high-precision spectroscopy on molecules, their initialization, manipulation and non-destructive interrogation by entangling them with a co-trapped single atomic ion. To stabilize the necessary laser sources we have set up a frequency-comb stabilization facility. In all of this we will focus on N_2^+ which has recently been identified as a promising candidate system for precision spectroscopy³.

I. INTRODUCTION

It has been theorised that certain fundamental constant could change over time. Studies unifying gravity with the other fundamental forces - electromagnetic, weak and strong point towards a possibility of varying constants⁷. Being the keystones of our physical laws, spatial/temporal variations in fundamental constants would indicate new physics. Experimentally, claims both for and against the variations in α , the fine structure constant, and μ , the proton to electron mass ratio, have been made^{8,9}. Due to their high precision and accuracy, frequency metrology and spectroscopy serve as good test beds for the search of new physics.

We plan to investigate temporal variations in the mass ratio μ by probing molecules¹⁰. Compared to atoms, frequencies of molecular rotational and vibrational transitions show a more prominent dependence on μ , making them better suitable for studying tiny variations of the quantity. We intend to use the highly controlled environments provided by ion traps in order to trap and investigate molecules. Additionally, the same set-up can be used for molecular clocks and quantum information processing using molecules.

II. MOLECULAR SPECTROSCOPY

High precision measurements require transitions to be narrow - which is possible for “forbidden” transitions. Electric dipole allowed transitions are usually too strong and hence exhibit large linewidths which is not suitable for precision studies. We use electric-dipole-forbidden transitions in N_2^+ . Being a homonuclear diatom, N_2^+ has no dipole moment rendering dipole allowed vibrational transitions forbidden. Its simple energy structure, low sensitivity to spurious electromagnetic fields and non-polar nature proves to be of additional advantage, making N_2^+ a good candidate for such studies.⁵

We have developed the theory of hyperfine resolved rovibrational spectra in Hund’s case b molecules to investigate transition frequencies, line-strengths and systematic uncertainties involved in precision spectroscopy

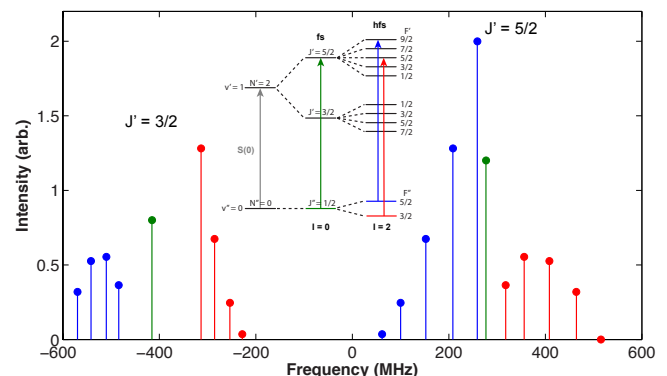


FIG. 1: Relevant transitions and their relative line strengths in the S(0) manifold of the fundamental vibrational transition in N_2^+

of N_2^+ ¹¹. The complete Zeeman Hamiltonian has been solved and transitions insensitive to magnetic field fluctuations have been identified. Such transitions could be measured experimentally to a precision of < 1 Hz provided the system is cooled to the motional ground state and a sufficiently narrow probe laser is used.

III. STATE INITIALIZATION OF N_2^+ IONS

In order to produce N_2^+ in specific rovibrational quantum states, N_2 is ionized from a cold sample using a threshold resonance-enhanced multi-photon ionization (REMPI) technique. This scheme produces N_2^+ with $> 90\%$ state selectivity^{12,13}. We have also developed a general theory describing fine and hyperfine effects in direct ionization and REMPI. The theory not only predicts the hyperfine populations present in photoionized molecular ions, but also predicts the previously observed propensity rule $\Delta J = \Delta F$ ^{14,15}.

We are planning on implementing a hyperfine selective REMPI scheme which would enable us to obtain better statistics in the near future. Once initialized in the correct predetermined state, high precision spectroscopy can be carried out on single N_2^+ molecules.

In order to cool the molecules to the motional ground

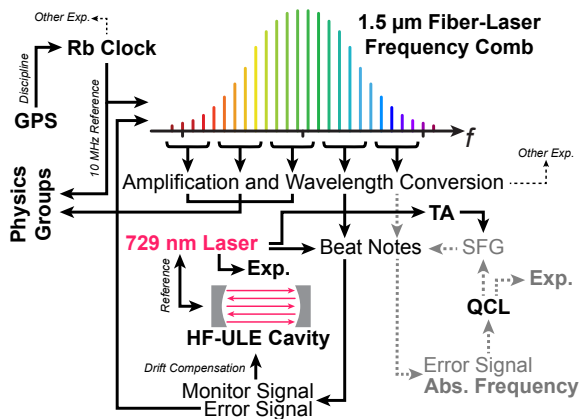


FIG. 2: Stabilization scheme for the lasers and the OFC

state of the ion trap, we trap our molecular ion with a Ca^+ ion. The Ca^+ sympathetically cools the N_2^+ molecules. Ground state cooling minimizes Doppler shifts and opens up the possibility of making non-destructive state readouts.

IV. THE LASER SETUP

We are currently in the process of stabilizing and narrowing the linewidth of our spectroscopic laser, a Mid-IR Quantum Cascaded Laser (QCL) around $4.6\mu m$. The laser is also being referenced to an Optical Frequency Comb (OFC) for absolute frequency determination. The

OFC, centered at $1.5\mu m$, is itself locked to an ultrastable 729nm cavity-stabilized diode laser, thus narrowing the comb lines to $< 5kHz$. Once setup, the QCL will have a linewidth below a few kHz, making it a suitable to drive narrow hyperfine transitions. Fig. 2 shows in detail the stabilization scheme for the OFC, QCL and the 729nm laser.

V. MOLECULAR STATE READOUT

A molecular state detection provides us information if a spectroscopic excitation event was successful. Currently, a destructive state readout scheme based on molecular state dependent chemical reaction is being employed¹². We are currently developing non-destructive readout schemes which would give us better statistics and hence better precision. We plan on cooling the N_2^+ and the Ca^+ to the motional ground state of the ion trap and apply a molecular state dependent optical dipole force to detect spectroscopic events. In the future we plan on implementing quantum phase gates for state detection.

Acknowledgments

This work has been supported by the Swiss National Science Foundation as part of the National Centre of Competence in Research, Quantum Science and Technology (NCCR-QSIT), the European Commission under the Seventh Framework Programme No. FP7 GA 607491 COMIQ, and the University of Basel.

- ¹ P. O. Schmidt, T. Rosenband, C. Langer, W. Itano, J. Bergquist, and D. Wineland, *Spectroscopy using quantum logic*, *Science* **309**, 749 (2005).
- ² S. Willitsch, *Coulomb-crystallised molecular ions in traps: methods, applications, prospects*, *International reviews in physical chemistry* **31**, 175 (2012).
- ³ M. Shi, P. Herskind, M. Drewsen, and I. Chuang, *Microwave quantum logic spectroscopy and control of molecular ions*, *New Journal of Physics* **15**, 113019 (2013).
- ⁴ S. Schiller, D. Bakalov, and V. Korobov, *Simplest molecules as candidates for precise optical clocks*, *Physical review letters* **113**, 023004 (2014).
- ⁵ M. Kajita, G. Gopakumar, M. Abe, M. Hada, and M. Keller, *Test of $m p/m e$ changes using vibrational transitions in $n 2+$* , *Physical Review A* **89**, 032509 (2014).
- ⁶ S. Schiller and V. Korobov, *Tests of time independence of the electron and nuclear masses with ultracold molecules*, *Physical Review A* **71**, 032505 (2005).
- ⁷ J.-P. Uzan, *Varying constants, gravitation and cosmology*, *Living Reviews in Relativity* **14**, 2 (2011), ISSN 1433-8351, URL <http://dx.doi.org/10.12942/lrr-2011-2>.
- ⁸ J. Bagdonaitė, P. Jansen, C. Henkel, H. Bethlem, K. Menten, and W. Ubachs, *A stringent limit on a drifting proton-to-electron mass ratio from alcohol in the early universe*, *Science* **339**, 46 (2013).
- ⁹ J. K. Webb, *Indications of a spatial variation of the fine*

- structure constant*, *Physical Review Letters* **107** (2011).
- ¹⁰ R. Thompson, *The determination of the electron to proton inertial mass ratio via molecular transitions*, *Astrophysical Letters* **16**, 3 (1975).
- ¹¹ M. Germann and S. Willitsch, *Line strengths for fine- and hyperfine-resolved electric-quadrupole rotation-vibration transitions in hund's case b molecules*, *Molecular Physics* **114**, 769 (2016).
- ¹² X. Tong, *Sympathetic cooling of molecular ions in selected rotational and vibrational states produced by threshold photoionization*, *Physical Review Letters* **105** (2010).
- ¹³ M. Germann, X. Tong, and S. Willitsch, *Observation of electric-dipole-forbidden infrared transitions in cold molecular ions*, *Nat Phys* **10**, 820 (2014), URL <http://dx.doi.org/10.1038/nphys3085>.
- ¹⁴ M. Germann and S. Willitsch, *Fine- and hyperfine-structure effects in molecular photoionization. i. general theory and direct photoionization*, *The Journal of Chemical Physics* **145**, 044314 (2016).
- ¹⁵ M. Germann and S. Willitsch, *Fine- and hyperfine-structure effects in molecular photoionization. ii. resonance-enhanced multiphoton ionization and hyperfine-selective generation of molecular cations*, *The Journal of Chemical Physics* **145**, 044315 (2016).

Quantum Circuits for Quantum Channels

Raban Iten,¹ Roger Colbeck,² and Matthias Christandl³

¹*Institute of Theoretical Physics, ETH-Hönggerberg, CH-8093, Zürich, Switzerland*

²*Department of Mathematics, University of York, YO10 5DD, UK*

³*QMATH, Department of Mathematical Sciences, University of Copenhagen, Universitetsparken 5, 2100 Copenhagen, Denmark*

We study the implementation of quantum channels with quantum computers while minimizing the experimental cost, measured in terms of the number of Controlled-NOT (C-NOT) gates required (single-qubit gates are free). We consider three different models. In the first, the Quantum Circuit Model (QCM), we consider sequences of single-qubit and C-NOT gates and allow qubits to be traced out at the end of the gate sequence. In the second (RandomQCM), we also allow external classical randomness. In the third (MeasuredQCM) we also allow measurements followed by operations that are classically controlled on the outcomes. We prove lower bounds on the number of C-NOT gates required and give near-optimal decompositions in almost all cases.

I. INTRODUCTION

Quantum channels, mathematically described by completely positive, trace-preserving maps, play an important role in quantum information theory because they are the most general evolutions quantum systems can undergo. The ability to experimentally perform an arbitrary channel allows in particular to simulate noisy channels. For example, this is useful to test how a new component (e.g., a receiver) will perform when subjected to noise in a more controlled environment. Moreover, experimental groups can show their command over quantum systems consisting of a small number of qubits by demonstrating the ability to perform arbitrary quantum channels on them¹. Instead of building a different device for the implementation of each quantum channel, it is convenient to decompose arbitrary channels into a sequence of simple-to-perform operations. In this paper we work with a gate set consisting of C-NOT and single-qubit gates, which is universal². The implementation of a C-NOT gate is usually more prone to errors than the implementation of single-qubit gates. This motivates using the number of C-NOT gates to measure the cost of a quantum circuit.

In this work we consider the construction of universal circuit topologies comprising gates from this universal set. A circuit topology^{3,4} corresponds to a set of quantum circuits that have a particular structure but in which some gates may be free or have free parameters. Our aim is to find circuit topologies that minimize the C-NOT count but are universal in the sense that any channel from m to n qubits can be obtained by choosing the free parameters appropriately.

We work with three different models. In the first we consider *the quantum circuit model* (QCM), in which we allow a sequence of C-NOT, single-qubit gates and partial trace operations on the qubits and any ancilla. In the second (RandomQCM) we allow the use of classical randomness in addition. In the third (MeasuredQCM), we allow the operations of the QCM as well as measurements and operations that are classically controlled on

the measurement outcomes. Note that this model generalizes the RandomQCM.

A task that is related to the construction of a circuit topology is that of minimizing the C-NOT count for a given quantum channel (on a channel-by-channel basis). Although this appears quite different, we show that it is related in the sense that our lower bounds on the number of C-NOT gates for circuit topologies that are able to generate all quantum channels from m to n qubits are also lower bounds for almost all (in a mathematical sense) m to n channels individually.

II. PREVIOUS WORK

For certain special cases, the theory of decomposing operations is quite developed. Considerable effort has been made to reduce the number of C-NOT gates required in the QCM for general unitary gates⁵⁻¹⁰ and state preparation^{9,11}, which are both examples of a wider class of operations, isometries. Recently, it was shown that every isometry from m to n qubits can be implemented using about twice the C-NOT count required by a lower bound¹². This leads to a method to implement quantum channels using Stinespring's theorem¹³, which states that every quantum channel from m to n qubits can be implemented by an isometry from m to $m+2n$ qubits, followed by tracing out $m+n$ qubits. The isometry can be decomposed into single-qubit gates and 4^{m+n} C-NOTs to leading order¹². Working in the QCM this C-NOT count is optimal up to a factor of about four to leading order¹². However, one can significantly lower this C-NOT count and the required number of ancillas in more general models.

Quantum operations beyond isometries have been investigated by Lloyd and Viola¹⁴. Although they did not focus on a decomposition into elementary gates, combining the decomposition of them with the idea to use binary search¹⁵ and with circuits for isometries¹², leads to low-cost decompositions of quantum channels into single-qubit and C-NOT gates in the MeasuredQCM using only one ancilla qubit. The combination of these papers was

fleshed out recently by Shen *et al.*¹⁶, which appeared shortly after the first version of the present work.

In this work, we give a new decomposition and proof that also leads to near-optimal circuits for quantum channels. In contrast to the work mentioned above, we consider channels that map between spaces with different dimensions. Our decomposition can be used for arbitrary channels from m to n qubits.

III. RESULTS

We give low-cost decomposition schemes for quantum channels from m to n qubits and lower bounds on the number of C-NOT gates in the QCM, the RandomQCM and the MeasuredQCM. Our results are summarized in Table I (where the first row of Table I was already known¹²).

TABLE I: Asymptotic upper and lower bounds on the number of C-NOT gates for m to n channels in the three different models (Model 1: QCM, Model 2: RandomQCM, and Model 3: MeasuredQCM). The total number of qubits required for the constructions is also indicated.

Model	Lower bound	Upper bound	Qubits
1 ¹²	$\frac{1}{4}4^{m+n}$	4^{m+n}	$m + 2n$
2	$\frac{1}{2}2^{2m+n}$	2^{2m+n}	$m + n$
3 ($m < n$)	$\frac{1}{6}(2^{m+n+1} - 2^{2m})$	$m \cdot 2^{2m+1} + 2^{m+n}$	n
3 ($m \geq n$)	$\frac{1}{6}2^{2n}$	$n \cdot 2^{2m+1}$	$m + 1$

Using our decompositions, we derive explicit circuits for channels on a small number of qubits lowering the lowest known C-NOT counts. In fact, we show that every one to two channel can be implemented by 4 C-NOT gates, every two to one channel by 7 C-NOT gates and every two to two channel by 13 C-NOT gates.

IV. DECOMPOSITION SCHEMES

As mentioned in the introduction, one possibility to implement a quantum channel is to use Stinespring's theorem and implement the isometry corresponding to the channel in the QCM¹². However, more general models allow to reduce the required number of C-NOT gates significantly. Our main result is a MeasuredQCM topology for any quantum channel from m qubits to n qubits that uses at most one ancilla and has a low C-NOT count. It decomposes a quantum channel from m to n qubits into a short sequence of m to $m + 1$ isometries (and an additional m to n isometry at the end of the sequence in the case $m < n$). Since this decomposition scheme uses the decomposition of isometries as a black box, it is not restricted to a specific universal gate library and hence we expect it to be useful in a wider range of contexts. For more details about our decomposition schemes, please consider our technical work¹⁷.

Acknowledgments

We acknowledge financial support from the European Research Council (ERC Grant Agreement no 337603), the Danish Council for Independent Research (Sapere Aude), the Innovation Fund Denmark via the Qubiz project and VILLUM FONDEN via the QMATH Centre of Excellence (Grant No. 10059). R.C. acknowledges support from the EPSRC's Quantum Communications Hub. The authors are grateful to Bryan Eastin and Steven T. Flammia, whose package Qcircuit.tex was used to produce the circuit diagrams. We thank Jonathan Home for helpful discussions.

¹ J. T. Barreiro *et al.*, Nature **470**, 486 (2011).

² A. Barenco, C. H. Bennett, R. Cleve, D. P. DiVincenzo, N. Margolus, P. Shor, T. Sleator, J. Smolin, and H. Weinfurter, Phys. Rev. A **52**, 3457 (1995).

³ V. V. Shende, I. L. Markov, and S. S. Bullock, Phys. Rev. A **69**, 062321 (2004).

⁴ V. Shende, I. Markov, and S. Bullock, in *Proceedings of the Design, Automation and Test in Europe Conference and Exhibition*, 2004, p. 980.

⁵ E. Knill, LANL report LAUR-95-2225, arXiv:quant-ph/9508006 (1995).

⁶ A. V. Aho and K. M. Svore, quant-ph/0311008 (2003).

⁷ J. J. Vartiainen, M. Möttönen, and M. M. Salomaa, Phys. Rev. Lett. **92**, 177902 (2004).

⁸ M. Möttönen, J. J. Vartiainen, V. Bergholm, and M. M. Salomaa, Phys. Rev. Lett. **93**, 130502 (2004).

⁹ V. Bergholm, J. J. Vartiainen, M. Möttönen, and

M. M. Salomaa, Phys. Rev. A **71**, 052330 (2005).

¹⁰ V. V. Shende, S. S. Bullock, and I. L. Markov, IEEE Transactions on Computer-Aided Design of Integrated Circuits and Systems **25**, 1000 (2006).

¹¹ M. Plesch and Č. Brukner, Phys. Rev. A **83**, 032302 (2011).

¹² R. Iten, R. Colbeck, I. Kukuljan, J. Home and M. Christandl, Phys. Rev. A **93**, 032318 (2016).

¹³ W. F. Stinespring, Proc. Amer. Math. Soc. **6**, 211 (1955).

¹⁴ S. Lloyd and L. Viola, Phys. Rev. A **65**, 010101(R) (2001).

¹⁵ E. Andersson and D. K. L. Oi, Phys. Rev. A **77**, 052104 (2008).

¹⁶ C. Shen *et al.*, Quantum Channel Construction with Circuit Quantum Electrodynamics, arXiv:1611.03463 (2016).

¹⁷ R. Iten, R. Colbeck, and M. Christandl, arXiv:1609.08103 (2016).

Transport Spectroscopy of Quantum Dots Coupled to a Fermionic Cavity

Giorgio Nicolí,¹ Clemens Rössler,¹ Michael Ferguson,² Oded Zilberberg,² Gianni Blatter,² Thomas Ihn,¹ and Klaus Ensslin¹

¹*Institute for Solid State Physics, ETH, CH-8093, Zürich, Switzerland*

²*Institute for Theoretical Physics, ETH, CH-8093, Zürich, Switzerland*

We have investigated quantum dot-cavity coupled systems through transport spectroscopy experiments performed on a GaAs/AlGaAs heterostructure. The experiments show the possibility of coherently coupling a quantum dot to a fermionic cavity. The Kondo effect has also been taken into account during the investigation, with the results suggesting that the quantum dot-cavity system is coupled in a spin-coherent fashion. The design of the sample also allowed the investigation of a neighboring quantum dots configuration. The results show the establishment of a coherent state extended over the whole system, allowing the coupling of spatially separated quantum dots.

I. INTRODUCTION

Recently, it has been possible to demonstrate the coherent coupling of a quantum dot (QD) defined electrostatically in a two-dimensional electron gas (2DEG) using semiconductor nanostructures, with a fermionic cavity embedded in one of the two leads¹. The results of the performed experiments also hint at spin-coherent dot-cavity coupling. The presented work builds on this previous investigation, utilizing a different sample geometry (FIG. 1). We have analyzed the formation of a quantum dot-cavity hybrid and the interplay between the Kondo² regime and cavity transport in the new sample. Moreover, we have employed the dot-cavity coupling in order to coherently couple two spatially separated QDs. The system has been investigated performing transport spectroscopy experiments at low temperature.

II. EXPERIMENTS

In order to perform transport spectroscopy experiments on dot-cavity hybrid systems, a sample has been fabricated (courtesy of C. Rössler and C. Reichl) on a GaAs/AlGaAs heterostructure, grown by molecular-beam epitaxy. A 2DEG that resides 90 nm below the surface of the sample can be locally depleted by applying a negative voltage to the lithographically defined top-gates. The shape of the gates allows to create confined structures such as QDs, corresponding to the red circles

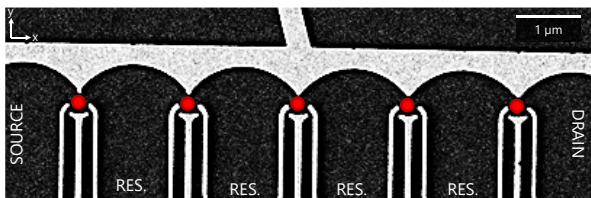


FIG. 1: Top view of the sample: the bright shapes are the lithographically defined gates and the red circles indicate the five distinct QDs available. The labels used for the contacts to the 2DEG are also indicated.

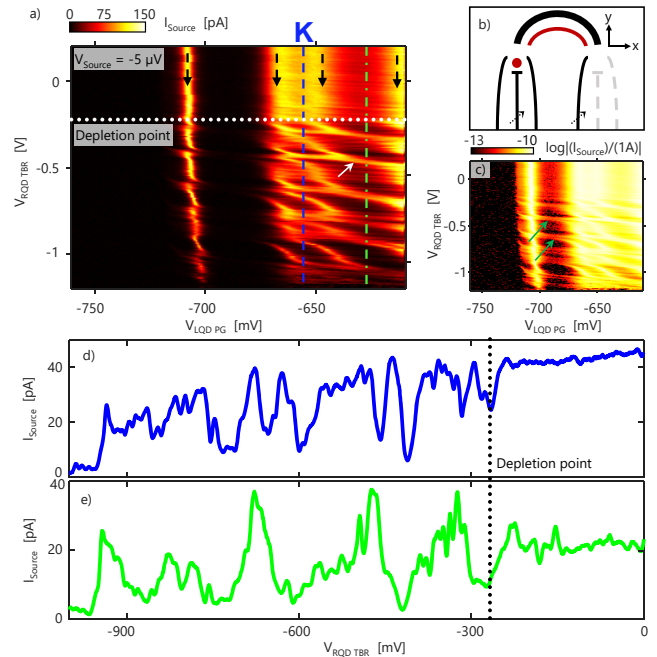


FIG. 2: (a) Current flowing through the dot-cavity system as a function of the PG voltage and of the TB voltage. (b) Schematic sketch of the part of the sample used for this experiment. (c) Same as (a) but in logarithmic scale. (d) Trace taken from (a) at fixed PG bias with the QD in the Kondo regime. (e) Trace taken from (a) at fixed PG bias outside the Kondo regime.

in FIG. 1, and quasi-one-dimensional electronic cavities (running along the arc-shaped gate).

Each QD is defined using the large arc-shaped gates and a group of three finger-like gates, of which the central one is called plunger gate (PG). The PG is used to adjust the energy levels and the size of the QD by applying a negative voltage. The two side gates of each group of three, instead, are used to vary the coupling strength Γ of a dot to the two surrounding leads, by adjusting the associated tunnel barrier (TB). These gates have also been used to form mirrors in order to confine the electrons in the cavity. During the investigation, only limited parts of the sample have been used, containing one or two dots. All the measurements have been performed inside

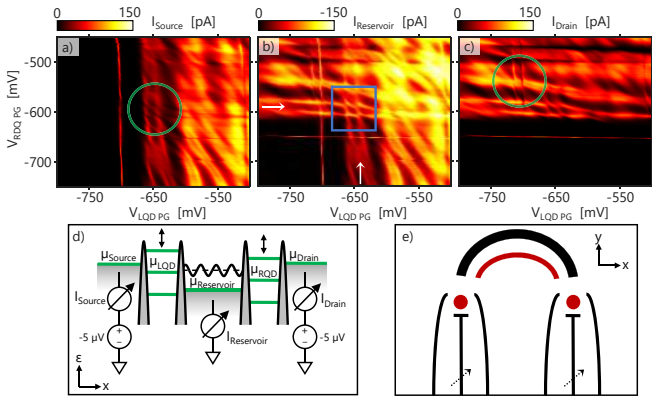


FIG. 3: Transport measurements performed on two neighboring QDs in parallel connection: source current is shown in (a), reservoir current in (b) and drain current in (c). (d) Schematic energy diagram of the investigated system. (e) Sketch of the part of the sample used for the experiments.

a cryogen-free dilution refrigerator at a base temperature of less than 20 mK.

The first step of the investigation has been to increase the coupling of a single QD to the two leads as much as possible. The Kondo effect has been used to probe the coupling strength of a dot to the two leads: the characteristic zero-bias resonance in the conductance through a QD is dependent on Γ and its intensity increases as Γ increases. After tuning the QD into a highly coupled state, the successive step has been to couple it to the cavity. We measured the current flowing through the system, at fixed bias, as a function of both the PG voltage of the dot and of the voltage applied to the TB confining the cavity. The result of this transport measurement through the dot-cavity system is shown in FIG. 2(a).

The plot shows the Coulomb resonances of the QD as vertical lines of enhanced current (black dashed arrows). Additionally, below the depletion point of the TB gate, modulations in the current are observed in the form of diagonal stripes. These lines are identified as cavity modes: the modulation of the density of states in the reservoir influences the transport properties of the dot-cavity system. The plots shown in FIG. 2(d) and (e) are traces taken from the previous plot at constant PG voltage and are used to better observe the modulation introduced by the cavity.

These traces are taken with the dot fixed in the Coulomb blockade regime and interestingly show a different behavior for the Kondo regime (blue trace) and outside the Kondo regime (green line). The cavity is able to suppress Kondo transport and this effect has been understood as a coherent spin-singlet formation in the dot-

cavity system, as it has already been observed in previous publications¹. This confirms the interplay between Kondo effect and dot-cavity hybridization with a different cavity geometry.

Having confirmed that coherent dot-cavity coupling is possible in the investigated sample, we introduced another QD to the system, with the goal of obtaining a coherent state extended over the whole system. This neighboring QD configuration has been investigated in a series and parallel configuration. The result of the transport measurements for the parallel case is shown in FIG. 3. The source and drain leads voltages were both fixed at $-10 \mu\text{V}$. Electrons were injected from both source and drain leads through the (respective) left and right QDs and were collected in the reservoir lead. The current flowing through each of these three leads has been measured independently.

The plots corresponding to source FIG. 3(a) and drain FIG. 3(c) currents show the resonances of the two QDs and, on top of that, it is possible to observe features that are not addressable to a single QD, but are instead caused by the coupling between the two dots. The smoking gun for the establishment of an extended coherent state can be found in the plot corresponding to the reservoir current, FIG. 3(b). In the region highlighted by the blue box, it is possible to observe several anti-crossing features between the resonances of the two QDs. These features are characteristic of strongly coupled systems and confirm the existence of coherent coupling between two spatially separated QDs.

III. OUTLOOK

In the future, it would be interesting to add a magnetic field in order to better investigate the spin properties of the system. Moreover a new and optimized cavity design has been proposed. With this design we aim to have separated experimental parameters to adjust the energy of the cavity levels and the coupling of the QDs to the leads. The phenomenology of the Kondo effect in coupled QDs is another topic that would be interesting to investigate further in the future.

Acknowledgments

We acknowledge the support of the ETH FIRST laboratory and financial support of the Swiss National Science Foundation through the NCCR Quantum Science and Technology grant.

¹ C. Rössler, D. Oehri, O. Zilberberg, G. Blatter, M. Karalic, J. Pijnenburg, A. Hofmann, T. Ihn, K. Ensslin, C. Reichl, et al., *Transport spectroscopy of a spin-coherent dot-cavity system*, Phys. Rev. Lett. **115**, 166603 (2015).

² L. P. Kouwenhoven and L. Glazman, *Revival of the Kondo effect*, Phys. World pp. 33–38 (January 2001).

Cavity Quantum Electrodynamics with Diamond

Sigurd Flågan,¹ Daniel Riedel,¹ Ben Petrak,¹ Patrick Maletinsky,² and Richard Warburton¹

¹*Department of Physics, Nano-photonics Group, University of Basel, CH-4056, Basel, Switzerland*

²*Department of Physics, Quantum Sensing Lab, University of Basel, CH-4056, Basel, Switzerland*

A nitrogen-vacancy (NV) centre in diamond can serve as a source of coherent photons. The photon flux, however, is limited by a long lifetime and poor light extraction efficiency due to the large difference in refractive index across the diamond-air interface. By coupling the NV-centre to a tunable microcavity, we have shown a reduction in lifetime from ~ 12 to ~ 7 ns and an increase in the fraction of coherent photon emission from $\sim 3\%$ to $\sim 46\%$, both clear evidence of the Purcell effect. In addition, recent experimental results show evidence for Purcell enhanced Raman scattering.

I. INTRODUCTION

With no classical analogue, entanglement is one of the most fascinating aspects of quantum mechanics. Entanglement of optical photons allows for fundamental tests of quantum mechanics¹, as well as being a key requirement for many applications in quantum science and technology, such as quantum communication and quantum key distribution (QKD). Advances in photon-photon² or spin-photon³ entanglement allows for advances in long distance quantum communication and remote spin-spin entanglement⁴. However, the limiting factor in these experiments is the rate of entanglement, which depends on the generation of indistinguishable photons. Coupling a solid state quantum emitter⁵ to an optical microcavity can enhance the emission rate of coherent photons.^{6,7}

II. NITROGEN-VACANCY CENTRE

The nitrogen-vacancy (NV) centre is a crystal defect in diamond, consisting of one substitutional nitrogen atom with a vacancy trapped at an adjacent lattice position⁸ (inset Fig.1(a)). When irradiated with a green laser, the NV-centre fluoresces strongly with the zero-phonon line (ZPL) at 637 nm. The ZPL corresponds to a truly electronic transition, implying that the NV-centre can act as a source of indistinguishable photons. However, due to additional phonon contributions, the emission spectrum of the NV-centre has a width of ~ 120 nm⁸.

III. TUNABLE MICROCAVITY

A Fabry-Pérot cavity consists of two highly reflective mirrors, spaced by a distance L . For an ideal cavity, without scattering or absorption, the transmission is described by

$$\mathcal{T} = \frac{1}{1 + (4\mathcal{F}^2/\pi^2) \sin^2(\phi/2)}, \quad (1)$$

where $\phi = 4\pi L/\lambda$ is the round-trip phase shift and \mathcal{F} is the finesse⁹. The transmission is maximised for the resonance condition $L = m\lambda/2$, $m \in \mathbb{Z}_{\geq 0}$, for which the light confined inside the cavity undergoes constructive interference.

The cavity used in our experiments consists of a plano-concave mirror configuration^{10,11} (Fig.1(c)). The concave mirror is fabricated by a CO₂ laser ablation technique on a SiO₂ substrate¹², resulting in an atomically smooth, near-Gaussian depression with a radius of curvature $\lesssim 5 \mu\text{m}$ ¹³. Subsequently, the substrates are coated with a distributed Bragg reflector (DBR) coating to ensure a reflectivity of $>99.9\%$. Piezo electric nanopositioners allow for tuning the cavity *in situ*, as shown in Fig.1(a) and (b) where the diamond is placed inside and outside of the cavity respectively.

IV. SAMPLE FABRICATION

For our experiments we use high-purity single-crystalline CVD-grown diamond, implanted with nitro-

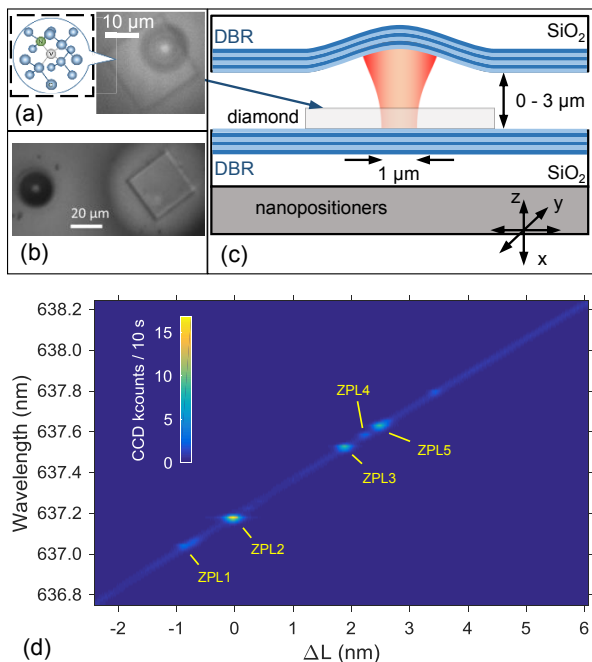


FIG. 1: (a) shows a diamond template located inside the cavity. The inset shows the structure of the NV-centre. (b) diamond placed next to the cavity to demonstrate the lateral tunability. (c) shows a schematic of the design of the microcavity. (d) shows a photoluminescence (PL) spectra of different NV-centres.

gen ions. A multi-step high-temperature annealing process creates close to lifetime limited NV-centres¹⁴. The diamond is structured into small platelets with a thickness of a few μm , using e-beam lithography and inductively coupled plasma reactive ion etching (ICP-RIE). The diamond is then transferred to a Bragg mirror using a micro-manipulator, where it bonds via the van der Waals interaction, provided both surfaces are sufficiently clean.

V. CAVITY QUANTUM ELECTRODYNAMICS

Spontaneous emission of photons is governed by the coupling of an excited quantum system to the electromagnetic vacuum fluctuations. By coupling the emitter to a tunable microcavity, the vacuum fluctuations become confined, and the probability of emitting a photon into the cavity mode is enhanced: the Purcell effect¹⁵.

For a cavity with quality factor Q , the Purcell factor is given by

$$F_P = \frac{3Q\lambda^3}{4\pi^2V_0}, \quad (2)$$

where V_0 is the mode volume. The spontaneous emission coupling factor, $\beta = F_P/(1 + F_P)$, gives the fraction of photons emitted into the cavity mode. The small radii

of curvature mirror produced by Najer *et al.*¹³ allows for a smaller V_0 , and hence a higher Purcell enhancement of photons emitted into the cavity mode.

Due to the large refractive index of diamond, $n = 2.4$, the radiative decay of NV-centres occur predominately into modes propagating latterly in the diamond membrane and the emission of 'useful' photons propagating in vertical modes is weak. In bulk diamond, the radiative lifetime of NV-centres is $\sim 12\text{ns}$. By taking advantage of the Purcell effect, we have shown an reduction in lifetime to 7ns ⁶. The Purcell enhancement of ZPL was found to be ~ 30 , corresponding to an increase in the probability of emission into ZPL from $\sim 3\%$ to $\sim 46\%$ ⁶. The full *in situ* tunability of our microcavity allows for investigation of several different NV-centres, as can be seen in Fig.1(d).

VI. OUTLOOK: PURCELL ENHANCED RAMAN SCATTERING

The Raman effect is the weak inelastic scattering of photons by creation, or absorption, of optical phonons. As previously shown for gaseous systems¹⁶, the rate of Raman scattering can be enhanced by coupling the Raman transition to a tunable microcavity, Purcell enhanced Raman scattering (PERS). Work in progress in our lab have demonstrated PERS from diamond.

-
- ¹ A. Aspect, P. Grangier, and G. Roger, *Experimental realization of Einstein-Podolsky-Rosen-Bohm Gedankenexperiment: a new violation of Bell's inequalities*, Phys. Rev. Lett. **49**, 91 (1982).
- ² H. Bernien, B. Hensen, W. Pfaff, G. Koolstra, M. Blok, L. Robledo, T. Taminiau, M. Markham, D. Twitchen, L. Childress, et al., *Heralded entanglement between solid-state qubits separated by three metres*, Nature **497**, 86 (2013).
- ³ E. Togan, Y. Chu, A. Trifonov, L. Jiang, J. Maze, L. Childress, M. G. Dutt, A. S. Sørensen, P. Hemmer, A. Zibrov, et al., *Quantum entanglement between an optical photon and a solid-state spin qubit*, Nature **466**, 730 (2010).
- ⁴ B. Hensen, H. Bernien, A. E. Dréau, A. Reiserer, N. Kalb, M. S. Blok, J. Ruitenber, R. F. Vermeulen, R. N. Schouten, C. Abellán, et al., *Loophole-free Bell inequality violation using electron spins separated by 1.3 kilometres*, Nature **526**, 682 (2015).
- ⁵ I. Aharonovich, D. Englund, and M. Toth, *Solid-state single-photon emitters*, Nat. Photonics **10**, 631 (2016).
- ⁶ D. Riedel, I. Söllner, B. J. Shields, S. Starosielec, P. Appel, E. Neu, P. Maletinsky, and R. J. Warburton, *Deterministic enhancement of coherent photon generation from a nitrogen-vacancy center in ultrapure diamond*, arXiv:1703.00815 (2017).
- ⁷ L. Greuter, S. Starosielec, A. V. Kuhlmann, and R. J. Warburton, *Towards high-cooperativity strong coupling of a quantum dot in a tunable microcavity*, Phys. Rev. B **92**, 045302 (2015).
- ⁸ C. Kurtsiefer, S. Mayer, P. Zarda, and H. Weinfurter, *Stable solid-state source of single photons*, Phys. Rev. Lett. **85**, 290 (2000).

- ⁹ M. Fox, *Quantum optics: an introduction* (OUP Oxford, 2006).
- ¹⁰ R. J. Barbour, P. A. Dalgarno, A. Curran, K. M. Nowak, H. J. Baker, D. R. Hall, N. G. Stoltz, P. M. Petroff, and R. J. Warburton, *A tunable microcavity*, J. Appl. Phys. **110**, 053107 (2011).
- ¹¹ L. Greuter, S. Starosielec, D. Najer, A. Ludwig, L. Duempelmann, D. Rohner, and R. J. Warburton, *A small mode volume tunable microcavity: development and characterization*, Appl. Phys. Lett. **105**, 121105 (2014).
- ¹² D. Hunger, C. Deutsch, R. J. Barbour, R. J. Warburton, and J. Reichel, *Laser micro-fabrication of concave, low-roughness features in silica*, AIP Adv. **2**, 012119 (2012).
- ¹³ D. Najer, M. Renggli, D. Riedel, S. Starosielec, and R. J. Warburton, *Fabrication of mirror templates in silica with micron-sized radii of curvature*, Appl. Phys. Lett. **110**, 011101 (2017).
- ¹⁴ Y. Chu, N. De Leon, B. Shields, B. Hausmann, R. Evans, E. Togan, M. Burek, M. Markham, A. Stacey, A. Zibrov, et al., *Coherent optical transitions in implanted nitrogen vacancy centers*, Nano letters **14**, 1982 (2014).
- ¹⁵ E. Purcell, *Spontaneous emission probabilities at radio frequencies*, Phys. Rev. **69**, 681 (1946).
- ¹⁶ B. Petrak, N. Djeu, and A. Muller, *Purcell-enhanced Raman scattering from atmospheric gases in a high-finesse microcavity*, Phys. Rev. A **89**, 023811 (2014).

that the helium doesn't boil, eliminating the possibility of bubbles obstructing the optical path.

The SNOM probe consists of a pulled fiber coated in metal, with an aperture of approximately 80nm. The fiber is mounted onto a tuning fork, with a resonance frequency of 32kHz, and a phase-locked loop circuit is used to monitor this frequency. A slight frequency shift is detected when the probe approaches the sample, which allows for precise positioning of the tip. A diagram of the experimental setup is shown in figure 2

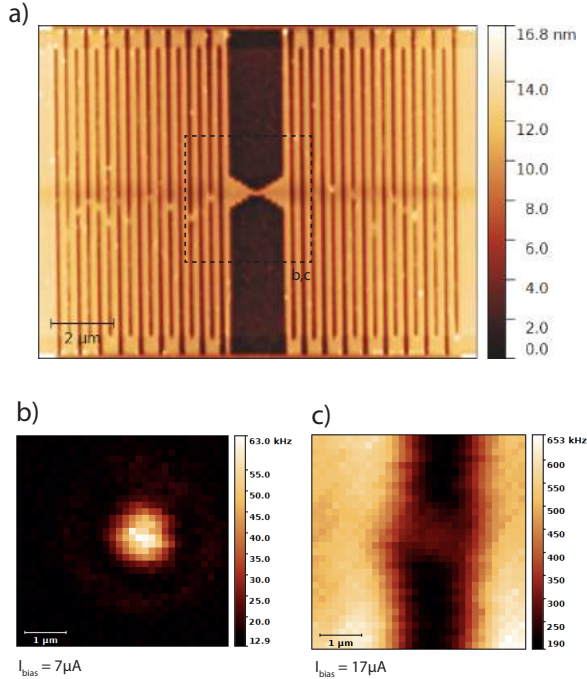


FIG. 3: a) AFM micrograph of a meandering SNSPD with isolated constriction. The nanowires are 200nm wide in the meander, while the constriction is 100nm wide only. b) Confocal map of the area indicated in a). The map indicates the photon counts of nanowire device, biased at $7\mu\text{A}$. Only the narrow constriction detects photons. c) Same scan as in b), but at an increased bias current of $17\mu\text{A}$. Here, only the wider nanowires in the meander detect photons.

III. SAMPLE PREPARATION

The SNSPDs are fabricated using a combination of electron beam lithography and reactive ion etching. Meandering nanowire structures are patterned from a sputtered thin film of NbTiN, resulting in wires 6nm thick and 100nm wide.

Different device geometries are also produced. Most notably, a meandering nanowire with a single constriction has proven to be a useful configuration. By biasing the device at the appropriate current, the active area can essentially be reduced to a point, which is desirable for near-field applications. An atomic force microscopy (AFM) scan of such a device is shown in figure 3a).

IV. PRELIMINARY RESULTS

The behavior of such a constricted nanowire is interesting. The meander has a thickness of 200nm, while the constriction is narrower, at 100nm. When biasing the device slightly below the critical current of the constriction, the current density is too low in the rest of the meander for the superconductivity to breakdown. Therefore, only the constriction is able to detect photons (figure 3b). When increasing the bias current beyond the critical current of the constriction, it becomes resistive and therefore unable to detect photons. However, the meander is now at an appropriate bias current, and the situation is reversed (figure 3c).

We intend to measure the constriction on such devices with a SNOM probe. While approaching the probe to the constriction, we expect to see an exponential increase in photon counts as a result of the detector interacting with the optical near-field. Furthermore, we hope to be able to resolve single nanowires optically, which would yield new insights regarding their detection mechanism.

Acknowledgments

We would like to thank NCCR QSIT and ETHZ for financial support of this project.

¹ G. N. Gol'tsman, O. Okunev, G. Chulkova, A. Lipatov, A. Semenov, K. Smirnov, B. Voronov, A. Dzardanov, C. Williams, and R. Sobolewski, *Picosecond superconducting single-photon optical detector*, Applied Physics Letters **79**, 705 (2001).

² F. Marsili, V. B. Verma, J. A. Stern, S. Harrington, A. E. Lita, T. Gerrits, I. Vayshenker, B. Baek, M. D. Shaw, R. P. Mirin, et al., *Detecting single infrared photons with 93%*

system efficiency, Nature Photonics **7**, 210 (2013).

³ C. M. Natarajan, M. G. Tanner, and R. H. Hadfield, *Superconducting nanowire single-photon detectors: physics and applications*, Superconductor Science and Technology **25**, 063001 (2012), URL <http://stacks.iop.org/0953-2048/25/i=6/a=063001>.

Long-range Rydberg molecules bound by electron-atom scattering

Michael Peper, Heiner Saßmannshausen, Frédéric Merkt, and Johannes Deiglmayr¹

¹Laboratory of Physical Chemistry, ETH Zürich, CH-8093, Zürich, Switzerland

We present recent experimental studies on the formation of long-range molecules in an ultracold Rydberg gas. These studies are conducted using high-resolution photoassociation spectroscopy. In the vicinity of one-photon transitions into $np_{3/2}$ Rydberg states, molecular resonances are observed corresponding to Cs_2 long-range Rydberg molecules originating from the interaction between a Rydberg and a ground-state atom. The interactions are modelled using a Fermi-contact pseudo potential. An extension of a more comprehensive model based on a full electron - ground state R -matrix scattering calculation is presented.

I. INTRODUCTION

In a Rydberg atom, one of the electrons is excited to a state with high principal quantum number n . Atoms in high- n Rydberg states possess unusual properties, such as a large orbital radius (proportional to n^2), a low electron-binding energy ($\propto n^{-2}$), and a long lifetime ($\propto n^3$). These exaggerated, and by their n -dependence tunable properties have long attracted experimental and theoretical interest. In 1934, Amaldi and Segré¹ observed the pressure-dependent shifts and broadenings in Rydberg spectra. The pressure shift results from interactions of the Rydberg electron with ground-state atoms lying inside its large orbit around the ion core, as depicted in Fig. 1. Since the Rydberg electron is slow at its semi-classical turning points, the de Broglie wavelength is large compared to the size of the perturbing ground-state atom. Therefore, a partial-wave analysis can be successfully employed to solve the scattering problem, as only components with small angular momentum contribute. Fermi² modelled this interaction for the s -wave component using a pseudopotential

$$V(\mathbf{R}) = 2\pi a |\Psi(\mathbf{R})|^2, \quad (1)$$

where a is the s -wave scattering length and $|\Psi(\mathbf{R})|^2$ is the probability density of the Rydberg electron at position \mathbf{R} with respect to the ion core.

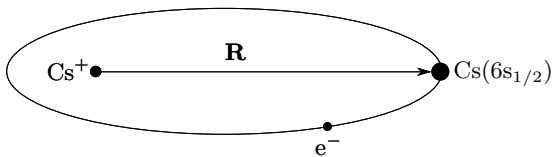


FIG. 1: Rydberg electron e^- with its semi-classical orbit around the Cs^+ ion-core scattering at a $\text{Cs}(6s_{1/2})$ ground-state atom.

As the probability density $|\Psi(\mathbf{R})|^2$ is oscillatory, the interaction potential between a Rydberg atom and a ground-state atom $V(\mathbf{R})$ is also oscillatory, as shown in Fig. 2. As first predicted by Greene et al.³ and first observed by Bendkowsky et al.⁴, these oscillatory potentials may support bound states of long-range diatomic molecules in case of a negative s -wave scattering length.

For the alkali metals, the triplet scattering length is negative while the singlet scattering length is very small or even positive. Omont extended this treatment to include p -wave contributions⁵. Here we will present studies on the formation of long-range Rydberg molecules in an ultracold Rydberg gas using high-resolution photoassociation spectroscopy.

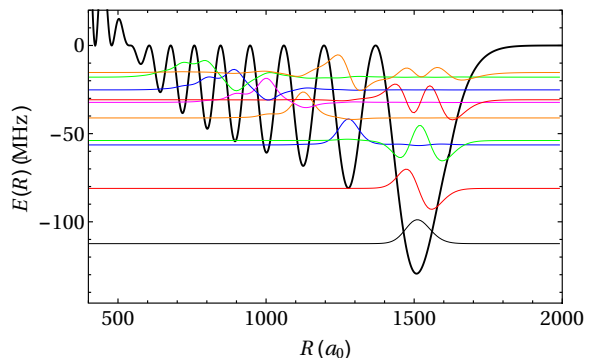


FIG. 2: Vibrational wave functions (coloured lines) in the interaction potential (black line) for the $^3\Sigma$ state dissociating to the $3p_{3/2}, 6s_{1/2}$ asymptote.

II. EXPERIMENTAL

The experiments are conducted on ultracold samples of Cs atoms released from a vapour-loaded compressed magneto-optical trap (MOT). The temperature and density of the sample are estimated from saturated-absorption images of the atom cloud to be $40 \mu\text{K}$ and 10^{11}cm^{-3} , respectively. A single-photon $np_{3/2} \leftarrow 6s_{1/2}$ transition is used to excite $np_{3/2}$ Rydberg states of Cs. The necessary UV radiation is obtained by frequency doubling the output of a single-mode continuous-wave ring dye laser in a doubling cavity. The frequency of the ring dye laser is locked to an external cavity. Frequency drifts are monitored using a wavelength meter, calibrated to a frequency comb. Using electro- and acousto-optic modulators, UV pulses of 2-40 μs are produced. Rydberg atoms and long-range Rydberg molecules are pulsed-field ionized using an extraction field. Cs^+ and Cs_2^+ ions are separated by ion-time-of-flight spectroscopy. The resulting ions and spontaneously formed ions are accelerated

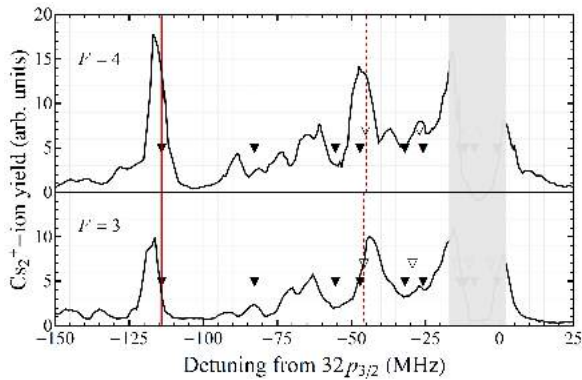


FIG. 3: Cs_2^+ signal at laser frequencies relative to the $np_{3/2}, 6s_{1/2} F = 3, 4$ asymptotes. The solid/dashed red lines correspond to the calculated position of the lowest vibrational level $v = 0$ for the $^3\Sigma/^{1,3}\Sigma$ states. Higher vibrational levels are marked with full/open triangles, respectively.^{7,8}

towards a microchannel plate (MCP) detector. The dynamical evolution of the excited molecular ensemble is studied by varying the delay of the extraction field after laser excitation.

III. RESULTS

A. Determination of scattering lengths

In Fig. 3, a photoassociation spectrum of long-range Cs_2 Rydberg molecules after excitation close to the $32p_{3/2}$ Rydberg state from the $F = 3$ and $F = 4$ hyperfine levels of the $6s_{1/2}$ ground state is shown. The resonances observed at the largest detuning correspond to the most strongly bound molecules in the vibrational ground state of the $^3\Sigma$ potential indicated by a red solid line in Fig. 3. The experiment reveals the existence of another class of molecular states, resulting from the mixing of singlet and triplet scattering channels (labelled as $^{1,3}\Sigma$) by the hyperfine coupling in the ground-state atom, as predicted by Anderson et al.⁶ (red-dashed lines in Fig. 3). Neglecting p-wave contributions, the zero-energy limits of the singlet and triplet scattering lengths are adjusted through a least-squares fit to reproduce experi-

mental binding energies of all $^3\Sigma(v = 0)$ and $^1\Sigma(v = 0)$ levels between $n = 26$ and $n = 34$ within their experimental uncertainties. This constitutes the first experimental determination of the singlet scattering length of low-energy e^- -Cs collisions⁷.

B. Lifetime measurements

The neglected p-wave contribution is known to lower the potential barrier towards smaller internuclear separations R^9 . The excited molecules may therefore decay by tunnelling through the potential barrier. Measurements of the lifetimes of the molecules provide a sensitive probe of the potential energy curve. We observe strongly n -dependent lifetimes of the long-range Rydberg molecules, varying between $0.5 \mu\text{s}$ and $15 \mu\text{s}$ for $n = 32$ and $n = 37$, respectively.

IV. CONCLUSION & OUTLOOK

Long-range Cs_2 Rydberg molecules formed through the interaction of a Rydberg electron and a ground-state atom were observed by photoassociation spectroscopy. The electron - ground-state atom interactions were modelled using a Fermi-contact s-wave scattering pseudopotential. Adjustment of the scattering lengths led to the first experimental determination of the singlet s-wave scattering length. In order to explain the observed molecular autoionisation it is necessary to include higher partial waves in the calculation. We will present our progress towards implementation of a more rigorous description based on a relativistic R -matrix scattering calculation by Bahrim and Thumm¹⁰ as performed by Khuskivadze et al.¹¹.

Acknowledgments

This work is supported financially by the NCCR QSIT and ETH grant No. ETH-22 15-1.

¹ E. Amaldi and E. Segre, *Il Nuovo Cimento* **11**, 145 (1934).

² E. Fermi, *Il Nuovo Cimento* **11**, 157 (1934).

³ C. H. Greene, A. S. Dickinson, and H. R. Sadeghpour, *Phys. Rev. Lett.* **85**, 2458 (2000).

⁴ V. Bendkowsky, B. Butscher, J. Nipper, J. P. Shaffer, R. Löw, and T. Pfau, *Nature* **458**, 1005 (2009).

⁵ A. Omont, *J. Phys. (Paris)* **38**, 1343 (1977).

⁶ D. A. Anderson, S. A. Miller, and G. Raithel, *Phys. Rev. A* **90**, 062518 (2014).

⁷ H. Saßmannshausen, F. Merkt, and J. Deiglmayr, *Phys.*

Rev. Lett. **114**, 133201 (2015).

⁸ H. Saßmannshausen, J. Deiglmayr, and F. Merkt, *Eur. Phys. J. Special Topics* **225**, 2891 (2016).

⁹ M. T. Eiles and C. H. Greene, *Phys. Rev. A* **95**, 042515 (2017).

¹⁰ C. Bahrim and U. Thumm, *Phys. Rev. A* **61**, 022722 (2000).

¹¹ A. A. Khuskivadze, M. I. Chibisov, and I. I. Fabrikant, *Phys. Rev. A* **66**, 042709 (2002).

Fabry-Perot cavities for enhancing Stokes–anti-Stokes correlations in hexagonal boron nitride

Irene Sánchez Arribas,¹ Nikolaus Flöry,¹ Achint Jain,¹ Markus Parzefall,¹
 Sebastian Heeg,¹ Kenji Watanabe,² Takashi Taniguchi,² and Lukas Novotny¹

¹Photonics Laboratory, ETH Zürich, CH-8093, Zürich, Switzerland

²National Institute for Materials Science, 1-1 Namiki, Tsukuba, Ibaraki, 305-0044 Japan

We present our design of Fabry-Perot cavities of hexagonal boron nitride (h-BN) sandwiched between two metallic mirrors. The planar microcavity modifies the photonic mode density of h-BN compared to its value in free space and can be tuned in such a way that the Raman scattering cross section is enhanced, increasing the probability of observing correlated Stokes–anti-Stokes photon pairs.

I. INTRODUCTION

Raman scattering is a powerful tool mostly used to study the vibrational modes of a system. It can be presented in two forms, the Stokes (S) and anti-Stokes (aS) process, where the incoming photon loses (gains) energy by creating (absorbing) a phonon, respectively¹. Klyshko² introduced a third process in which the incoming photon is absorbed in a Stokes process by a phonon and the phonon is subsequently annihilated to create an anti-Stokes photon, resulting in a Stokes–anti-Stokes (SaS) correlated photon pair as shown schematically in Figure 1. Systems presenting the SaS process are of particular interest as the character of the correlation can be continuously varied from purely quantum to classical³ and have also been proven to be a potential solid state quantum memory⁴.

In order to observe the SaS process at room temperature, one needs phonons with energy $\hbar\Omega_G$ higher than the thermal energy $k_B T$ so that the phonon occupation number $\eta_0 = 1/(\exp(\frac{\hbar\Omega_G}{k_B T}) - 1)$ is low. In this way, the spontaneous aS process is rare and correlations between S and aS phonons can be observed. Several materials such as diamond and graphene fulfill these conditions and have already been demonstrated as sources of SaS photons^{3–5}.

However, even if the material satisfies the above conditions, the probability of observing the SaS process is still very low due to the low Raman scattering cross section. To increase it, one needs to use either pulsed lasers where the instantaneous number of photons is extremely high as Kasperczyk et al.³ and Lee et al.⁴ did in diamond or by resonance engineering. In this last approach, one could use a few-milliwatt continuous wave laser by bringing the system in resonance with the aS process as demonstrated by Jorio et al.⁵ in twisted bilayer graphene.

Another interesting candidate for the generation of SaS photons is hexagonal boron nitride (h-BN), since it has a Raman active high energy optical phonon at 1364 cm^{-1} with a low occupation number at room temperature of $\eta_0 = 0.0014$. Moreover, it is a van der Waals material and its atomic flatness makes it a good candidate for building up planar microcavities that can be used to enhance the different Raman processes by optical resonance

engineering.

The goal of this work is to fabricate and characterize high quality Fabry-Perot (FP) cavities using different thicknesses of h-BN. Finally, we will choose cavity designs that can selectively enhance the S or aS processes in h-BN.

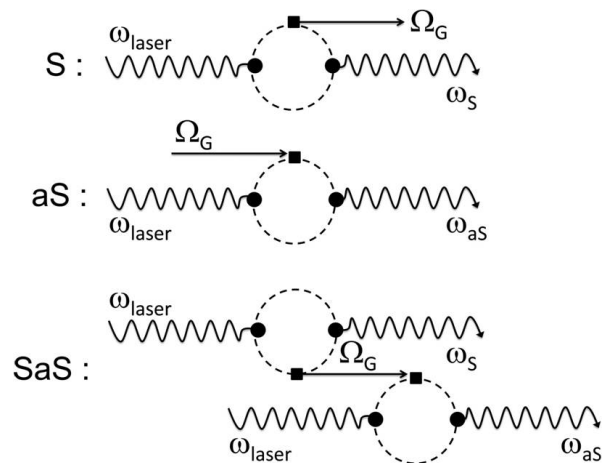


FIG. 1: Feynman diagrams for three different Raman scattering processes. Wavy and straight arrows stand for photons and phonons, respectively, while the dashed circles represent electron-hole pairs. Black dots and black squares represent electron-photon and electron-phonon interactions. S stands for Stokes Raman process, aS for anti-Stokes Raman process, and the last diagram, named here SaS, represents the generation of a Stokes and anti-Stokes photon pair via creation and annihilation of the same phonon. Figure and caption taken from Ref. 5.

II. FABRY-PEROT CAVITY DESIGN

We study planar microcavities formed by two metallic mirrors separated by a h-BN flake. We address cavities with metallic mirrors because of their easy implementation, but in principle other structures such as distributed Bragg reflectors could be used as well. The transmittance of the microcavities is modeled using the transfer matrix method⁶.

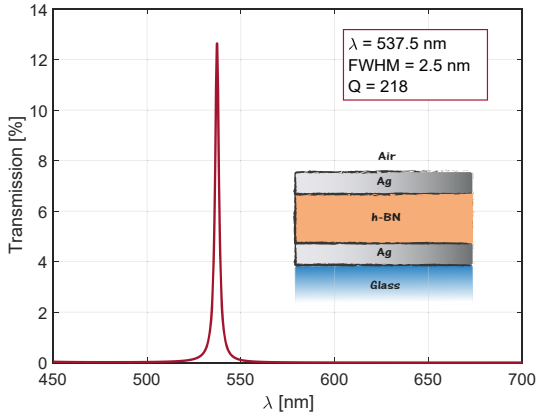


FIG. 2: Simulated transmission spectra of the Air/silver/h-BN/silver/glass structure depicted in the inset. Both silver mirrors have a thickness of 60 nm and the h-BN is 350 nm thick. Air and glass are treated as semi-infinite mediums. The resonance wavelength is 537.5 nm and the FWHM is 2.5 nm, corresponding to a Q factor of 218.

The resonant modes of the cavity will be at wavelengths in which the phase change accumulated in the cavity in a round trip is equal to a multiple of 2π :

$$2m\pi = \frac{4\pi n_c L_c \cos \theta}{\lambda} + \sum_i \Delta\phi_i(d_i, \theta, \lambda) \quad (1)$$

where m is an integer, n_c and L_c stand for the refractive index and thickness of the cavity (h-BN), θ is the angle of the incident light, λ the wavelength in vacuum, and $\Delta\phi_i$ the phase change due to reflection at the respective mirror of thickness d_i .

Since the cross-section of Raman scattering in h-BN does not vary appreciably as a function of wavelength, we focus on resonance wavelengths between 500 and 600 nm

to optimize detection efficiency of our Raman setup. Furthermore, in order to achieve selectivity of the aS mode, the full width at half maximum (FWHM) $\Delta\lambda$ of the cavity resonance has to be smaller than the phonon energy. This adds the constraint of a cavity with FWHM smaller than 30 nm for the aforementioned wavelength values. Figure 2 shows the simulated transmittance spectrum of a potential cavity candidate formed by two silver mirrors of 60 nm thickness and a h-BN flake of 350 nm. We select silver for the mirrors because of its high reflectivity in the desired range. Simulations show that in order to achieve high quality factor $Q \sim \lambda/\Delta\lambda$ values the mirror thickness has to be in the range from 50 to 60 nm.

The samples will be fabricated by mechanical exfoliation of h-BN flakes onto SiO_2 substrate using the scotch tape method. Subsequently, silver will be evaporated on top of the structure and template stripping will be performed, ensuring an ultraflat surface at the mirror/h-BN interface. Finally, a second silver mirror will be evaporated on top of the surface.

III. CONCLUSION AND OUTLOOK

We have discussed the fabrication of Fabry-Perot cavities with embedded h-BN in order to enhance the Stokes-anti-Stokes process so far never observed in this material. Once the cavities have been fabricated and proven to be successful, we will perform cross-correlation measurements to reveal the quantum or classical nature of the produced Stokes-anti-Stokes photon pairs.

Acknowledgments

We would like to thank QSIT for the financial support.

¹ A. Jorio, *Raman spectroscopy in graphene related systems* (Wiley-VCH, Weinheim, 2011), ISBN 978-3-527-40811-5.

² D. N. Klyshko, *Correlation between the Stokes and anti-Stokes components in inelastic scattering of light*, Soviet Journal of Quantum Electronics **7**, 755 (1977), ISSN 0049-1748.

³ M. Kasperczyk, A. Jorio, E. Neu, P. Maletinsky, and L. Novotny, *Stokes-anti-Stokes correlations in diamond*, Optics Letters **40**, 2393 (2015), ISSN 1539-4794.

⁴ K. C. Lee, B. J. Sussman, M. R. Sprague, P. Michelberger, K. F. Reim, J. Nunn, N. K. Langford, P. J. Bustard, D. Jaksch, and I. A. Walmsley, *Macroscopic non-*

classical states and terahertz quantum processing in room-temperature diamond, Nature Photonics **6**, 41 (2012), ISSN 1749-4885.

⁵ A. Jorio, M. Kasperczyk, N. Clark, E. Neu, P. Maletinsky, A. Vijayaraghavan, and L. Novotny, *Optical-Phonon Resonances with Saddle-Point Excitons in Twisted-Bilayer Graphene*, Nano Letters **14**, 5687 (2014), ISSN 1530-6984.

⁶ S. J. Byrnes, *Multilayer optical calculations*, arXiv:1603.02720 [physics] (2016), arXiv: 1603.02720, URL <http://arxiv.org/abs/1603.02720>.

Magnetic Sensing with Single Spins in Diamond

Natascha Hedrich,¹ Patrick Appel,¹ Brendan Shields,¹ and Patrick Maletinsky¹

¹Quantum Sensing Group, Universität Basel, CH-4096, Basel, Switzerland

Due to their excellent coherence properties and high magnetic field sensitivity, single spin defects in diamond, in particular Nitrogen-Vacancy (NV) centers, have recently emerged as a promising platform for imaging magnetic fields¹. Here, we explore NV center magnetometry of magnetic structures down to monolayer sensitivities. In particular, we show how to use these sensors to measure the magnetic domains of ferromagnetic thin film materials such as in-plane demagnetized Co/Pt stacks. Similar thin-films have been shown to contain magnetic skyrmions, potentially important components of future spintronic devices, in ambient conditions², making these films of great technological interest.

I. INTRODUCTION

In recent years, the development of crystal defects in diamond as high precision magnetic field sensors has led to exciting new revelations in materials physics^{3,4}. The Nitrogen Vacancy (NV) center has emerged as a particularly promising quantum sensor for imaging magnetic structures such as domain walls⁵ and skyrmions⁶, which are of great interest in the search for new forms of magnetic memories⁷. Due to their quantum-coherent manipulation, long coherence times⁸, and high magnetic field and spatial resolutions⁹, NV centers may be applied to determine the dynamics of such magnetic structures - an aspect that is of fundamental interest in nanomagnetism.

II. EXPERIMENTAL BACKGROUND

NV centers are atom-like defects in diamond composed of a substitutional nitrogen atom and an adjacent lattice vacancy (Figure 1a). Negatively charged NV's have been studied particularly intensely in recent years due to their stable $S=1$ electronic spin triplet ground state, which can be prepared and read out optically. The triplet ground (and excited) states are spanned by $|m_s = 0, \pm 1\rangle$ basis states, where m_s is the magnetic quantum number along the NV spin quantization axis. As illustrated in Figure 1b, the NV ground state can be non-resonantly excited with a 532 nm laser via spin-preserving optical transitions to the vibrational sideband of the excited states (green). The $|0\rangle$ excited state primarily decays radiatively, while the $|\pm 1\rangle$ excited states can decay (non-radiatively) to an intermediate, metastable singlet state. The singlet state then primarily decays to the $|0\rangle$ ground state, resulting in two important facts: the NV can be initialized into the $|0\rangle$ state via spin pumping, and the NV fluorescence is state-dependent. Thus, we can optically distinguish between the $|0\rangle$ and $|\pm 1\rangle$ states, which yield 'bright' and 'dark' fluorescence respectively.

In the absence of a magnetic field, the $|\pm 1\rangle$ states are degenerate, and split by 2.87 GHz from the $|0\rangle$ state. The $|0\rangle \rightarrow |\pm 1\rangle$ transitions can be driven with a microwave for resonant population transfer. Applying a magnetic

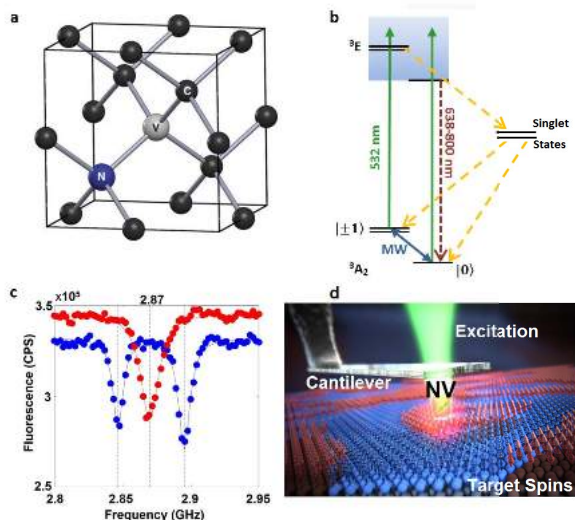


FIG. 1: **The Nitrogen Vacancy (NV) defect in diamond**
a The diamond crystal lattice containing an NV center defect. The NV spin quantization axis lies along the line connecting the nitrogen and vacancy (Figure adapted from [8]). **b** Electronic states of the NV center. Indicated are the non-resonant ground state excitations (in green) used for spin initialization and readout, as well as the radiative (dashed red) and non-radiative (dashed yellow) decay channels. The blue arrow indicates the $|0\rangle \leftrightarrow |\pm 1\rangle$ microwave transition. **c** Two ESR spectra measured at 0 G (red) and 8.6 G (blue). The two transitions $|0\rangle \rightarrow |+1\rangle$ and $|0\rangle \rightarrow |-1\rangle$ are identified by two dips in the fluorescence. **d** The NV is embedded near the tip of a diamond pillar-cantilever structure, which is scanned over the sample. A microwave loop is placed near the NV to resonantly drive the $|0\rangle \rightarrow |\pm 1\rangle$ transitions and the spin state is initialized and read out via a green excitation laser.

field lifts the $|\pm 1\rangle$ degeneracy due to a Zeeman splitting of 2.87 MHz/G. Therefore, when the microwave frequency matches the $|0\rangle \rightarrow |\pm 1\rangle$ transitions, population is pumped out of $|0\rangle$ and the NV fluorescence decreases, a condition denoted by electron spin resonance (ESR). At zero magnetic field, we thus see a fluorescence dip at microwave frequencies of 2.87 GHz. Conversely, when the NV is exposed to external magnetic fields, the single dip splits into two at the $|0\rangle \rightarrow |-1\rangle$ and $|0\rangle \rightarrow |+1\rangle$ transition frequencies. This splitting can thus be used

to quantitatively determine the magnetic field via ESR measurements. Two example ESR spectra are shown in Figure 1c, where the NV fluorescence is plotted as a function of microwave frequency. The zero field ESR is shown in red, and a spectrum at 7 G (blue) shows a splitting of 20 MHz.

To harness the magnetic field response of the NV fluorescence for magnetic imaging, we use two techniques to probe the Zeeman splitting as the NV is scanned over the sample. First, by applying a fixed-frequency microwave drive, we can image iso magnetic field lines on our sample. Alternatively, by recording the full ESR spectrum at each point, we can extract a full field map from the splitting between the two dips. In order to increase optical addressability, the NV is embedded in the tip of a diamond pillar-cantilever structure as shown in Figure 1d. This structure allows for easy optical access, as well as simple, AFM-style scans. These combined factors yield the excellent performance of NV magnetometry, necessary for imaging nanoscale magnetic spin structures, discussed in the following.

III. RESULTS

Based on the principles described above, we present imaging of domain patterns of ferromagnetic thin-film materials. In particular, we examined a stack of 50nm Pt/ 0.6 nm Co/ 2 nm Pt deposited on a sapphire substrate. The moment of the magnetic Co layer are oriented orthogonal to the sample plane. At a domain wall, the stray field is maximal as the field curls at this point, resulting in a large overlap with the NV symmetry axis. In our experiments, we perform a dual iso B scan at 17 G and 12.5 G over a $3 \times 3 \mu\text{m}$ scan region to obtain two pairs of lines shown in Figure 2, around each domain wall. We also performed a full field scan over a small region of the domain wall (inset of Figure 2). This high resolution, quantitative scan can ultimately be used to determine the magnetization of the sample, which is an important parameter in characterizing magnetic materials. Preliminary estimates indicate a magnetization of $M_s = 1.12 \times 10^6$ A/m.

IV. DISCUSSION AND OUTLOOK

In this work, we have demonstrated our ability to image the magnetic domains of a Co/Pt thin film. This

material is particularly important as a first step towards imaging a very closely related material, Ir/Co/Pt, which has been shown to contain skyrmions at room temperature under ambient conditions². Imaging these structures will help us to better understand their spin-texture, allowing skyrmions to be integrated into future spintronic devices. Eventually, we aim at measuring skyrmion dynamics in these thin films, an experiment which will be enabled by the long coherence times and fast coherent manipulation of NV centers. Such experiments would be a large step towards developing the technology necessary to realize smaller, more efficient magnetic memories.

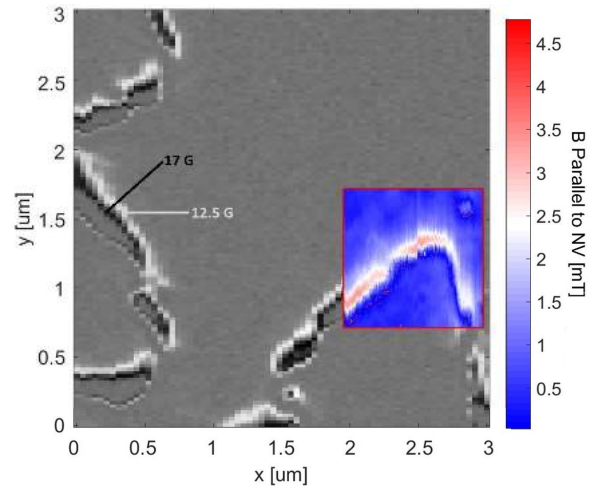


FIG. 2: **Domain structures** A dual-iso B scan, in which the 12.5 G and 17 G iso magnetic field lines have been extracted. The inset shows a portion of the domain wall, which has been imaged in detail by taking an ESR spectrum at each point. The resultant magnetic field amplitude is indicated by the color bar on the right.

Acknowledgments

We would like to acknowledge the support of QSIT, the Swiss National Science Foundation and the EU FET project, DIADEMS. Furthermore, we would like to thank Prof. Hans-Josef Hug and Dr. Mirko Bacani at EMPA for providing the samples.

¹ P. Maletinsky et al, Nat. Nano. **12**, 1578 (2012).

² M. Baćani et al (2016), arXiv: 1609.01615.

³ T. van der Sar et al, Nat. Comm. **6**, 8886 (2015).

⁴ C. Du et al (2016), arXiv: 1611.07408.

⁵ J. Tetienne et al, Nat. Comm. **6**, 7733 (2015).

⁶ Y. Dovzhenko et al (2016), arXiv: 1611.00673.

⁷ A. Fert et al, Nat. Nano. **8**, 152 (2013).

⁸ N. Bar-Gill et al, Nat. Comm. **4**, 1743 (2013).

⁹ P. Appel et al, NJP **17**, 112001 (2015).

Atomic memory for semiconductor quantum dot single photons

Roberto Mottola,¹ Janik Wolters,¹ Gianni Buser,¹ Andrew Horsley,¹ Lucas Béguin,¹ Andreas Jöckel,¹ Jan-Philipp Jahn,¹ Richard J. Warburton,¹ and Philipp Treutlein¹

¹*Department of Physics, University of Basel, Klingelbergstrasse 82, CH-4056 Basel, Switzerland*

Quantum memories matched to single photon sources will be essential for the development of quantum networks and quantum information processing. We demonstrate a quantum memory in warm Rb vapor with on-demand storage and retrieval based on electromagnetically induced transparency. The implemented memory is compatible with single photons emitted by semiconductor quantum dots, having a bandwidth on the order of 100 MHz. Using attenuated laser pulses on the single-photon level the principle of operation of the memory is demonstrated. For a storage time $T = 50$ ns an end-to-end efficiency $\eta_{e2e} = 3.4(3)\%$ of the memory setup is achieved, with an intrinsic storage and retrieval efficiency $\eta_{int} = 17(3)\%$.

I. INTRODUCTION

Quantum information science is a rapidly advancing field, whose principles are currently being implemented in real-world applications. For example, quantum communication enables the creation of unconditionally secure links across the globe¹, and linear optical quantum computation promises exponential speed-ups in evaluating complex problems². Secure quantum communication has already been demonstrated³. However, it is limited to relatively short distances due to losses in fibers and noise in the system (~ 100 km). To overcome these limitations, quantum repeaters⁴ have been proposed: long distance entanglement is established through successive entanglement swapping between adjacent nodes, allowing transmission of a quantum state to a remote receiver through quantum teleportation. Each of these nodes consists of a single photon source and a *quantum memory* (QM): a device that can store and retrieve a quantum state of light on-demand.

Two important metrics for the performance of quantum nodes are the rate at which the entanglement between two nodes can be established, and the coherence time of the stored quantum information. Relying on a single system for both the source and the memory means making a trade-off in performance.

Heterogeneous quantum nodes consisting of a single-photon source and a compatible QM are highly promising. The two systems can be completely different and therefore individually optimizable. Combining the best of different systems, such as the high-speed, on-demand photon generation of semiconductor *quantum dots* (QDs) and the long coherence times of atomic systems, could lead to great advantages⁵. Furthermore, these QDs can emit indistinguishable single photons, which are the prerequisite for several quantum information processing protocols⁶.

Warm vapors of alkali atoms have several advantages for the storage of light. Vapor cells are relatively cheap and easy to use since they require neither an ultra-high vacuum environment, nor cryogenics nor laser cooling. Furthermore, the cells are robust and high optical depths on the order of thousands⁷ can be achieved.

While wavelength matching to QDs has been successfully accomplished⁸, the remaining challenge of a QD compatible memory is to achieve the required acceptance bandwidth of 100 MHz, which is rather large compared to the intrinsic alkali D lines (~ 5 MHz). To achieve this we proposed⁹ and are implementing¹⁰ a high-speed quantum memory based on *electromagnetically induced transparency* (EIT) in warm Rb vapour.

II. STORAGE & RETRIEVAL

EIT is a nonlinear optical phenomenon that occurs in ensembles of atoms with a three level Λ -scheme and long lived ground states. The weak signal field, which carries the quantum information, couples the ground state $|g\rangle$ to the excited state $|e\rangle$. Through a strong control field, which couples the second ground state $|s\rangle$ to $|e\rangle$, the propagation of the signal field through the EIT medium is manipulated. In fact, if both fields are near-resonant with the atomic transition, the different pathways for the absorption of the light interfere destructively opening a transparency window, allowing signal photons to pass through the atomic medium without absorption.

Through EIT the signal field experiences an increase of normal dispersion and thus a coherently controlled decrease of the group velocity. This slowdown can be used as a protocol for QMs. In fact, when the signal pulse is inside the medium and the control laser intensity is adiabatically decreased the group velocity goes to zero, closing the EIT window and storing the signal field. As this is a unitary evolution, as follows from time reversal symmetry, the signal can be retrieved by simply turning on the control field again.

The system is prepared by optically pumping the atoms into the ground state $|g\rangle$ with the control laser. The signal is stored as a collective excitation of the atoms of the EIT medium¹¹. Considering a single photon signal field, after storage, the atoms are in a superposition of the two ground-states $|g\rangle$ and $|s\rangle$ with a single shared excitation.

We present a quantum memory using the ⁸⁷Rb D₁ line at 795nm (see Fig.1(a)). The atoms were initially prepared in the $F = 1$ hyperfine state of the $5^2S_{1/2}$ ground

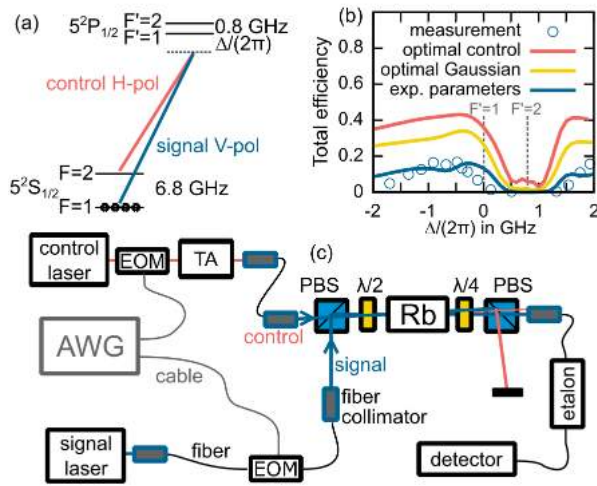


FIG. 1: (a) Energy levels of the ^{87}Rb D₁ line and transitions involved in the memory scheme. Both lasers are slightly detuned by Δ . (b) Measured and computed internal efficiency in dependency of the detuning Δ , for the control pulses used in the experiment, Gaussian pulses and optimal control pulses. (c) Experimental setup.

state manifold by optical pumping. As a signal field we used weak coherent pulses, generated by a laser red detuned by $\Delta = -2\pi \cdot 0.9$ GHz from the $F = 1 \rightarrow F' = 1$ transition of the ^{87}Rb D₁ line. The control laser was detuned by Δ from the $F = 2 \rightarrow F' = 1$ transition.

For the proof-of-principle setup we used weak coherent pulses generated by modulating an attenuated laser with an *electro-optic modulator* (EOM) driven by a fast *arbitrary waveform generator* (AWG). Similarly, the control pulses are generated by a second laser that gets modulated and subsequently amplified by a *tapered*

amplifier (TA). The amplified spontaneous emission introduced by the TA is suppressed with a monolithic filter cavity. A great challenge in quantum memory experiments is the separation of the weak signal from the strong control field. By using polarization filtering, spatial filtering through a single mode fiber and a slight 10(1) mrad misalignment of the beams, and spectral filtering with an etalon we achieved a suppression of 12 orders of magnitude (120 dB) for the control beam, while the signal was attenuated by only 4.8 dB. After a storage time $T = 50$ ns we applied a second identical control pulse for retrieval. We obtained an internal efficiency $\eta_{int} = 17(3)\%$ and an end-to-end efficiency $\eta_{e2e} = 3.4(3)\%$, which describe the ratio of output to input energy, i.e. the re-emission probability of the stored photon, considering only the memory itself or the whole setup, respectively. The measured internal efficiency corresponds to the predicted values computed for the experimental parameters (see Fig.1(b)).

III. OUTLOOK

Achieving storage and retrieval of true single photons emitted by a QD source will be the focus of our future work. Further improvements of this proof-of-principle work can be accomplished by some straightforward implementations such as: a control field with higher power to enhance the intrinsic efficiency, an optimized filtering system, using anti-relaxation coated vapor cells for improved pumping efficiency, increasing the beam diameters (and thus the interaction volume) for an extended storage time, and using a magnetic shielding to reduce the ground state decoherence. Furthermore, exploiting the Zeeman substructure of the atoms will significantly increase the efficiency.

- ¹ L.-M. Duan, M. Lukin, J. I. Cirac, and P. Zoller, *Long-distance quantum communication with atomic ensembles and linear optics*, Nature **414**, 413 (2001).
- ² E. Knill, R. Laflamme, and G. J. Milburn, *A scheme for efficient quantum computation with linear optics*, Nature **409**, 46 (2001).
- ³ B. Korzh, C. C. W. Lim, R. Houlmann, N. Gisin, M. J. Li, D. Nolan, B. Sanguinetti, R. Thew, and H. Zbinden, *Provably secure and practical quantum key distribution over 307 km of optical fibre*, Nature Photonics **9**, 163 (2015).
- ⁴ H.-J. Briegel, W. Dür, J. I. Cirac, and P. Zoller, *Quantum Repeaters: The Role of Imperfect Local Operations in Quantum Communication*, Physical Review Letters **81**, 5932 (1998).
- ⁵ N. Sangouard, C. Simon, J. Minář, H. Zbinden, H. De Riedmatten, and N. Gisin, *Long-distance entanglement distribution with single-photon sources*, Physical Review A **76**, 050301 (2007).
- ⁶ N. Somaschi, V. Giesz, L. De Santis, J. C. Loredano, M. P. Almeida, G. Hornecker, S. L. Portalupi, T. Grange, C. Anton, J. Demory, et al., *Near optimal single photon sources*

in the solid state, Nature Photonics **10**, 1 (2015).

- ⁷ K. F. Reim, J. Nunn, V. O. Lorenz, B. J. Sussman, K. C. Lee, N. K. Langford, D. Jaksch, and I. A. Walmsley, *Towards high-speed optical quantum memories*, Nature Photonics **4**, 218 (2010).
- ⁸ J.-P. Jahn, M. Munsch, L. Béguin, A. V. Kuhlmann, M. Renggli, Y. Huo, F. Ding, R. Trotta, M. Reindl, O. G. Schmidt, et al., *An artificial Rb atom in a semiconductor with lifetime-limited linewidth*, Physical Review B **92**, 245439 (2015).
- ⁹ M. T. Rakher, R. J. Warburton, and P. Treutlein, *Prospects for storage and retrieval of a quantum-dot single photon in an ultracold ^{87}Rb ensemble*, Physical Review A - Atomic, Molecular, and Optical Physics **88**, 1 (2013).
- ¹⁰ J. Wolters, G. Buser, A. Horsley, L. Béguin, A. Jöckel, J.-P. Jahn, R. J. Warburton, and P. Treutlein, *Simple atomic quantum memory suitable for semiconductor quantum dot single photons* (2017), URL arXiv:1703.00489.
- ¹¹ A. I. Lvovsky, B. C. Sanders, and W. Tittel, *Optical quantum memory*, Nature Photonics **3**, 706 (2009).

Supraconducting Nanowire Single Photon Detectors in MoSi

Matthieu Perrenoud,¹ Misael Caloz,¹ Claire Autebert,¹ and Hugo Zbinden¹

¹*Group of Applied Physics - Quantum Technologies,
University of Geneva, CH-1211, Geneva, Switzerland*

We design, build and characterize Supraconducting Nanowire Single Photon Detectors (SNSPDs) for application in quantum key distribution . . .

I. INTRODUCTION

Supraconducting Nanowire Single Photon Detectors (SNSPDs) constitute a key technology for the development of quantum communication and computation. Their low dead time and dark count rate, combined with a high efficiency and small jitter favour the use of this technology in applications such as Quantum Key Distribution (QKD), quantum optics and communication¹, and long-distance ground-to-space optical communications².

Amorphous materials such as WSi and MoSi are particularly desirable for the fabrication of SNSPDs due to their high degree of homogeneity and uniformity over large areas. Due to the lack of a well-defined crystal structure, amorphous superconductors can be deposited on virtually any substrate without significant degradation in material properties. Thus, SNSPDs fabricated from these materials can easily be embedded inside of a dielectric optical stack to enhance absorption at a particular wavelength. High efficiencies have been reported with WSi (90%)³ and MoSi (87%)⁴.

In this work, we present the progress on the development of single photon detectors based on superconducting nanowires made from amorphous MoSi as well as the investigation of the nanoscale detection mechanism in MoSi nanowire SNSPDs.

II. DEVICE FABRICATION

A. Design

The nanowire is designed as squared shape meander of size $16 \times 16 \mu\text{m}$ (Figure 1). The meander shape allows for a large surface area to be covered by the wire while keeping its width below 200nm. Different nanowire with and fill factors are tested in order to optimize the detector efficiency. To increase the system detection efficiency, an optical cavity optimized for our wavelength is also added to our design using an Ag mirror and a top layer of TiO_2 . The final design including the nanowire, the cavity, as well as contact electrodes is made in a lollipop shape, allowing for easy electrical and optical connection.

B. Nanofabrication

The fabrication of the device takes place in the clean room facilities of the center of micro and nanotechnologies (CMI) at the Swiss Federal Institute of Technology, Lausanne (EPFL).

In order to create an optical cavity to enhance the absorption probability in the nanowire, an Ag mirror is first deposited on a silicon wafer with dry silicon oxide. On top of the mirror, a thin layer of $\text{Mo}_{0.8}\text{Si}_{0.2}$ is deposited in the University of Basel by sputtering. The supraconducting nanowire is then created by EBeam Lithography and dry etching. Gold contact pads contacting the nanowire are deposited by evaporation. The nanowire is encapsulated with silicon oxide and the cavity closed with a top layer of TiO_2 . Each individual nanowire is finally separated from the wafer with deep reactive ion etching (DRIE) in a lollipop shape. This final mechanical shape allows for the self-alignment of the device into an optical fiber mating sleeve as well as the wire bonding of the contact pads to a standart SMA connector.

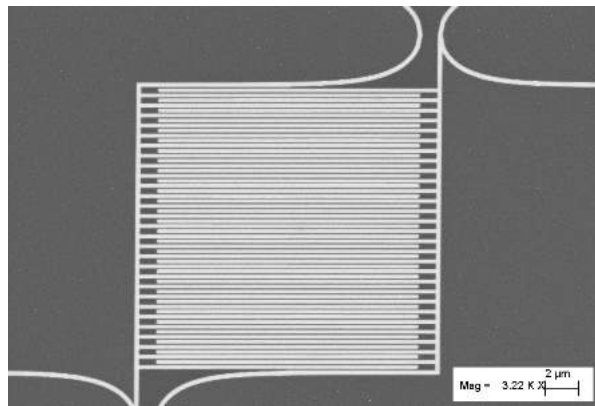


FIG. 1: SEM image of the $16 \times 16 \mu\text{m}$ nanowire during the fabrication process

C. Packaging

After fabrication, the detector is placed on a specifically designed holder allowing for easy electrical connection to an SMA connector via wire bonding. The lollipop shape of the design let the bonding be performed at a distance from the nanowire to avoid potential damage during the bonding process.

III. MEASUREMENT SETUP

The photon detection is characterized using a 1500nm CW laser. Three EXFO attenuators are used in order to decrease the laser power to a mean photon number of 100'000 photons. The measurement is performed at cryogenic temperature (0.75K), and the polarization of incident light is optimized to maximize the detector counts. The system detection efficiency (SDE) (i.e, the number of detections per 100'000 incident photons) is one of the key properties of the detector to optimize and is characterized as the number of counts per 100'000 photons versus the bias current of the nanowire. Efficiency of different nanowire designs including different fill factor, nanowire width, and optical cavities are fabricated and tested. Other important information such as timing jitter and detector dead time are also investigated and rely on the readout electronics as much as the actual detector design.

IV. RESULTS

A good detector should exhibit an efficiency saturation when increasing the bias current, before reaching the critical current of the superconducting material. Such plateau is observed in most of our designs, with best efficiencies reaching an SDE of above 80% at 0,75K. Figure 2 shows the SDE and dark count rate (DCR) as a function of bias current.

Jitter measurement on the same generation of devices show a jitter around 30ps to 40ps. The dead time of the

detectors is estimated to be in the order of few tens of nanoseconds.

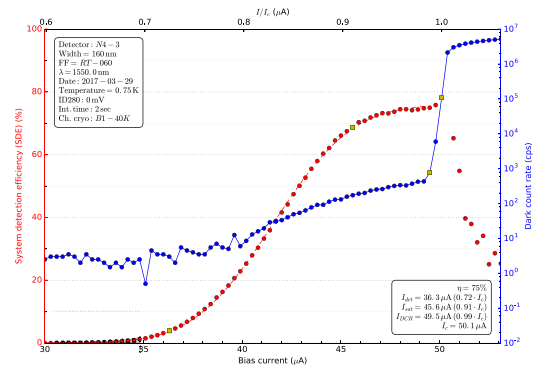


FIG. 2: SDE vs increasing current bias. A saturation plateau is reached above $45\mu A$

V. DISCUSSION

Current investigation aims at achieving better efficiencies using an optical cavity optimized for our 1550nm laser. This could also allow for high efficiencies with lower fill factor, potentially leading to nanowire designs with higher critical current. Improvement of the readout electronics for jitter and count rate optimization planned as well. Other more exotic nanowire shapes are also investigated.

¹ C. Zinoni, B. Alloing, F. Li, A. Marsili, L. Fiore, L. Lunghi, A. Gerardino, Y. B. Vakhtomin, K. Smirnov, and G. Goltsman, *Single-photon experiments at telecommunication wavelengths using nanowire superconducting detectors*, Appl. Phys. Lett **91**, 031106 (2007).

² M. E. Grein, A. J. Kerman, E. A. Dauler, O. Shatrovov, R. J. Molnar, D. Rosenberg, J. Yoon, C. E. DeVoe, D. V. Murphy, B. Robinson, et al., *Design of a ground-based optical receiver for the lunar laser communications demonstration*, Int. Conf. Sp. Opt. Syst. Appl. **78** (2011).

³ F. Marsili, V. B. Verma, J. A. Stern, S. Harrington, A. E. Lita, T. Gerrits, I. Vayshenker, B. Baek, M. D. Shaw, R. P. Mirin, et al., *Detecting single infrared photons with 93% system efficiency*, Nat. Photonics **7** (2013).

⁴ V. B. Verma, B. Korzh, F. Bussieres, R. D. Horansky, D. Dyer, A. E. Lita, I. Vayshenker, F. Marsili, M. D. Shaw, H. Zbinden, et al., *High-efficiency superconducting nanowire single-photon detectors fabricated from mosi thin-films*, Opt. Express **23**, 33729 (2015).

Towards non-destructive, real-time transport measurements of interacting Fermi Gas

Barbara Cilenti,¹ Kevin Roux,¹ Oscar Bettermann,¹ Victor Helsen,¹ and Jean-Philippe Brantut¹

¹*Institute of physics, École Polytechnique Fédérale de Lausanne, 1015 Lausanne, Switzerland*

We are setting up a new experiment using ultracold ⁶Li atoms to study transport properties of mesoscopic channels. The novelty of the experiments is in the implementation of a non-destructive measurement procedure by means of a high-finesse cavity. In the following abstract I will first give a short description of the planned experimental setup, with a focus on the high finesse cavity design and then describe the first tests that has been performed on it and the current status of the experiment.

I. INTRODUCTION

Over the last decades an intensive research has been conducted on ultracold atoms, inspired by their good isolation from the environment and ease in manipulation. As a result a very high degree is now accessible, including the tuning of inter-atomic interactions, the possibility to organize them in defined geometrical patterns or in lower dimensions. For these reasons, ultracold atoms can simulate a large variety of many-body quantum system that cannot be studied theoretically directly¹ Among the open problems in many-body physics, the study of the transport properties has gained popularity in the past years, and several experiments have been realized to study the phenomenon under different perspectives. In particular, simulation of conductance in mesoscopic devices has been performed, by connecting two macroscopic reservoirs of ultracold fermions via a channel and observing the current induced by a controlled unbalance of the two reservoirs².

The aim of the experiment that is currently being set up in Lausanne is to push forward the exploration of this aspect by integrating a high finesse cavity in the experimental set-up to perform non-destructive measurements³. This will allow us to observe the dynamic of the system in real time, enhancing the sensitivity usually limited by the noise associated to the preparation of a new sample after each measurement.

II. PRINCIPLE

Consider a probe beam with frequency ν_l , resonant with the cavity. The atomic cloud is composed of identical copies of a single two-level system with energy spacing $h\nu_0$, as in Fig.1.

If the beam is detuned from the transition by Δ , with Δ very large, the cloud will act as a dispersive medium modifying the phase of the probe beam without altering the state of the single atoms. By performing an interferometric measurements on the probe beam, we are inferring information on the atoms distribution. Since the state of the atoms is not altered, the measurement is non-destructive.

In order to make the effect of the atoms on the probe beam significant, is necessary to work in a strong cou-

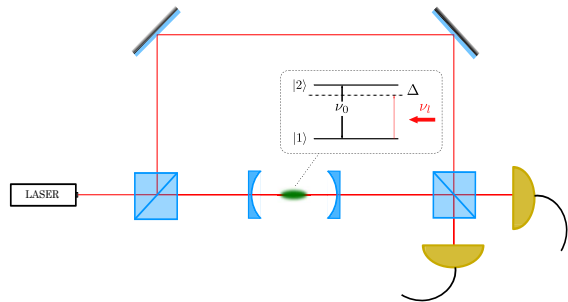


FIG. 1: Schematic setup for non-destructive measurement. If the detuning Δ is sufficiently large, the probe beam which passes through the atomic sample experiences a phase shift measurable with an interferometric measurement.

pling regime. This is achieved by building cavity with high Finesse. Indeed, it can be shown that for a fixed destructivity of the measurement, the signal to noise ratio increases like the square root of the Finesse.

Working with a high finesse cavity imposes stringent constraints on the mechanical stability of the experimental setup.

III. EXPERIMENTAL SETUP

In order to perform a non-destructive measurement we need

- a stable cavity with a high finesse
- an atomic sample produced at its center

The last requirement is achieved by trapping and manipulating the atoms directly inside the cavity, which is placed in the main chamber. The atomic species selected for the experiment is the fermionic isotope ⁶Li and the procedure for the coolind down and trapping of the atoms is similar to the one performed in other ultracold atoms experiments⁴.

The main chamber has a lot of optical access to allow the entrance of the laser beams for the cooling/trapping procedure, for the non-destructive measurement procedure and for the production of optical lattices along different directions. On the top and bottom of the chamber there are two re-entrant viewports with $NA \sim 0.56$, for high resolution imaging of the atomic sample and for the projec-

tion of optical potentials. The magnetic fields for all the stages of the experiment are provided by different sets of coils located around the main chamber and outside the re-entrant viewports.

In order to fulfill the conditions on the cavity, both the optical and the mechanical properties have been designed accurately.

IV. OPTICAL AND MECHANICAL DESIGN OF THE CAVITY

TABLE I: Expected parameter for the high finesse cavity at the three wavelength of interest. The 671nm source will be employed in the cooling down procedure and as the probe beam for the atoms in the cavity. The 1064nm source is for the dipole trap, and the 532nm is the lock reference for the cavity length.

Wavelength	532/1064nm	671nm
Length	4 cm	
Radius of curvature	2.5cm	
FSR	3.75GHz	
Finesse	3000	50000

As mentioned before, a high finesse is fundamental in order to make the effect of the interaction between the probing field and the atomic sample measurable. For this purpose mirrors with low losses must be selected. In table I are shown the chosen parameters. To ensure the stability of the cavity length, each mirror is attached to a piezoelectric actuator which will allow to compensate the effect of long term drifting. The voltage signal of the piezos will be controlled via a Pound-Drever-Hall lock scheme⁵ involving the 532nm laser beam.

The cavity could be made unstable also by the coupling with environmental vibrations which can propagate through the support holding the vacuum system. To isolate it from this perturbation, the support for the mirrors is composed of the actual holder and of a set of isolating rings spaced by rods of damping material. The geometry and the material of the holder have been chosen in order to have the first oscillation eigenmode at around 7kHz while the same parameters of the isolating rings have been selected in such a way that the entire stack will

block the vibrations with frequency higher than $\sim 100\text{Hz}$. A section cut of the CAD drawing of the whole cavity support in the main chamber is shown in Fig. 2.

V. PRELIMINARY TESTS

A first prototype of the cavity holder has been realized in order to test the cavity alignment, the gluing procedure and the quality of the mirrors. This "training" is of primary importance since, once that the final assembly will be placed in the vacuum system, it will not be possible

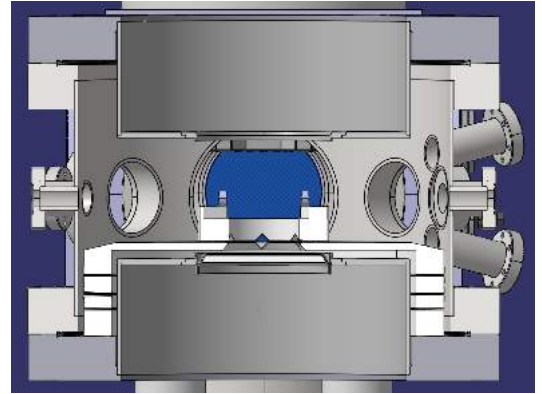


FIG. 2: Section cut of the main chamber with the high finesse cavity. The material selected for the cavity holder is titanium while the isolating rings are made of stainless steel 316L

to act on it. The finesse of the cavity has been measured⁶ for both the wavelength 532nm and 671nm, at different stage of the assembly procedure. We used the measured value as a reference to judge the success or failure of the gluing procedure. Every time that the value of the finesse decreased after the assembly, a different procedure for the gluing has been performed. The measured values for the finesse are (2700 ± 400) at 532 nm and (68000 ± 1300) at 671nm. In conclusion, the results of the first test have shown that the designed setup is suitable for building a high-finesse cavity, which will allow us to implement a non-destructive measurement procedure for the real-time detection of atomic current through a mesoscopic channel.

¹ I. Bloch, J. Dalibard, and W. Zwerger, *Many-body physics with ultracold gases*, Rev. Mod. Phys. **80**, 885 (2008).

² J. Brantut, J. Meinke, D. Stadler, S. Kinner, and T. Esslinger, *Conduction of ultracold fermions through a mesoscopic channel*, Science **337**, 1069 (2012).

³ J. E. Lye, J. J. Hope, and J. D. Close, *Nondestructive dynamic detectors for bose-einstein condensates*, Phys. Rev. A **67**, 043609 (2003).

⁴ B. Zimmermann, Ph.D. thesis, Swiss federal institute of technology, Zürich ETH (2010).

⁵ E. D. Black, *An introduction to pound-drever-hall laser frequency stabilization*, Am. J. Phys. **69**, 79 (2001).

⁶ O. Bettermann, *Realization of a high-finesse fabry-pérot cavity* (2017).

Broadband Raman Heterodyne Spectroscopy of Rare Earth-doped Crystals for Quantum Memory Applications

Antonio Ortu,¹ Alexey Tiranov,¹ Emmanuel Zambrini Cruzeiro,¹ Nicolas Gisin,¹ and Mikael Afzelius¹

¹*Groupe de Physique Appliquée, Université de Genève, CH-1211 Genève 4, Switzerland*

We present a broadband extension of the Raman Heterodyne Spectroscopy (RHS) technique to optically detect spin coherence evolution in rare earth-doped crystals, reporting as a demonstration the case of a spin echo experiment on a $\text{Nd}^{3+}:\text{Y}_2\text{SiO}_5$ crystal in the MHz-GHz range. The technique has wide applicability in spectroscopy and quantum information protocols based on coherence properties of multi-level systems.

I. INTRODUCTION

Rare earth (RE) ions are being extensively studied as doping in solid state crystals for quantum information purposes, such as processing and storage^{1,2}. Some of the main reasons are their long optical and spin coherence times at low temperatures^{3,4} and the wide range of usable optical wavelength, spin transition frequencies and related dipole moments made available by the different RE ions species⁵.

Kramers ions are a type of RE with an odd number of electrons in their $4f$ shell, as opposed to non-Kramers for which the number of electrons is even. This feature leads to a system with a non-zero electronic spin and a strong magnetic moment (up to $15 \mu_B$), which often can be described as a $S = 1/2$ doublet. With the addition of a moderate external magnetic field, the doublet can be split in order to obtain spin transitions in the GHz range, while ground state splittings in non-Kramers ions are usually limited to tens of MHz. Kramers ions can thus allow faster operations in protocols and a wider bandwidth. Moreover, they present optical transitions in the infrared range, where telecommunication optical fibres usually operate and for which diode lasers are easily available. However, their high magnetic moments lead also to stronger interactions with the lattice of the host crystal, which can limit the spin population and coherence lifetimes (T_1 and T_2 respectively). Another consequence is a linewidth of typically one order of magnitude larger for spin transitions in Kramers with respect to non-Kramers (\sim MHz against hundreds of kHz), which translates to a higher power needed for coherent excitation of spin states.

Given the importance of understanding the spin properties of these systems, as in our case for storage in quantum memories, several techniques have so far been implemented⁶. Among them, Raman Heterodyne Spectroscopy (RHS) was used on non-Kramers ions since the '80s⁷. However, RHS on Kramers ions has proven to be more difficult due to their properties and only recently used for detection of up-conversion in Erbium⁸. The main purpose of this work is to extend the application of RHS to the investigation of spin coherence evolution for a large range of doublet energy splittings in Kramers ions. We present as a demonstration the optical detection of the spin echo effect for Nd^{3+} in a Y_2SiO_5 host.

II. RHS AND SPIN ECHO

For our crystal, the RHS technique can be understood by considering a simplified three-level system as in Fig. 1. At a temperature of about 3 K, Nd^{3+} ions are approximately equally distributed among the two sub-levels $|1\rangle$ and $|2\rangle$ of the ground state $^4I_{9/2}$, while the excited state $^4F_{3/2}$, indicated with $|e\rangle$, is mostly empty. A population difference between the ground levels is created by an optical pump, so to strongly populate for instance the $|2\rangle$ level and induce a spin polarization. By coherently probing the transition $|1\rangle \rightarrow |e\rangle$ at the optical frequency ν_0 and at the same time driving the spin transition $|2\rangle \rightarrow |1\rangle$ with a radio-frequency (RF) at ν_{RF} , a coherent Raman emission is induced at a frequency $\nu_R = \nu_S - \nu_{RF}$ due to transitions $|e\rangle \rightarrow |2\rangle$. The coherent Raman emission is then usually detected by interference with the transmitted component of the probe beam as a beat at the frequency $\nu_0 - \nu_R$. However, this can be a problem for the limited bandwidth of optical detectors, especially when the splitting between the spin states is varied in a large range of energies. To overcome this limitation, we combine the beam to be detected with another one from the same laser source as the probe, but with a chosen shift in frequency (the *local oscillator*). This way, the Raman radiation is instead detected as a beat at the frequency $|\nu_{LO} - \nu_R|$, which in principle can be fixed so to be inside the bandwidth of the photodetector used, no matter what the spin transition frequency is.

In a similar way, a spin echo is able to produce a corresponding coherent Raman emission, making it possible to use RHS for its detection. A spin echo is induced by a combination of pulses as in Fig. 1, with durations carefully chosen according to previous observation of Rabi oscillations. After a long and strong pump pulse used to create the population difference in the ground sub-levels, a $\pi/2$ RF pulse induces a coherent superposition of the ground spin states. A dephasing process, due to inhomogeneous broadening of the spin transition, will then take place. This dephasing can be reversed by means of a π RF pulse. Following the rephasing, the ions will collectively return to the initial state producing a strong emission, or echo, after a time from the π pulse equal to the delay Δ between the $\pi/2$ and π pulses. If at the same time a weak optical probe pulse resonant with the $|1\rangle \rightarrow |e\rangle$

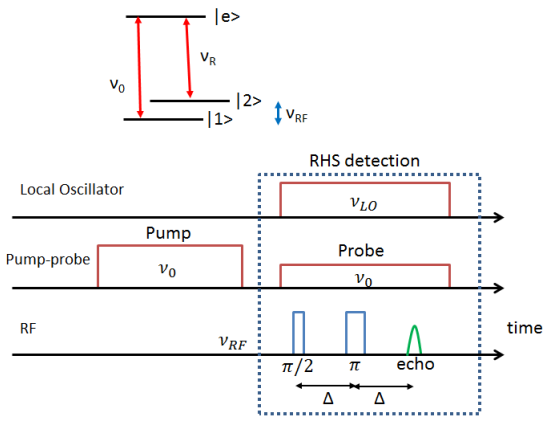


FIG. 1: Top: simplified scheme of the three level system made of a ground Kramers doublet and an excited state. Bottom: optical and RF pulse sequences for spin echo observation.

transition is applied on the system, a corresponding Raman emission at the frequency ν_R will be generated. By analysing the amplitude of the echo as a function of the delay between the input RF pulses, one can deduce coherence properties of the sub-levels related to the spin transition, as for instance the coherence lifetime T_2 .

III. EXPERIMENT

For the detection of the spin echo, a pulse sequence of the type represented in Fig. 1 is used. By constantly applying a weak probe pulse during the full RF pulse sequence, it is possible to detect the Fourier transform of the transmitted light combined with the local oscillator and the effect the RF pulses induce on the ions population, as shown in Fig. 2. The Fourier transform is filtered around the beat frequency $|\nu_{LO} - \nu_R|$ and then anti-transformed so to generate a time domain representation of the Raman emission. The first RF pulse is followed by a strong free induction decay (FID) signal, due to the broad excitation induced by the short $\pi/2$ pulse. After a time equal to the delay Δ between the RF pulses, an echo becomes clearly visible. The measurement was

repeated for delays Δ ranging from 0.8 to 2.6 μs and the area of the echo pulse computed from the data. Fig. 2 shows the results with an exponential fit, which yields a coherence time T_2 of $1.55 \pm 0.15 \mu\text{s}$, given an expected time dependence of the intensity of the echo pulse proportional to $\sim \exp(-4\Delta/T_2)$.

Our results show how it is possible to apply the RHS technique for the optical detection of the spin coherence evolution in Kramers ions. The large bandwidth, high sensitivity and the simplicity of the necessary setup make it a flexible instrument of investigation of coherence-related effects in various systems, interesting for quantum communication and processing applications, such as RE ions, vacancy centres and quantum dots.

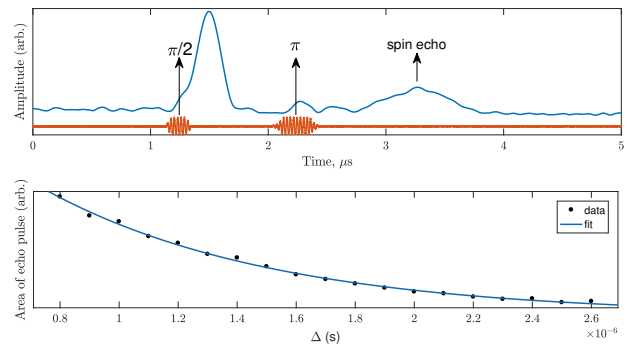


FIG. 2: Top: example of spin echo detection: the time sequence shows in orange the two excitation RF pulses at $\nu_{RF} = 35 \text{ MHz}$, delayed by $\Delta = 1 \mu\text{s}$, and the blue line shows the consequent FID and echo pulse, obtained by deconvolution of the filtered Fourier transform of the light transmitted by the crystal. Bottom: area of the spin echo pulse as a function of the time delay between the $\pi/2$ and π RF pulses. The solid line is an exponential fit, yielding a T_2 of $1.55 \pm 0.15 \mu\text{s}$ (statistical error).

Acknowledgments

This work is funded by the Swiss NCCR-QSIT and the European Marie Skłodowska-Curie QCALL programs.

- ¹ F. Bussi eres, N. Sangouard, M. Afzelius, H. de Riedmatten, C. Simon, and W. Tittel, *Journal of Modern Optics* **60**, 1519 (2013).
- ² M. Afzelius and H. de Riedmatten, in *Engineering the Atom-Photon Interaction: Controlling Fundamental Processes with Photons, Atoms and Solids*, edited by A. Predojevi c and M. W. Mithcell (Springer International Publishing, 2015), pp. 241–268.
- ³ Y. Sun, C. W. Thiel, R. L. Cone, R. W. Equall, and R. L. Hutcheson, *J. Lumin.* **98**, 281 (2002).
- ⁴ M. Zhong, M. P. Hedges, R. L. Ahlefeldt, J. G. Bartholomew, S. E. Beavan, S. M. Wittig, and J. J.

Longdell, *Nature* **517**, 177 (2015).

- ⁵ W. Tittel, M. Afzelius, T. Cheneli ere, R. Cone, S. Kr oll, S. Moiseev, and M. Sellars, *Laser and Photonics Reviews* **4**, 244 (2010).
- ⁶ P. Goldner, A. Ferrier, and O. Guillot-N oel, in *Handbook on Physics and Chemistry of Rare Earths*, edited by J. B unzli and V. Pecharsky (North-Holland, 2015), vol. 46, chap. 267.
- ⁷ J. Mlynek, N. C. Wong, R. G. DeVoe, E. S. Kintzer, and R. G. Brewer, *Phys. Rev. Lett.* **50**, 995 (1983).
- ⁸ X. Fernandez-Gonzalvo, Y.-H. Chen, C. Yin, S. Rogge, and J. Longdell, *Phys. Rev. A* **92**, 062313 (2015).

Two methods analysis of the driven, dissipative Dicke mode

Matteo Soriente, Rama Chitra, and Oded Zilberberg

Institute for Theoretical Physics, ETH-Hönggerberg, CH-8093, Zürich, Switzerland

We study the Dicke model, that is, a driven photonic cavity coupled to numerous two-level systems using two different methods. First, we study the Lindblad master-equation describing the evolution of the density matrix using standard quantum optics technique. Second, we apply a Keldysh-path integral approach to go beyond the mean-field solutions.

I. INTRODUCTION

As for the first three months of the PhD project we have been reviewing some known results regarding the Dicke model. This is so because, in recent years, there has been incredible experimental progress in control and manipulation of light-matter quantum systems. A defining feature of many of these systems is that they are inherently driven and subject to dissipation, for instance due to the presence of cavities. This has generated a growing interest in the study of many-body phenomena out-of-equilibrium and the possibility to have out-of-equilibrium phase transition. We focus our attention to a particular realization of such a system, described by the so-called Dicke model¹. Here, a single bosonic cavity mode is coupled to a large number of two-level systems, or "qubits". It exhibits a Z_2 symmetry breaking quantum phase transition from a normal phase (NP), where all the atoms are in their ground state and the cavity is empty, to a super-radiant phase (SP), where the atoms are excited and the cavity is in a coherent state, i.e. a photon condensate appears. The Hamiltonian describing the coherent evolution of the system is

$$H = \hbar\omega_c a^\dagger a + \hbar\omega_a \sum_{i=1}^N s_z^i + \frac{2\hbar\lambda}{\sqrt{N}} \sum_{i=1}^N s_x^i (a + a^\dagger), \quad (1)$$

where s_α^i with $\alpha = x, y, z$ are the spin operators describing the i -th two-level system, and a^\dagger, a represent the cavity creation and annihilation operators, respectively. The cavity's resonance frequency is ω_c , whereas the atoms are considered to be identical with level spacing $\hbar\omega_a$. The driven and dissipative nature of the system is described by a Liouvillian equation for the density matrix ρ of the system

$$\frac{d\rho}{dt} = -\frac{i}{\hbar} [H, \rho] + \kappa [2a\rho a^\dagger - \{a^\dagger a, \rho\}] + \frac{\eta}{N} \sum_{i,j=1}^N [2s_-^i \rho s_+^j - \{s_+^i s_-^j, \rho\}], \quad (2)$$

where $s_\pm^j = s_x^j \pm i s_y^j$ are ladder operators. The first term on the right-hand side describes the standard Hamiltonian evolution and the last two terms represent the Markovian dissipation for both cavity and a global dissipation for the qubits in Lindblad form with rates κ and η , respectively. We study this system with two different approaches, namely, a mean-field approach to analyze the Heisenberg-Langevin equations and a Keldysh-path integral one that allows us to go beyond the mean field results, e.g., taking into account finite size corrections.

II. MEAN-FIELD EQUATIONS

The mean-field ansatz that we use states that the total density matrix in the steady state is a product state of the individual density matrices, $\rho = \rho_c \otimes \prod_{i=1}^N \rho_i$, where ρ_c and ρ_i are density matrices of the cavity and the i -th atom, respectively. We assume all ρ_i to be equivalent and define the order parameters $\alpha = \langle a \rangle / \sqrt{N}$, $\beta = \langle \sum_i s_\beta^i \rangle / N$ with $\beta = x, y, z$. We then look at the steady-state solution in the thermodynamic limit ($N \rightarrow \infty$). We find the well known Dicke transition but modified by the presence of the dissipative terms, Fig. 1. In particular, the transition happens when the coupling strength exceeds the critical value

$$\lambda_c^{mf} = \frac{1}{2} \sqrt{\frac{(\eta^2 + \omega_a^2)(\kappa^2 + \omega_c^2)}{\omega_a \omega_c}}, \quad (3)$$

where the presence of atomic dissipation, $\eta \neq 0$, shifts the threshold. The role of out-of-equilibrium dynamics can be understood by the appearance of a non vanishing order parameter along the y spin polarization. This phenomenon is only present because of the atomic dissipation, it is in fact absent for $\eta = 0$, dashed lines Fig. 1. We can also see how in the dissipative case the total spin is no more conserved.

III. KELDYSH APPROACH

We start from the Liouvillian master equation (2) with constant drive, λ , and map it into a dissipative Keldysh action $S[a^*, a, b^*, b]$ for both the photon (a) and spin (b) field variables². To study the photon observable we simply integrate out the spin degrees of freedom and vice-versa for the spin ones. Once we find the advanced, retarded and Keldysh Green's functions we are immediately given the response and correlation functions of the system. The former is encoded in the retarded and advanced Green's functions while the latter in the Keldysh one. This allows us to find the low-frequency effective temperature at which the cavity and the spins equilibrate, $T_c^{eff} = \frac{\omega_c^2 + \kappa^2}{4\omega_c}$ and $T_a^{eff} = \frac{\omega_a^2 + \eta^2}{4\omega_a}$, respectively³. Finally, this formalism is most suitable to study finite N correction. For instance we can look at the photon number in the cavity near the transition which is expected to diverge in the thermodynamic limit, Fig. 2.

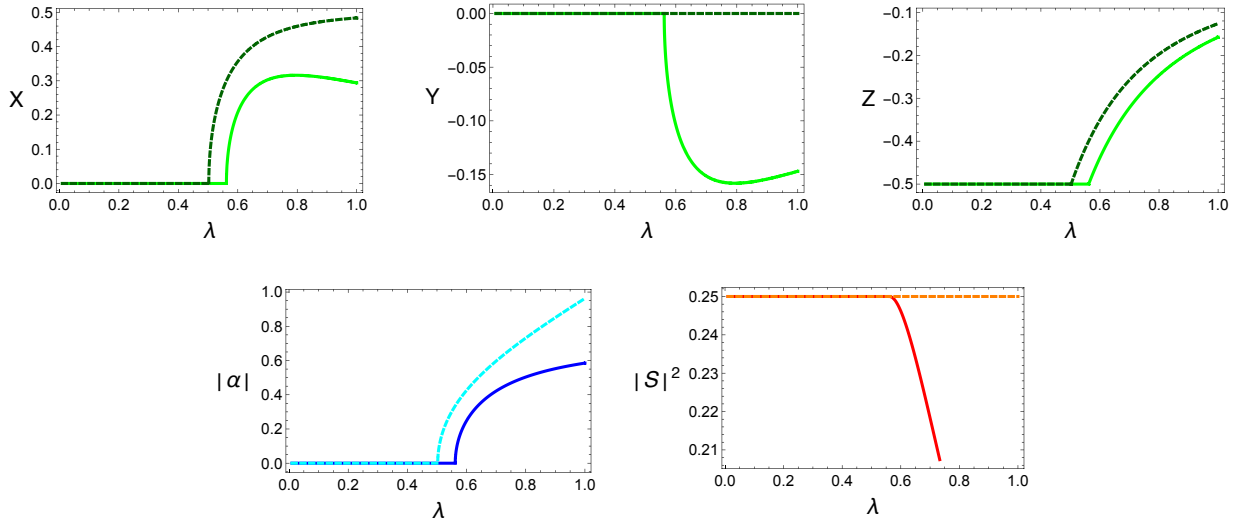


FIG. 1: Characteristics of the phase transition of the driven Dicke model as a function of the coupling strength λ in with (solid line) and without (dashed line) atomic dissipation η . The most relevant features are a shift of the transition towards larger λ values, a non-zero Y spin polarization and $|S|^2 = |X|^2 + |Y|^2 + |Z|^2$ not more conserved above threshold. Numerical parameters: $\omega_a = 2.0, \omega_c = 1.0, \kappa = 1.0, \eta = 0.5$.

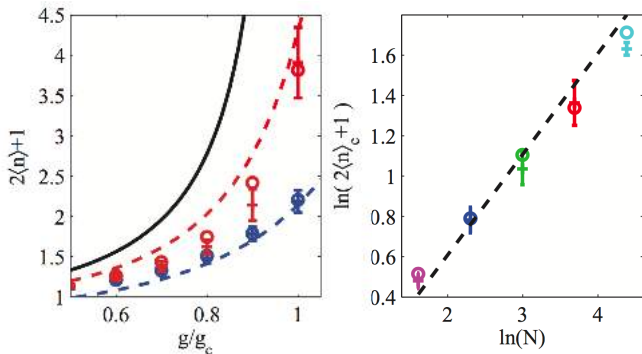


FIG. 2: (Left) Photon occupation in the vicinity of the Dicke transition for $N = 10$ (blue), 40 (red). (Right) Photon occupation at the critical point as function of the system size. The circles (\circ), crosses ($+$) and dashed lines correspond to the one-loop Keldysh resummation, to the effective equilibrium theory, to the Monte Carlo solution of the original master equation. The solid curve corresponds to the mean-field solution, valid in thermodynamic limit. Numerical parameters: $\omega_a = 2.0, \omega_c = 1.0, \kappa = 1.0, \lambda_c^K = 1.0$.

IV. CONCLUSION AND OUTLOOKS

We studied the driven dissipative Dicke model with two different methods. First, we described the system using a mean-field approach. We found that the onset of

the transition is modified by the presence of atom dissipation described in a Lindblad form with the dissipation rate η . We then used a Keldysh approach in order to go beyond the mean-field level. Remarkably, we showed that due to its out-of-equilibrium nature the system in the low-frequency limit is not in a global thermal state even though the cavity and the spins separately are, with two different effective temperatures. The natural development of this study would be to introduce the Keldysh formalism to study more involved problems like the parametrically driven Dicke model already addressed at the mean-field level⁴ or possibly to introduce an additional cavity-spin coupling, e.g. with the s_y component. It might also be possible to apply Keldysh formalism to the recently experimentally realized supersolid in a quantum gas⁵ where one could study the role of dissipation and disorder. Finally, it would be interesting to translate the Keldysh formalism to the description of other light-matter models, where dissipation, and out-of-equilibrium play an important role.

Acknowledgments

We acknowledge financial support from the Swiss National Science Foundation (SNF).

¹ F. Brennecke, R. Mottl, K. Baumann, R. Landig, T. Donner, and T. Esslinger, Proc. Natl. Acad. Sci. **110**, 11763 (2013).

² L. M. Sieberer, M. Buchhold, and S. Diehl, Rep. Prog. Phys. **79**, 096001 (2016).

³ E. G. D. Torre, S. Diehl, M. D. Lukin, S. Sachdev, and

P. Strack, Phys. Rev. A **87**, 023831 (2013).

⁴ R. Chitra and O. Zilberberg, Phys. Rev. A **92**, 023815 (2015).

⁵ J. Léonard, A. Morales, P. Zupancic, T. Esslinger, and T. Donner, Nature **543**, 87 (2017).

Levitated Nanoparticles in a Microcavity

Dominik Windey,¹ Rene Reimann,¹ Sebastian Starosielec,² Ben Petrak,² Richard Warburton,² and Lukas Novotny¹

¹*Professur für Photonik, ETH Hönggerberg, CH-8093 Zürich, Switzerland*

²*Nano-Photonics Group, University of Basel, CH-4056 Basel, Switzerland*

We study the coupling of optically levitated nanoparticles in vacuum to the light field inside an optical cavity. Our aim is to cool the particle's center-of-mass (CM) motion to the quantum mechanical ground state by employing optical feedback cooling and cavity-enhanced anti-Stokes scattering. We will use light that leaks out of the cavity to detect the particle's motion. To minimize the cavity's mode volume and thereby enhance particle-light interaction we fabricate micro-cavity mirrors, using a hot embossing technique.

I. INTRODUCTION

Optomechanics studies the coupling between light and mechanical objects. Well controlled optomechanical systems are promising candidates to observe the quantum to classical transition¹ or could be used as ultra-sensitive force sensors due to their high mechanical quality factors Q . The cooling of mechanical systems by optical methods has been demonstrated with various systems such as cantilevers, toroidal cavities, nanobeams or membranes. An advantage of levitated nanoparticles over many of the above mentioned systems is the nearly perfect decoupling of the particles from their environment due to the absence of clamping losses. This leads to possible CM motional Q -factors in excess of 10^8 under UHV conditions (10^{-8} mbar). As the CM motion is additionally decoupled from the internal vibrations of the particle² one profits from not requiring a cryogenic environment. In relation to fragile cold atom based optomechanical systems, observing a levitated nanoparticle induces much less motional decoherence: Recoil heating events and photon scattering differ by about nine orders of magnitude³ due to the comparably large nanoparticle mass.

In contrast to other mechanical oscillators⁴ levitated nanoparticles have not been cooled to their ground state, yet. So far levitated particles have been controlled and

cooled via active feedback cooling³ and via passive cavity cooling⁵. Up to now neither of the two approaches has led to CM motional ground-state cooling of the particles.

II. FEEDBACK COOLING

Within our group an efficient parametric feedback cooling scheme³ has been developed that stabilizes the particle's motion in 3D. In this experiment the polarizable particle is trapped close to the intensity maximum of a strongly focused laser beam by dipole forces, as shown in figure 1. The principle of feedback cooling is based on the linear dependence of the trap stiffness $k \propto \Omega_{\text{mech}}^2$ on I . To cool, the intensity and therefore k is increased as the sphere moves away from the trap center and is lowered as the sphere returns to the trap center.

III. MICROCAVITY

Placing the trapped nanosphere inside a cavity as shown schematically in figure 2 strongly enhances the detection sensitivity to a level where, in principle, the motional ground state of the sphere can be resolved⁶. Simultaneously, one would benefit from combining a cavity with the described free space feedback cooling setup to stabilize the sphere position and for precooling.

It has been theoretically shown that a mechanical oscillator coupled to a cavity can be ground-state cooled either in the resolved-sideband regime ($k < \Omega_{\text{mech}}$) by passive cavity cooling or in the fast cavity regime ($\kappa > \Omega_{\text{mech}}$) by active feedback cooling where the cavity acts as a position measurement amplifier. At first sight, the resolved-sideband approach seems superior to the fast cavity approach; with the correct detuning between driving laser frequency and cavity resonance $\Delta = \omega - \omega_c \approx -\Omega_{\text{mech}}$, sideband cooling should in principle cool the sphere to its CM motional ground state for low enough background pressures - no further experimental action is needed. However, there are several disadvantages to this approach. Among them is the fact that in the resolved-sideband regime the cavity acts as a low-pass filter with cutoff frequency below the sphere's mechani-

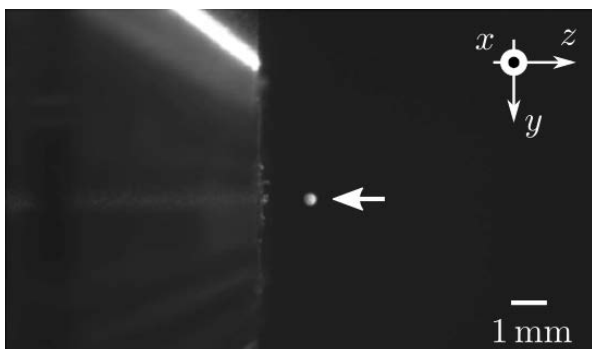


FIG. 1: Photograph of light scattered from an optically trapped fused silica nanosphere (arrow) with radius $R \approx 70$ nm. The object to the left is a part of the objective that strongly focuses the trapping beam on the levitated sphere.

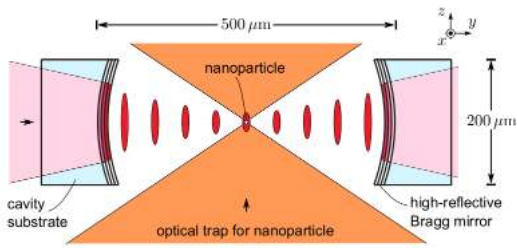


FIG. 2: Top view of the planned microcavity apparatus (simplified cross section sketch). The nanosphere will be trapped close to the focus of the objective.

cal frequency, making it difficult to verify whether the sphere has reached the CM motional ground state. Disadvantages are technically challenging requirements for the laser source and the cavity finesse \mathcal{F} .

Even though the CM motional ground state cannot be reached by standard, passive cavity cooling in the fast cavity regime, it has become clear that the fast cavity regime - entered with a short high-finesse cavity - shows several advantages over the resolved-sideband regime: The passive cavity cooling rate can still be significant and the limit regarding the phase noise of the driving laser is less stringent. Most importantly, measuring the sphere's motional state, the information retrieval rate and measurement sensitivity are increased.

To maximize sensitivity of the nanoparticle motion the cavity's mode volume must be decreased to a minimum set by the optical accessibility of the nanoparticle. We therefore will use a microcavity to measure and cool the particle motion. The project benefits from the knowledge of microcavity fabrication of the Warburton group which is able to fabricate micro mirrors using a CO₂ laser ablation technique⁷. The fabrication technique results in sufficiently smooth but gaussian-shaped mirror profiles which exhibit mode-mixing losses at long enough mirror separation⁸. As shown in figure 3 the finesse drops at cavity lengths of about 250 μm making it unsuitable to operate the cavity at a cavity length of 500 μm. Cur-

rently the aim is to develop a hot embossing technique that pre-shapes the mirror substrates to a more spherical shape and use CO₂ laser ablation as a finishing step to smoothen the surface.

We presented the key technologies which we think will be necessary to bring a levitated nanoparticle into the CM motional ground-state. We recently built up the vacuum chamber that will house the experiment. Furthermore we were able to measure the finesse \mathcal{F} of an optical microcavity as shown in figure 3. The observed drop in finesse led to the conclusion to fabricate cavity mirrors by employing a hot embossing technique and not only laser ablation which is typically done.

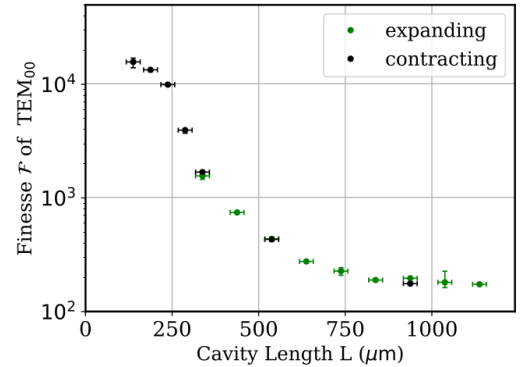


FIG. 3: The finesse of a cavity formed from a micromirror and a flat mirror is measured as a function of the cavity length. Far before leaving the stable cavity region the cavity finesse decreases. This result can be understood by transverse mode coupling and diffraction loss arising from the Gaussian mirror profile⁸.

Acknowledgments

This research was supported by ERC-QMES (Grant No. 338763), by ETH Zurich, and by QSIT through the Directors Reserve Project 'A Novel Mesoscopic Cavity Device'.

¹ M. Schlosshauer, *The quantum-to-classical transition and decoherence* (2014), arXiv:1404.2635.
² D. E. Chang, C. A. Regal, S. B. Papp, D. J. Wilson, J. Ye, O. Painter, H. J. Kimble, and P. Zoller, *Cavity optomechanics using an optically levitated nanosphere*, Proc. Natl. Acad. Sci. U. S. A. **107**, 1005 (2010).
³ J. Gieseler, B. Deutsch, R. Quidant, and L. Novotny, *Subkelvin parametric feedback cooling of a laser-trapped nanoparticle*, Phys. Rev. Lett. **109**, 103603 (2012).
⁴ J. Chan, T. P. M. Alegre, A. H. Safavi-Naeini, J. T. Hill, A. Krause, S. Groeblacher, M. Aspelmeyer, and O. Painter, *Laser cooling of a nanomechanical oscillator into its quantum ground state*, Nature **478**, 89 (2011).
⁵ P. Asenbaum, S. Kuhn, S. Nimmrichter, U. Sezer, and M. Arndt, *Cavity cooling of free silicon nanoparticles in*

high vacuum, Nat. Commun. **4**, 2743 (2013).

⁶ C. Genes, D. Vitali, P. Tombesi, S. Gigan, and M. Aspelmeyer, *Ground-state cooling of a micromechanical oscillator: Comparing cold damping and cavity-assisted cooling schemes*, Phys. Rev. A **77**, 033804 (2008).

⁷ L. Greuter, S. Starosielec, D. Najer, A. Ludwig, L. Duempelmann, D. Rohner, and R. J. Warburton, *A small mode volume tunable microcavity: Development and characterization*, Applied Physics Letters **105**, 121105 (2014).

⁸ J. Benedikter, T. Hümmer, M. Mader, B. Schlederer, J. Reichel, T. W. Hänsch, and D. Hunger, *Transverse-mode coupling and diffraction loss in tunable Fabry-Pérot microcavities*, New Journal of Physics **17**, 053051 (2015).

Nanoscale imaging of magnetic structures with a diamond magnetometer

M. S. Wörnle,^{1,2} K. Chang,² M. Palm,² P. Welter,² C. Degen,² and P. Gambardella¹

¹Departement of Materials, ETH- Zürich, CH-8093, Zürich, Switzerland

²Institute of Solid State Physics, ETH- Zürich, CH-8093, Zürich, Switzerland

Diamond magnetometer offers a possibility to measure small magnetic fields at ambient temperature with high sensitivity and spatial resolution. Due to its noninvasive nature, it is an ideal measurement tool to investigate magnetic structures at nanometer scales, usually sensitiv to external magnetic perturbations. Here we shortly describe the diamond magnetometer setup and motivate its future use for investigating magnetic structures.

I. INTRODUCTION

Ultrathin ferromagnets, such as Pt/Co/AlO_x trilayers, have attracted considerable interest for the development of low power spintronic devices¹. However imaging the magnetic structure of those systems at nanometer scales remains challenging: Magnetic Force Microscopy is not suitable because of the high sensitivity of certain magnetic structures, like domain walls, to the magnetic tip and techniques based on X-rays suffer from low sensitivity due to a small interacting volume¹.

A promising alternative is the so-called diamond magnetometer. It employs a single spin defect hosted in a diamond crystal which is attached to the tip of an atomic force cantilever to sense local magnetic fields near a sample². The diamond magnetometer allows measuring local magnetic fields at ambient temperatures with high spatial resolution and sensitivity. There is no significant back-action on the sample, in contrast to for example magnetic force microscopy which makes it an ideal measurement technique to investigate the magnetic structure of ultrathin ferromagnets¹. For instance there is a debate about the stabilisation of Néel walls by the Dzyaloshinski-Moriya interaction in ultrathin magnetic films which might be solved by mapping the domain structure^{1,3}. Additionally, imaging current-controlled domain wall motion at nanoscales would help for the development of non-volatile magnetic storage devices, like magnetic random access memories (MRAM)⁴. The construction of a diamond magnetometer is part of our work to try to solve those questions. Here we describe the basic working principle of a diamond magnetometer.

II. EXPERIMENTAL SYSTEM

The diamond crystal hosts a nitrogen-vacancy (NV) center which is a single spin system with a triplet ground $|g\rangle$ and excited state $|e\rangle$ as well as a metastable singlet state $|s\rangle$ (FIG 1). Transitions between $|g\rangle$ and $|e\rangle$ are spin conserving⁵. The transition probability for a decay to the long-lived singlet state $|s\rangle$ is however spin dependent and much higher for the spin sublevels $m_s = \pm 1$. This additional spin dependent decay mechanism leads to an optical contrast between the $m_s = \pm 1$ and $m_s = 0$ spin sublevels. Sweeping a microwave field over the elec-

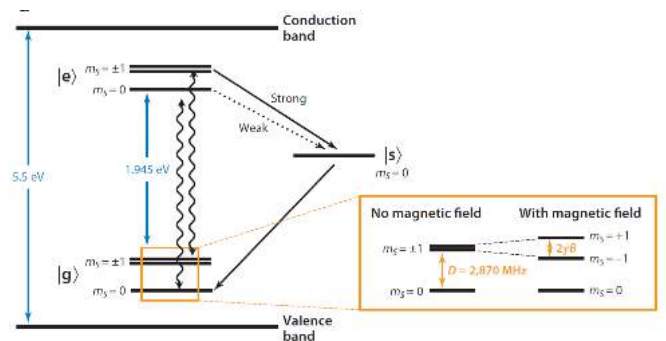


FIG. 1: Energy level diagram for NV-center. $|g\rangle$, $|e\rangle$ and $|s\rangle$ denotes the electronic ground state, excited state and metastable singlet state, respectively. Wiggly arrows indicate radiative transition, black arrows indicate non-radiative decay. The inset shows the Zeeman splitting when applying a magnetic field. Besides the optical transition between $|e\rangle$ and $|g\rangle$ a decay by intersystem crossing to the long-lived $|s\rangle$ is possible^{5,6}.

tron paramagnetic resonance (EPR) causes a reduction of the luminescence intensity due excitation between the $m_s = \pm 1$ and $m_s = 0$ levels. This so-called optically detected magnetic resonance (ODMR) provides a means to detect magnetic fields from the sample and magnetic stray fields from magnetic samples. As a consequence of the Zeeman splitting the resonance frequency is shifted by $2\gamma B$ where γ is the electron gyromagnetic ration and B is the magnetic field (FIG. 1). The recorded spectrum is called EPR spectrum and is shown in FIG. 2 for an applied magnetic field of 4.4 mT⁵⁻⁷. A confocal microscope is used for EPR measurements. The excitation laser (532 nm) is reflected by a dichroic mirror and focused onto the NV-center. The fluorescent photons are collected via the same way but pass the dichroic mirror and are detected by a photodiode⁵.

The diamond crystal, hosting the NV-center, is attached to a tip of an atomic force cantilever (FIG. 3) and positioned over the sample using atomic force microscopy protocols. By scanning the diamond crystal over the sample, high-resolution magnetic images are recorded with a spatial resolution limited by the distance of the sample

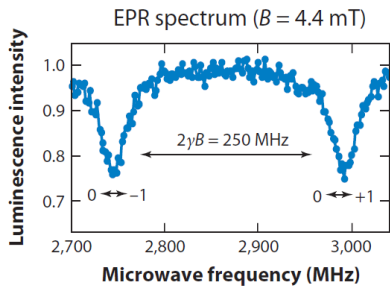


FIG. 2: Electron paramagnetic resonance spectrum of a single NV-center at nonzero magnetic field (4.4 mT), recorded using the optically detected magnetic resonance technique⁶.

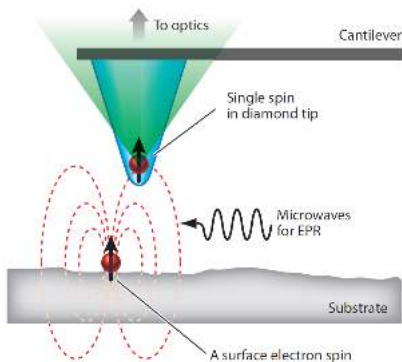


FIG. 3: Basic principle of a diamond magnetometer. A diamond tip, hosting a NV-center, is attached to a cantilever. The NV-center is excited at 532 nm. The luminescent photons are guided to an avalanche photodiode. Here the NV-center measures the magnetic field of a surface electron spins⁶.

surface to the single spin defect⁶. Spatial resolution down to 30 nm with a magnetic field sensitivity of about $1 \mu\text{T}$ have been demonstrated at ambient temperatures⁸.

III. CONCLUSION

Here we have described the basic mechanism of diamond magnetometry to investigate the magnetic structure of ultrathin ferromagnets at nanometer scales. Stray fields of magnetic vortices and bubble domains have already been measured using a diamond magnetometer showing its potential to investigate ultrathin ferromagnetic films^{1,9?} ¹⁰. One goal is to image current-controlled domain wall motion which helps for the development of non-volatile memory storage devices.

- ¹ J.-P. Tetienne, T. Hingant, L. Rondin, S. Rohart, A. Thiaville, E. Jué, G. Gaudin, J.-F. Roch, and V. Jacques, *Nitrogen-vacancy-center imaging of bubble domains in a 6-Å film of cobalt with perpendicular magnetization*, Journal of Applied Physics **115**, 17D501 (2014).
- ² C. Degen, *Scanning magnetic field microscope with a diamond single-spin sensor*, Applied Physics Letters **92**, 243111 (2008).
- ³ A. Thiaville, S. Rohart, É. Jué, V. Cros, and A. Fert, *Dynamics of dzyaloshinskii domain walls in ultrathin magnetic films*, EPL (Europhysics Letters) **100**, 57002 (2012).
- ⁴ C. Chappert, A. Fert, and F. N. Van Dau, *The emergence of spin electronics in data storage*, Nature materials **6**, 813 (2007).
- ⁵ K. Chang, *Scanning magnetometry with nv centers in diamond*, PhD. Thesis ETH Zürich (2016).
- ⁶ R. Schirhagl, K. Chang, M. Loretz, and C. L. Degen, *Nitrogen-vacancy centers in diamond: nanoscale sensors for physics and biology*, Annual review of physical chemistry **65**, 83 (2014).
- ⁷ L. Rondin, J. Tetienne, T. Hingant, J. Roch, P. Maletinsky,

- and V. Jacques, *Magnetometry with nitrogen-vacancy defects in diamond*, Reports on progress in physics **77**, 056503 (2014).
- ⁸ K. Chang, A. Eichler, and C. Degen, *Nanoscale imaging of current density with a single-spin magnetometer*, arXiv preprint arXiv:1609.09644 (2016).
- ⁹ L. Rondin, J.-P. Tetienne, P. Spinicelli, C. Dal Savio, K. Karrai, G. Dantelle, A. Thiaville, S. Rohart, J.-F. Roch, and V. Jacques, *Nanoscale magnetic field mapping with a single spin scanning probe magnetometer*, Applied Physics Letters **100**, 153118 (2012).
- ¹⁰ L. Rondin, J.-P. Tetienne, S. Rohart, A. Thiaville, T. Hingant, P. Spinicelli, J.-F. Roch, and V. Jacques, *Stray-field imaging of magnetic vortices with a single diamond spin*, Nature communications **4** (2013).
- ¹¹ J.-P. Tetienne, T. Hingant, J.-V. Kim, L. H. Diez, J.-P. Adam, K. Garcia, J.-F. Roch, S. Rohart, A. Thiaville, D. Ravelosona, et al., *Nanoscale imaging and control of domain-wall hopping with a nitrogen-vacancy center microscope*, Science **344**, 1366 (2014).

Scattering of Dirac Fermions on hexagonal periodic structures in 2D

Tobias Wolf,¹ Ivan Levkivskiy,¹ Gianni Blatter,¹ and Oded Zilberberg¹

¹*Institute for Theoretical Physics, ETH Zurich, 8093 Zurich, Switzerland*

We study non-interacting spin-less Dirac Fermions in two dimensions subjected to a smooth periodic potential with three-fold rotational symmetry. This model can be realized in the low-energy physics of various condensed matter systems, a prominent example being graphene aligned with a hexagonal Boron Nitride substrate. We complement known results for the band structure with analytical studies and thus provide deeper insight into the plethora of possible realizations of the model.

I. INTRODUCTION

In recent years, low-energy analogues of Dirac fermions have been identified in a wide range of systems within the condensed matter setting, including graphene-like 2D materials^{1–3}, topological insulators⁴, topological crystalline insulators⁵, as well as *d*-wave cuprate superconductors⁶ and Weyl semimetals. In the solid-state realm, technological advances in fabrication techniques of the recent years have allowed the synthesis of novel materials and structures. A particularly prominent example are Van-der-Waals (VdW) heterostructures^{7,8} which are built by manually stacking exfoliated 2D crystals. It is in this context that the question of how Dirac materials are influenced by perturbing periodic structures originates and has been studied^{9–12}. However, the physical description transcends this solid-state realization and can also be implemented in other systems.

In this work, we analytically determine the band structure of a Dirac material that is perturbed by a generic three-fold symmetric potential using perturbation theory. Our analytical results are in good agreement with numerical diagonalization, and allow for a direct study of the dependence on model parameters of the general potential. We further discuss potential realizations, including VdW heterostructures, nano-patterned heterostructures, photonic crystals and cold atoms in optical lattices.

II. MODEL

We consider a spinless Dirac particle moving in two dimensions in the presence of a weak periodic potential. Such a system can be described by the Hamiltonian

$$H = [v \mathbf{p} - \nabla_{\perp} a(\mathbf{x})] \cdot \boldsymbol{\sigma} + [\Delta + m(\mathbf{x})] \sigma_z + u(\mathbf{x}), \quad (1)$$

where $T(\mathbf{k}) = v \hbar \mathbf{k} \cdot \boldsymbol{\sigma} + \Delta \sigma_3$ describes a free Dirac particle with mass Δ moving at Fermi velocity v with momentum $\mathbf{k} = (k_1, k_2)$. We have used Pauli matrices σ_j and $\nabla_{\perp} = \mathbf{z} \times \nabla$ to express H .

The terms with spatial dependence in Eq. (1) capture the presence of a general periodic potential. We assume the potential to be smooth and have a three-fold rotational symmetry, such that it only contains long-wavelength components with an underlying hexagonal

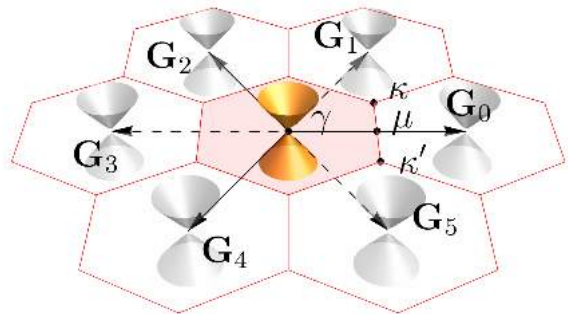


FIG. 1: Reciprocal space illustration of scattering of Dirac particles from a smooth, and periodic three-fold rotational symmetric potential. The potential imposes periodic mirroring (light gray) of the Dirac spectrum (darker orange), leading to hybridization of bands at the boundary of the first Brillouin zone (shaded red). The solid and dashed arrows highlight the three-fold nature of the scattering. The special high-symmetry points γ , μ , κ and κ' are marked and play an important role when investigating degeneracies in the band structure.

lattice periodicity. The real scalar potentials then take the form

$$\chi(\mathbf{x}) = \sum_{\ell=0,\dots,5} (\chi + i(-1)^\ell \chi') e^{i \mathbf{G}_\ell \cdot \mathbf{x}} \quad (2)$$

for $\chi = a, m, u$, where the reciprocal lattice vectors $\mathbf{G}_\ell = G \cdot (\cos(\frac{2\pi}{6}\ell), \sin(\frac{2\pi}{6}\ell))$ with $\ell = 0, \dots, 5$ describe the long-wavelength periodicity $L = 4\pi/(3G)$. The reciprocal lattice constant G defines the recoil energy $\epsilon_0 \equiv v \hbar G/2$ for elastic scattering. We assume that the latter is much larger than the Dirac mass Δ and than the amplitudes of the potential.

The periodic potential can be treated using Bloch's theorem. As a result, the free Dirac spectrum is folded in reciprocal space, leading to hybridization of bands, see Fig. 1. Formally, this band structure is obtained by diagonalizing the Bloch Hamiltonian on the first Brillouin zone.

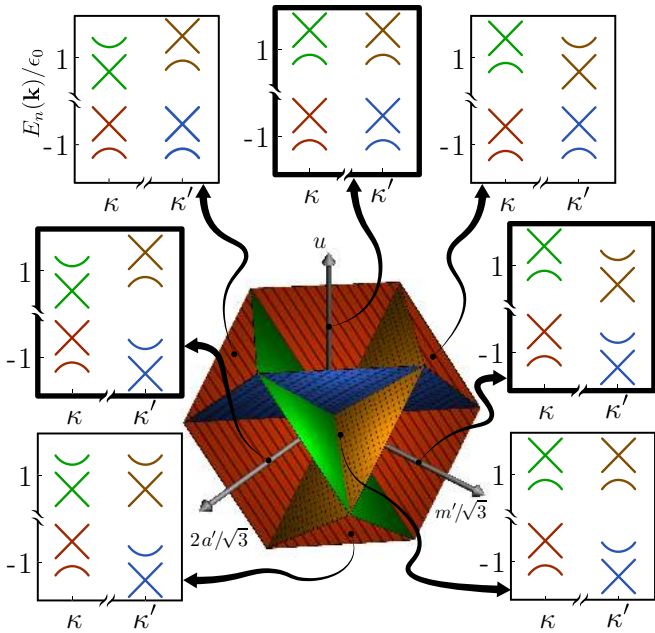


FIG. 2: Parameter space for inversion-symmetric terms u, m', a' of the three-fold rotationally symmetric potential while inversion-asymmetric terms u', m, a are set to vanish. The partitioning planes mark the presence of three-fold degeneracies at κ (κ') at positive or negative energies. The surrounding insets schematically show how the three-fold degenerate band crossings can be split into different band configurations by the potential. The persistent crossings can be split by including inversion-asymmetric terms.

III. RESULTS

The lowest three energy bands ($j = 0, 1, 2$) at positive and negative ($s = \pm$) energies in vicinity of momentum κ take the form

$$\epsilon_{\kappa s}^{(j)}(\mathbf{q}) = \bar{\epsilon}_{\kappa s}(\mathbf{q}) + 2\delta\epsilon_{\kappa s}(\mathbf{q}) \cos\left(\frac{\phi_s(\mathbf{q}) + 2\pi j}{3}\right) \quad (3)$$

where $\bar{\epsilon}_{\kappa s}(\mathbf{q})$, $\delta\epsilon_{\kappa s}(\mathbf{q})$ and $\phi_s(\mathbf{q})$ are non-trivial functions of unperturbed particle energies and potential parameters that we determined explicitly.

Apart from the quantitative utility of result (3), a systematic analysis yields a general characterization of resulting band configurations depending on the chosen parameters. For this purpose we first consider the splitting of three-fold degenerate crossings of the unperturbed spectrum at high-symmetry point κ (κ'), i.e., $\mathbf{q} = \mathbf{0}$. The potential parameters can be grouped with regard to behaviour under spatial inversion into symmetric (u, m', a') and asymmetric (u', m, a). The possible band configurations of the symmetric case are shown in Fig. 2. Similarly, we study how the purely asymmetric case breaks the remaining degeneracy and finally how the global band structure can be extrapolated.

Our current and future research is aimed at (i) investigating the physical contexts of this and similar models and (ii) extending our analytical results to physical observables and possible relations to band topology, and (iii) study magnetic field effects.

- ¹ A. K. A. Geim and K. S. K. Novoselov, *The rise of graphene*, Nature materials **6**, 183 (2007), ISSN 1476-1122, 0702595.
- ² A. H. Castro Neto, F. Guinea, N. M. R. Peres, K. S. Novoselov, and A. K. Geim, *The electronic properties of graphene*, Rev. Mod. Phys. **81**, 109 (2009), ISSN 00346861, 0709.1163, URL <http://link.aps.org/doi/10.1103/RevModPhys.81.109>.
- ³ S. Balendhran, S. Walia, H. Nili, S. Sriram, and M. Bhaskaran, *Elemental analogues of graphene: Silicene, germanene, stanene, and phosphorene*, Small **11**, 640 (2015), ISSN 16136829.
- ⁴ M. Z. Hasan and C. L. Kane, *Colloquium: Topological insulators*, Reviews of Modern Physics **82**, 3045 (2010), ISSN 00346861, 1002.3895.
- ⁵ L. Fu, *Topological crystalline insulators*, Physical Review Letters **106**, 1 (2011), ISSN 00319007, 1010.1802.
- ⁶ C. C. Tsuei and J. R. Kirtley, *Pairing symmetry in cuprate superconductors*, Reviews of Modern Physics **72**, 969 (2000), ISSN 0034-6861, 0002341, URL <http://rmp.aps.org/abstract/RMP/v72/i4/p969>{_}1\$backslash\$nhttp://link.aps.org/doi/10.1103/RevModPhys.72.969.
- ⁷ A. K. Geim and I. V. Grigorieva, *Van der Waals heterostructures.*, Nature **499**, 419 (2013), ISSN 1476-4687,

1307.6718, URL <http://www.ncbi.nlm.nih.gov/pubmed/23887427>.

- ⁸ K. S. Novoselov, A. Mishchenko, A. Carvalho, A. H. C. Neto, and O. Road, *2D materials and van der Waals heterostructures*, Science **353**, aac9439 (2016), ISSN 0036-8075, arXiv:1411.1235v1.
- ⁹ J. R. Wallbank, *Electronic properties of graphene heterostructures with hexagonal crystals* (Springer, 2014), ISBN 978-3-319-07721-5, URL <http://link.springer.com/10.1007/978-3-319-07722-2>.
- ¹⁰ M. Mucha-Kruczyński, J. R. Wallbank, and V. I. Fal'ko, *Moiré miniband features in the angle-resolved photoemission spectra of graphene/hBN heterostructures*, Physical Review B **93**, 085409 (2016), ISSN 2469-9950, URL <http://link.aps.org/doi/10.1103/PhysRevB.93.085409>.
- ¹¹ P. Moon and M. Koshino, *Electronic properties of graphene hexagonal boron nitride moiré superlattice*, Phys. Rev. B **90**, 155406 (2014), 1406.0668, URL <http://arxiv.org/abs/1406.0668>.
- ¹² D. S. L. Abergel, J. R. Wallbank, X. Chen, M. Mucha-Kruczyński, and V. I. Fal'Ko, *Infrared absorption by graphene-hBN heterostructures*, New Journal of Physics **15** (2013), ISSN 13672630, arXiv:1309.2292v2.

New dynamical phase of matter from parametric driving of a BEC in a cavity

Paolo Molignini,¹ Luca Papariello,¹ Axel U. J. Lode,² and R. Chitra¹

¹*Institute for Theoretical Physics, ETH-Hönggerberg, CH-8093, Zürich, Switzerland*

²*Department of Physics, University of Basel, CH-4056 Basel, Switzerland*

We simulate the full time evolution of a parametrically modulated, laser-pump driven Bose-Einstein condensate in a dissipative high-finesse cavity. A new dynamical phase transition appears as a many-body parametric resonance. The new phase is linked to the dynamical normal phase (D-NP) of the parametrically modulated Dicke model. Energy profiles, density and correlations are studied, revealing prethermalized and thermalized regimes even in the presence of dissipation.

I. INTRODUCTION

The Dicke model is a paradigmatic example of collective behavior in quantum light-matter systems. It describes the interaction of N two-level atoms with a single bosonic cavity mode. In the thermodynamic limit $N \rightarrow \infty$, it undergoes a \mathbb{Z}_2 symmetry breaking quantum phase transition¹: at a critical atom-field coupling, the system moves from a normal phase (NP) containing few excitations to a superradiant phase (SP), which shows a macroscopic photonic occupation. Recently, parametric modulation of the Dicke model was shown to yield yet a new phase, termed dynamical normal phase (D-NP). In the D-NP the order parameter is on average zero but it dynamically oscillates between the two inequivalent superradiance configurations, with the system periodically emitting pulses of photons with opposite phases².

A candidate system for observing the D-NP is a laser-pump driven Bose-Einstein condensate placed in an optical trap and dispersively coupled to a high-finesse optical cavity. For a static pump driving, this system has already been shown to host a Dicke phase transition in the mean-field limit³. In the normal phase, the order parameter is vanishing small and the BEC sits in a Thomas-Fermi distribution at the bottom of the trapping potential. When the atomic pump power exceeds a threshold value, the condensate spontaneously orders in one of two possible checkerboard lattices with degenerate ground states. In the vicinity of the phase transition, the two phases can be mapped to the normal and superradiant phase of an effective Dicke model Hamiltonian under the assumption that only the lowest k -modes are populated³. The effective two-level states correspond then to the momentum states $|p_x, p_z\rangle = |0, 0\rangle$ (ground state) and $|\pm\hbar k, \pm\hbar k\rangle$ (scattered states) whose atomic density is modulated with a periodicity of half the pump wavelength.

II. METHODS

The BEC/cavity system consists of atoms in a trapping potential $V(\vec{r})$, interacting via a short ranged potential U . The atoms are driven by a transverse pump field described by the mode-function $h(\vec{r}) = \Omega_p \cos kz$ and the atomic detuning Δ_a . The BEC also interacts with the light field given by bosonic operators $\hat{a}^{(\dagger)}$, which describe

the cavity field in a rotating frame with a pump-cavity detuning Δ_c and strength Ω_c . Other two effective lattice potentials for the BEC arise from the cavity field (with mode-function $g(\vec{r}) \propto \cos kx$) and the interference pattern between cavity and pump field. This system can be thus described by the following Hamiltonian³:

$$\begin{aligned} \mathcal{H}_{\text{BEC}} = & \int d^3r \hat{\Psi}^\dagger(\mathbf{r}) \left\{ -\frac{\hbar^2}{2m} \nabla^2 + V(\mathbf{r}) + \right. \\ & \left. + \frac{U}{2} \hat{\Psi}^\dagger(\mathbf{r}) \hat{\Psi}(\mathbf{r}) \right\} \hat{\Psi}(\mathbf{r}) - \hbar \Delta_c \hat{a}^\dagger \hat{a} - \hbar \Omega_c (\hat{a} + \hat{a}^\dagger) \\ & + \int d^3r \hat{\Psi}^\dagger(\mathbf{r}) \left\{ \frac{\hbar}{\Delta_a} [\hbar^2(\mathbf{r}) + g^2(\mathbf{r}) \hat{a}^\dagger \hat{a} + \right. \\ & \left. + h(\mathbf{r})g(\mathbf{r})(\hat{a} + \hat{a}^\dagger)] \right\} \hat{\Psi}(\mathbf{r}) \end{aligned} \quad (1)$$

A dissipative decay term κ describing the photon leakage from the cavity can be included *a posteriori* in the equations of motion. We have investigated the parametrically modulated version of Hamiltonian (1), where the pump has an explicit periodic time dependence: $\Omega_p(t) = \Omega_p(1 + \alpha \cos(t))$. Because of the mapping between the BEC in a cavity and the Dicke model, we expect to observe a D-NP regime in the parametrically modulated Hamiltonian (1). Simulations of the BEC-cavity system are practical because this model can be directly realized in an experiment with cold atoms³⁻⁵. Moreover, a full time-evolution of this model can be computed numerically with the variational MultiConfigurational Time-Dependent Hartree method (MCTDH-X)^{6,7}, which enables us to probe non-mean field regimes.

III. RESULTS

We have first simulated the BEC in a cavity driven by a static pump for different values of the pump power Ω_p and cavity detuning Δ_c to obtain the diagram of the Dicke phase transition. We have then periodically driven the system by modulating the amplitude of the pump laser around two frequencies pertaining to the NP and SP, obtaining dynamical phase diagrams (*e.g.* figure 1). For both starting phases, the system undergoes a phase transition to the D-NP phase, appearing as many-body parametric resonances (Arnold tongues).

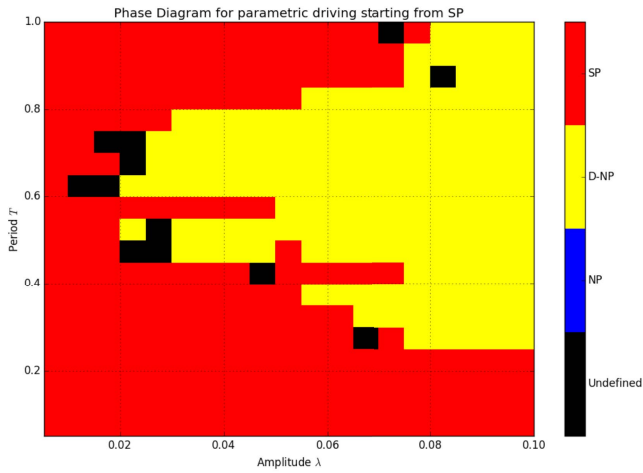


FIG. 1: Phase diagram of a parametrically driven BEC in a cavity for $N=1000$ bosons and various driving amplitude and periods, driven from the SP.

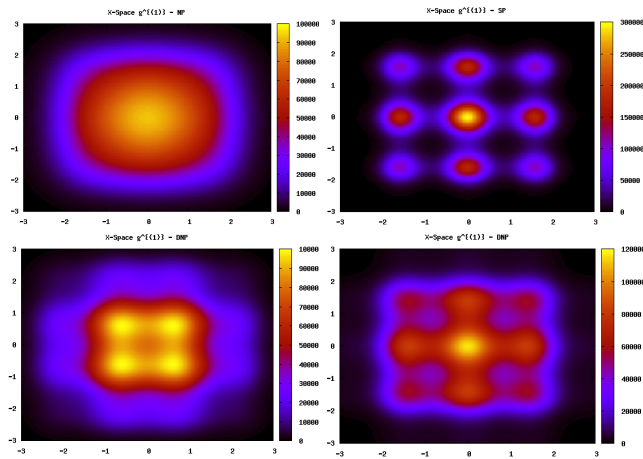


FIG. 2: Single-particle density matrix of a BEC in a cavity in the NP (upper left panel), SP (upper right panel) and D-NP (lower panels) phases.

We then analyzed the energy profile, density and correlations as a function of time. Some results are shown in figures 2 and 3. In the NP the BEC sits at the bottom of the harmonic potential and in the SP it chooses either one of the two sublattices. In the D-NP phase the BEC

oscillates instead between even and odd sites. The SP and NP phases show no heating under parametric modulation, but the D-NP phase has different thermalization properties depending on the starting phase. When driven from an initial NP, pre-thermalization states with beating patterns arise, but in the long-time regime the system eventually thermalizes. Driving from the SP leads instead to very quick and strong heating.

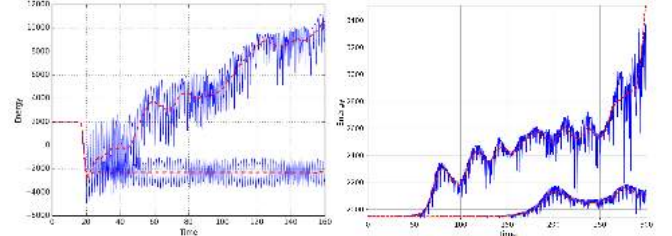


FIG. 3: Time evolution of the energy and its running average in the parametrically driven D-NP starting from SP and NP (left/right panel). The oscillating curve at constant average on the left panel refers to the system in the dynamically driven SP (dynamically driven NP not shown).

IV. CONCLUSIONS

We have investigated the full time evolution of a parametrically modulated, laser-pump driven BEC in a dissipative high-finesse cavity. The D-NP phase was shown to exist in this system and its phase boundaries delineate Arnold instability lobes. Modulated normal and superradiant phases are resistant to heating at the mean field level. The D-NP phase shows prethermalization and thermalizes to infinite temperature even in the presence of dissipation. Future directions include further analyses of the nature of the NP/D-NP and SP/D-NP phase transitions from correlation functions, the study of the effect of particle number and simulations beyond mean field.

Acknowledgments

We would like to thank Tobias Donner for useful discussions. This project is supported by SNF, Mr. Giulio Anderheggen and the ETH Zürich Foundation.

¹ K. Hepp and E. Lieb, Phys. Rev. **8**, 2517 (1973).
² R. Chitra and O. Zeitler, Phys. Rev. A **92**, 023815 (2015).
³ K. Baumann, C. Guerlin, F. Brennecke, and T. Esslinger, Nature **464**, 1301 (2010).
⁴ K. Baumann, R. Mottl, F. Brennecke, and T. Esslinger, Phys. Rev. Lett. **107**, 140402 (2011).

⁵ F. Brennecke, R. Mottl, K. Baumann, R. Landig, T. Donner, and T. Esslinger, PNAS **110** (29), 11763 (2013).
⁶ O. E. Alon, A. I. Streltsov, and L. Cederbaum, Phys. Rev. A **77**, 033613 (2007).
⁷ URL <http://ultracold.org>.

Quantum Hall Polaritons

Patrick Knüppel,¹ Sylvain Ravets,¹ Stefan Faelt,^{1,2} Martin Kroner,¹ Werner Wegscheider,² and Ataç Imamoglu¹

¹*Institute of Quantum Electronics, ETH-Hönggerberg, CH-8093, Zürich, Switzerland*

²*Solid State Laboratory, ETH Hönggerberg, CH-8093 Zürich, Switzerland*

Elementary excitations of a two-dimensional electron gas can be described as exciton-polarons. Excitons are dressed by Fermi-sea electron-hole pairs due to exciton-electron interactions. In large magnetic fields, Landau quantization and electron correlations lead to rich many-body physics in the quantum Hall regime. We couple a two-dimensional electron gas to an optical cavity. On the one hand, we examine possible photon-nonlinearity induced by the electronic system. On the other hand, cavity spectroscopy enables us to study quantum Hall physics in the bulk using light.

I. INTRODUCTION

Exciton-polaritons are half-light half-matter quasiparticles that allowed investigating many intriguing phenomena, for example nonequilibrium condensation and superfluidity of light¹. Owing to their excitonic part, polaritons show intrinsic nonlinearities due to Coulomb interactions and phase-space filling. They might find applications in integrated devices and quantum simulators^{2,3}. One major goal of the field is to engineer strong light-light interactions to reach polariton blockade, where the presence of only one polariton in the system blocks a second excitation.

We try to enhance the photon nonlinearity in a system with a finite electron density where polarons instead of bare excitons are coupled to the photons, creating polaron-polaritons⁴⁻⁶. In turn, the polaron-polaritons carry signatures of the electronic system that can now be studied optically⁵.

II. SAMPLE AND EXPERIMENTAL SETUP

The elementary excitation of a semiconductor quantum well (QW) is a bound pair of electron and hole called exciton. It carries a dipole moment and interacts with electromagnetic fields. Placing the QW at the antinode of an optical microcavity confines the photons around the QW and thus enhances the exciton-photon interactions. If the exciton-photon coupling rate exceeds the exciton and photon decay and decoherence rates, strong coupling is reached. At the exciton-photon resonance, polaritons are formed, which are mixed light-matter quasiparticles. We study a doped GaAs QW structure containing a finite electron density n_e . This two-dimensional electron gas (2DEG) can rearrange to screen the excitons and lower their transition energy. These excitons dressed by 2DEG excitations (polarons) are sensitive to properties of the many-body 2DEG state. The 2DEG properties are mostly studied with transport measurements, we try to use cavity spectroscopy as a complementary tool (FIG. 1). We use polaritons in this system to extract signatures of the many-body ground state by detecting photons leaking out of the microcavity from decaying polaritons.

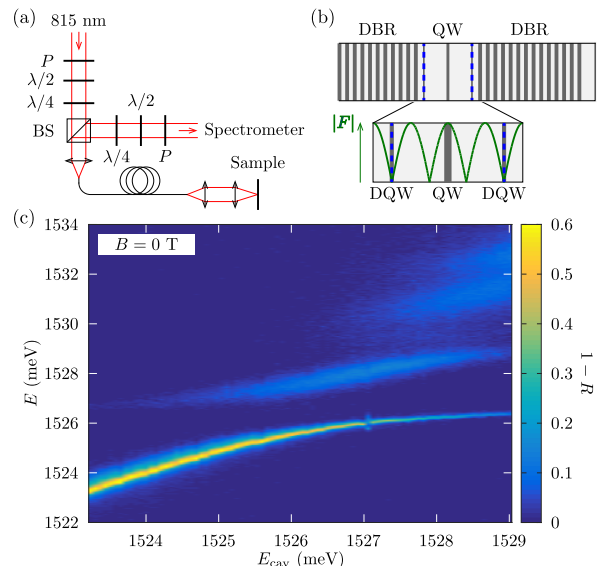


FIG. 1: Polaron-polaritons in a GaAs QW⁷. (a) Fiber-based confocal microscope for polarization resolved absorption measurements. The sample is placed in a dilution refrigerator with 30 mK base temperature. (b) Structure of the MBE-grown sample containing a microcavity formed by a pair of DBRs. The GaAs QW is centered at an antinode of the optical field and surrounded by two doping quantum wells (DQW). (c) Absorption spectrum when tuning the cavity frequency shows an avoided crossing and thus the formation of polaron-polaritons.

III. QUANTUM HALL REGIME

Introducing an external magnetic field B perpendicular to the 2DEG quantizes⁸ the electronic states into Landau levels (LLs) with energies $E_n = \hbar\omega_c(n + 1/2)$. Each LL has a degeneracy eB/h and the filling factor $\nu = hn_e/(eB)$ specifies how many of the LLs are occupied by electrons. Measuring absorption spectra while tuning the magnetic field (FIG. 2) reveals clear signatures of the 2DEG states. Left-hand circularly polarized light σ^- probes transitions to the lower Zeeman spin subband and right-hand circularly polarized light σ^+ to the higher Zeeman spin subband. So the way electrons are arranged in the LLs strongly influences the absorption spectra. At the integer state $\nu = 1$, we observe a collapse in the

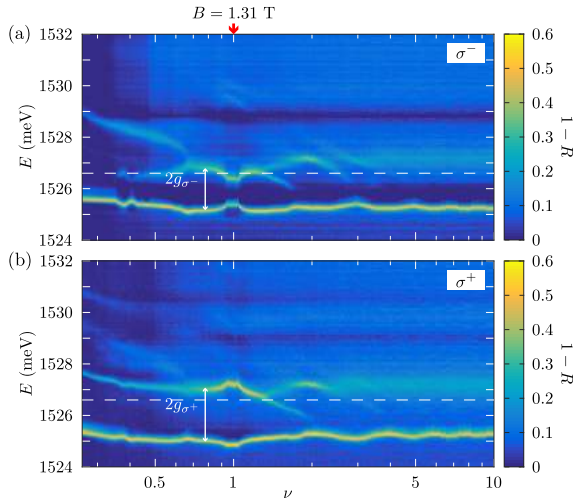


FIG. 2: Cavity spectroscopy for fixed cavity frequency (dashed line) and varying magnetic fields $B \propto \nu^{-1}$. Measurement in σ^- (a) and σ^+ (b) polarized light.

normal mode splitting g_{σ^-} and an increase in g_{σ^+} . This is expected since at $\nu = 1$ the lowest LL is completely filled, forbidding any further excitation in σ^- , while all states corresponding to the σ^+ transition are free. More generally, we can extract the spin polarization

$$P = \frac{g_{\sigma^+}^2 - g_{\sigma^-}^2}{g_{\sigma^+}^2 + g_{\sigma^-}^2} \quad (1)$$

of the underlying electronic state by comparing FIG 2(a) and (b). While the electron polarization at integer filling

factors directly translates to the optical spectrum, the case is more complicated for fractional states. One cannot expect a vanishing normal mode splitting from this phase space filling argument at partially filled LLs. Instead, the polaron nature of the excitation needs to be considered. In a polarized state, a lack of electrons in the opposite spin state might lead to a vanishing coupling constant g for one of the polarizations⁷, because there are no electrons available to screen the excitation.

IV. OUTLOOK

As a next step, we will try to characterize the photon nonlinearity in the quantum Hall regime. The large line shifts induced by the presence of integer and fractional quantum Hall states should lead to an enhanced nonlinear effect at certain magnetic fields. At higher magnetic fields, we might be able to investigate quantum Hall physics using cavity spectroscopy. In the future, we want to look for optical signatures of incompressibility in fractional states. A possible extension is the optical manipulation of anyonic quasiparticles associated with strongly correlated phases.

Acknowledgments

The Authors acknowledge many useful discussions with Hadis Abbaspour, Valentin Goblot, Sina Zeytinoglu and Wolf Wuester. This work was supported by NCCR Quantum Photonics (NCCR QP), an ETH Fellowship (S. R.), and an ERC Advanced investigator grant (POLT-DES).

¹ H. Deng, H. Haug, and Y. Yamamoto, *Exciton-polariton bose-einstein condensation*, Reviews of Modern Physics **82**, 1489 (2010).
² D. Sanvitto and S. Kéna-Cohen, *The road towards polaritonic devices*, Nature Materials **15**, 1061 (2016).
³ A. Aspuru-Guzik and P. Walther, *Photonic quantum simulators*, Nature Physics **8**, 285 (2012).
⁴ R. Schmidt, T. Enss, V. Pietilä, and E. Demler, *Fermi polarons in two dimensions*, Phys. Rev. A **85**, 021602 (2012).
⁵ S. Smolka, W. Wuester, F. Haupt, S. Faelt, W. Wegscheider, and A. Imamoglu, *Cavity quantum electrodynamics with many-body states of a two-dimensional electron gas*, Science **346**, 332 (2014).
⁶ M. Sidler, P. Back, O. Cotlet, A. Srivastava, T. Fink,

M. Kroner, E. Demler, and A. Imamoglu, *Fermi polaron-polaritons in charge-tunable atomically thin semiconductors*, Nature Physics (2016).

⁷ S. Ravets, S. Faelt, M. Kroner, W. Wegscheider, and A. Imamoglu, *Polaron-Polaritons in the Integer and Fractional Quantum Hall Regimes*, ArXiv e-prints (2017), 1701.01029.

⁸ Given the 2DEG quality (electron mobility) is large enough such that $\omega_c \tau \gg 1$ can be achieved for the cyclotron frequency $\omega_c = eB/m$ and the electron relaxation time τ . Additionally, the temperature must be small compared to the cyclotron frequency: $k_B T \ll \hbar \omega_c$.

Detection of topological superconductivity via phase tunable noise in Josephson junctions

Roy Haller,¹ Vishal Ranjan,¹ Raphaëlle Delagrangé,¹ Gergő Fülöp,¹ and Christian Schönenberger¹

¹*Institute of Physics, University of Basel, CH-4054, Basel, Switzerland*

The aim of my PhD is to develop a setup to detect topological superconductivity in a semi-conducting nanowire Josephson junction (JJ) by measuring its finite-frequency noise as a function of the superconducting phase difference ϕ . In contrast to a normal JJ, where the energy-phase relation of the supercurrent carrying Andreev bound states (ABS) is 2π -periodic, the ABS of a topological JJ shows a 4π -periodicity. We aim the detection of topological superconductivity by measuring finite frequency noise around the topologically protected crossing. One expects an increase of noise at this crossing point, whereas in a conventional JJ noise will be (formally) zero at the anti-crossing point. To perform these measurements, we will introduce the nanowire in a superconducting loop, itself inductively coupled to a high frequency resonator.

I. INTRODUCTION

A supercurrent can flow between two superconductors even if they are separated by a normal metal section (shorter than the superconducting coherence length) at equilibrium via so-called Andreev bound states (ABS) and a Josephson junction (JJ) is formed. The ABS energies $E_{\pm}^{\text{ABS}}(\phi)$ for a single mode JJ depend on the phase difference ϕ between the superconductors and are given by

$$E_{\pm}^{\text{ABS}}(\phi) = \pm\Delta\sqrt{1 - D\sin^2(\phi/2)}, \quad (1)$$

where Δ is the superconducting gap energy and D the transmission probability.

In contrast to a normal JJ ($D < 1$), where the energy-phase relation of the two ABS is 2π -periodic, the ABS of a topological JJ show a 4π -periodicity. This originates from the fact that the topological ABS are immune to back scattering ($D = 1$). Therefore topologically protected energy levels cross at $\phi = (2n - 1)\pi$ ($n \in \mathbb{Z}$), while they anti-cross in case of a conventional JJ (see Fig. 1).

Furthermore, transitions between the two ABS parities are induced at finite temperature for the non-topological

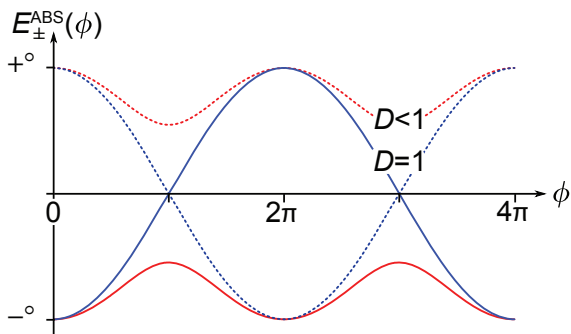


FIG. 1: Typical energy spectra $E_{\pm}^{\text{ABS}}(\phi)$ of Andreev bound states, as a function of the phase difference ϕ in the Josephson junction. The gapless 4π -periodic topological mode corresponds to the blue line, whereas the gapped 2π -periodic non-topological mode is indicated red.

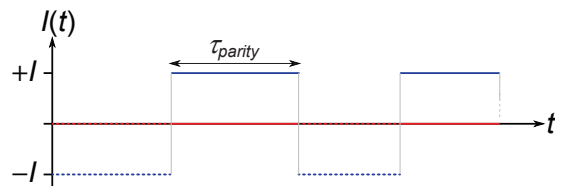


FIG. 2: Supercurrent $I(t)$ as a function of time t for the topological (non-topological) mode at the crossing (anti-crossing) point where $\phi = (2n - 1)\pi$ ($n \in \mathbb{Z}$) is sketched in blue (red). The current changes sign when the parity is swapped and remains constant over the parity lifetime τ_{parity} .

mode as well as for the topological mode. The parity lifetime τ_{parity} describes the time interval between those parity swaps and is determined by unavoidable quasiparticle poisoning. Albrecht *et al.*¹ investigated effects of quasiparticle poisoning in the topological mode and estimated $\tau_{\text{parity}} \approx 1 \mu\text{s}$.

Moreover, the current-phase relation is proportional to the derivative of the parity energy with respect to phase, resulting in a sign change of the current for each parity swap.² However, in a conventional JJ there is no current carried by either parity at the anti-crossing point. Hence, there are no current fluctuations and noise will be (formally) zero. Whereas for a topological JJ, phase biased to the crossing point, the sign of the current is always changing with state transitions. On average the current will be zero as well, however in time scales, smaller than τ_{parity} , current will be finite resulting in telegraphic noise (see Fig. 2).

II. EXPERIMENTAL REALISATION

In an arrangement of a superconducting loop interrupted by a JJ (rf-SQUID), the phase difference across the junction can be tuned via magnetic flux penetrating through the loop. Since rf-SQUIDS are extremely sensitive to magnetic field, only a small magnetic field needs to be applied, which will be provided by an on-chip current biased dc line next to the loop.

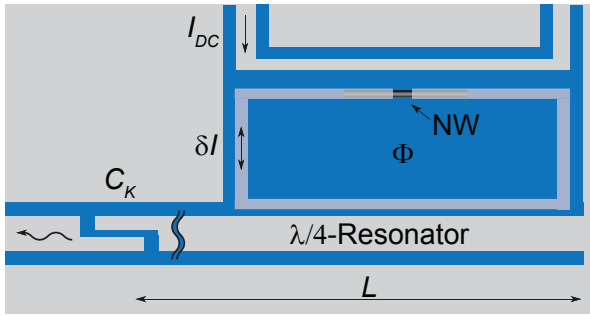


FIG. 3: Sketched sample arrangement for a phase tunable Josephson junction inductively coupled to a $\lambda/4$ -resonator. A dc flux line carrying the current I_{DC} generates a magnetic flux Φ within the superconducting loop to control the phase difference ϕ across the Josephson junction formed by a nanowire. The supercurrent fluctuations δI are transfer via the resonator and measured with a high frequency setup.

Current fluctuations within the time scale of τ_{parity} would correspond to a required measurement frequency at least of the order of MHz, which is not provided by normal dc measurements. Therefore our approach is to couple the phase tunable JJ to a superconducting coplanar transmission line (CTL) resonator. The shortest version of a CTL resonator is the so-called $\lambda/4$ -resonator, which consists of an open and a short end. Both ends act as mirrors for electromagnetic waves and the distance L between them defines the fundamental resonance frequency. However, photons are coupled to the measurement setup via the coupling capacitor C_K , where the voltage is maximum. On the short end current is maximal and therefore sensitive to magnetic field fluctuations, which are generated by current fluctuations in the phase biased rf-SQUID. Hence, the rf-SQUID is inductively coupled to the $\lambda/4$ -resonator.

This kind of geometry has already been used by Janvier *et al.*⁴ in the non-topological regime. Dmytruk *et al.*³ de-

scribe theoretically the interaction between a topological superconducting ring with a microwave cavity.

Since the central frequency of the high frequency components built-in our dilution refrigerator measurement setup is ~ 3 GHz, the resonator's fundamental resonance frequency should be engineered to this value.

A semiconducting nanowire with large spin-orbit interaction proximity connected to the superconducting loop will offer the tunability between the normal and the topological JJ by applying an in-plane magnetic field.⁵ Moreover, with gate lines the density of states in the nanowire can be tuned as well as the tunnel couplings.

III. OUTLOOK

In a first step, measurements will be performed with a rf-SQUID consisting of a normal metal JJ to investigate the dynamics of the resonator compared to simulated and calculated circuit parameters. The effect of the rf-SQUID's changing kinetic inductance on the resonator can be studied. Subsequently, the superconducting material as well as its thickness need to be adapted such that the device sustains in-plane magnetic fields. Later on, a fast flux line will offer adiabatic tunability of the JJ.

Acknowledgments

We would like to thank the National Centre of Competence in Research – Quantum Science and Technology (NCCR–QSIT), the Swiss National Science Foundation (SNF) and the Swiss Nanoscience Institute (SNI).

¹ S. Albrecht, E. Hansen, A. Higginbotham, F. Kuemmeth, T. Jespersen, J. Nygård, P. Krogstrup, J. Danon, K. Flensberg, and C. Marcus, *Transport signatures of quasiparticle poisoning in a majorana island*, *Physical Review Letters* **118**, 137701 (2017).

² A. Golubov, M. Y. Kupriyanov, and E. Il'ichev, *The current-phase relation in josephson junctions*, *Reviews of Modern Physics* **76**, 411 (2004).

³ O. Dmytruk, M. Trif, and P. Simon, *Josephson effect in topological superconducting rings coupled to a microwave*

cavity, *Physical Review B* **94**, 115423 (2016).

⁴ C. Janvier, L. Tosi, L. Bretheau, Ç. Girit, M. Stern, P. Bertet, P. Joyez, D. Vion, D. Esteve, M. Goffman, et al., *Coherent manipulation of andreev states in superconducting atomic contacts*, *Science* **349**, 1199 (2015).

⁵ V. Mourik, K. Zuo, S. M. Frolov, S. Plissard, E. Bakkers, and L. P. Kouwenhoven, *Signatures of majorana fermions in hybrid superconductor-semiconductor nanowire devices*, *Science* **336**, 1003 (2012).

Quantum interface between single optical and microwave photons

Yuta Tsuchimoto,¹ Patrick Knüppel,¹ Sun Zhe,¹ Aymeric Delteil,¹
Martin Kroner,¹ Atac Imamoglu,¹ Klaus Ensslin,² and Andreas Wallraff²

¹*Institute of Quantum Electronics, ETH-Hönggerberg, CH-8093, Zürich, Switzerland*

²*Laboratory for Solid State Physics, ETH-Hönggerberg, CH-8093, Zürich, Switzerland*

We propose a fast quantum interface to interconvert single optical and microwave photons. The interface comprises a coupled quantum dot (CQD) and a superconducting (SC) cavity. Since a CQD has large coupling strength to a SC cavity and fast decay rate to optical field, the interface realizes fast interconversion of several nanoseconds as well as high conversion efficiency. The unprecedented transfer speed along with the high conversion efficiency make this system promising for future use of quantum networks based on SC qubits.

I. INTRODUCTION

Quantum networks are promising platforms which realize long-distance quantum communication and distributed quantum computing. A lot of works have been dedicated to build the systems for decades. The goal of those works is to transmit quantum information between long-distance nodes and also to precisely manipulate the information in each node. The former is realized by using optical photons in fibers, which transmit quantum information with low-losses. For the later, superconducting (SC) qubits working on microwave regime are strong candidates. Recent emerging demand is to develop interfaces which connect those two different frequency regimes for linking distributed SC qubits with optical photons in fibers. To do so, one has to realize efficient interconversion between single optical and microwave photons. Several systems aiming to such a conversion have been studied. The nanomechanical membrane system has demonstrated bi-directional conversion and experimentally shown the highest conversion efficiency of 0.1 with a bandwidth of 30 kHz, so far². From the view point of long-distance communication, it is essential to increase not only conversion efficiency but also transfer speed. We propose a novel quantum interface consisting of CQDs and a SC cavity which realizes not only high conversion efficiency but also fast transfer speed. CQDs have large decay rate to optical field (several hundreds of MHz) and coupling strength to a SC cavity (several hundreds of MHz). These features enable to realize fast conversion speed as well as high conversion efficiency.

II. STRUCTURE OF THE INTERFACE

Figure 1 shows the design for our quantum interface. The interface consists of a CQD and a SC coplanar waveguide cavity. The CQD couples to both microwave and optical field and links microwave photons in the SC cavity with optical photons in a free space. The vertically aligned CQD is located in a defect of the SC cavity at an anti-node of the microwave field. The area of defect is as small as several μm^2 to minimize losses of microwave field. The CQD are sandwiched by a top gate

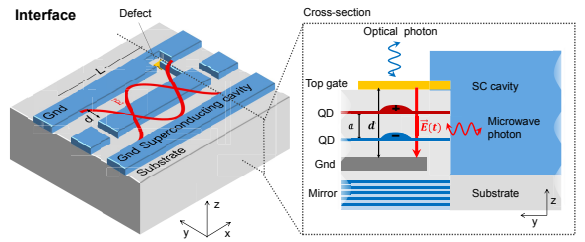


FIG. 1: Schematic of the quantum interface consisting of a CQD and a SC cavity. Whole image of the interface (left) and cross-section image of the defect geometry (right) in the interface.

and ground plane as shown in the cross-section image. The electrodes enable to control the charging state of the CQD with an applied voltage. Resonant tunnel coupling of the CQD hybridizes the electronic states of the two dots and leads to the formation of an exciton with a hole located in one dot and a delocalized electron. Such an exciton not only has a large optical coupling strength but also carries a large dipole moment lying along the z -axis. This dipole is several orders of magnitude larger than that of single QDs or Rb atoms and can couple to the SC microwave field. To efficiently couple this large dipole moment to SC microwave field, we use the defect geometry shown in the cross-section image. The top gate and ground plane matches the direction of the SC microwave field \vec{E} with the CQD dipole moment. Furthermore, by choosing small separation between the top gate and ground, one can enhance the SC microwave field between those electrodes, resulting in strong interaction of the SC microwave field and the dipole. Optical photons are emitted from or absorbed into the CQD by exciting an optical dipole lying in the xy plane through the thin top gate. To enhance the optical coupling of the CQD with free space, the interface has an optical mirror under the ground plane. The mirror modifies the radiation field mode of the CQD and matches it with the incident photon mode. This mode matching promotes the efficient absorption and collection of the optical photons.

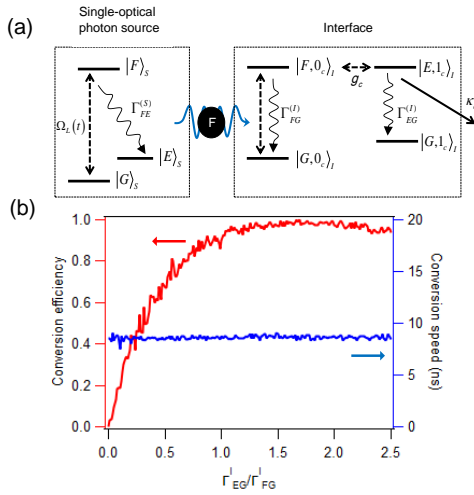


FIG. 2: (a) Optical to microwave conversion scheme. (b) Calculated conversion efficiency (right axis) and speed (left axis) as a function of Γ_{EG}/Γ_{FG} . For the calculation, we set the realistic system parameters as follows: $\Gamma_{FG}^{(I)}/2\pi = 300$ MHz, $g_c/2\pi = 200$ MHz, $\kappa_c/2\pi = 3$ MHz.

III. SINGLE PHOTON CONVERSION

Figure 2(a) shows an optical to microwave conversion scheme. The system consists of a single-optical photon source and the interface. The photon source has simple three-level system denoted by $|G\rangle_S$, $|E\rangle_S$, and $|F\rangle_S$. A continuous wave (CW) laser excites $|G\rangle_S$ to $|F\rangle_S$ with a laser Rabi frequency ω_L , and the excited state $|F\rangle_S$ spontaneously relaxes into $|G\rangle_S$ or $|E\rangle_S$ with decay rates Γ_{FG} or Γ_{FE} . Generated single-optical photons from the $|F\rangle_S \rightarrow |E\rangle_S$ transition resonantly couples to the interface as described before. The interface consists of a CQD with three-level λ system and a SC cavity. $|G\rangle_I$ denotes the ground state of the CQD. $|E\rangle_I$ and $|F\rangle_I$ are the bonding and anti-bonding state generated from the tunnel coupling. $|F\rangle_I$ spontaneously relaxes into $|G\rangle_I$ or $|E\rangle_I$ with decay rate Γ_{FG} or Γ_{FE} , respectively. $|E\rangle_I$ decays into $|G\rangle_I$ with the decay rate Γ_{EG} . Frequency difference between $|E\rangle_I$ and $|F\rangle_I$ corresponds with the resonant frequency of the SC cavity. $|0_c\rangle_I$ and $|1_c\rangle_I$ are states where the SC cavity has zero or one microwave photon. The microwave photons leave the cavity with decay rate κ_c . The state $|F,0_c\rangle_I$ and $|E,1_c\rangle_I$ interact with each other with a coupling strength g_c derived from the interaction between the SC

microwave field and the dipole. The interface absorbs single-optical photons through $|G,0_c\rangle_I \rightarrow |F,0_c\rangle_I$ transition and converts them into single-microwave photons through $|F,0_c\rangle_I \rightarrow |E,1_c\rangle_I$ transition. The efficiency and speed of this conversion is determined by various dissipative processes and coupling strengths. We estimated conversion efficiency and speed using the quantum monte carlo method. Figure 2(b) shows the conversion efficiency and speed as a function of $\Gamma_{EG}^{(I)}/\Gamma_{FG}^{(I)}$. The efficiency reaches almost unity, indicating that this system realizes efficient optical to microwave conversion. As well as the high conversion efficiency, the system realizes fast conversion speed of less than 10 ns. This speed is 10^3 times faster than previously reported results.

Figure 3(a) shows a microwave to optical conversion scheme. The interface initially has a microwave photon in the SC cavity. A CW laser excites the $|G,1_c\rangle_I \rightarrow |E,1_c\rangle_I$ transition. Single-microwave photons gain this energy and are upconverted into optical photons. Figure 3(b) shows the conversion efficiency and speed. The maximum conversion efficiency reaches almost unity. The conversion speed is again less than 10 ns. The results shown in FIGs. 2 and 3 indicate that the system allows to demonstrate fast conversion speed of several nanoseconds as well as almost unity conversion efficiency for both optical to microwave and microwave to optical conversions. We will discuss further details in our presentation.

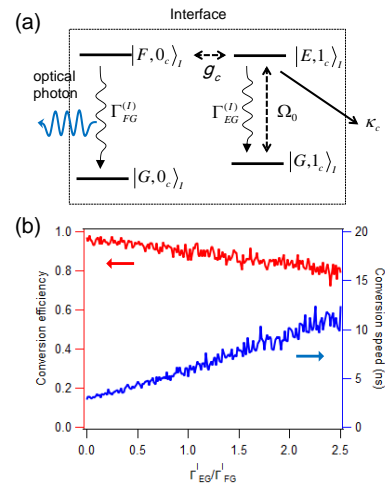


FIG. 3: (a) Microwave to optical conversion scheme. (b) Calculated conversion efficiency and speed. The system parameters used here are same as shown in the caption of FIG. 1.

Correlation measurement of THz photons using GaAs based waveguide

Francesca Fabiana Settembrini,¹ Ileana-Cristina Benea-Chelms,¹ Giacomo Scalari,¹ and Jérôme Faist¹

¹*Institute of Quantum Electronics, ETH-Hönggerberg, CH-8093, Zürich, Switzerland*

Photon correlation measurements are crucial in order to study the quantum nature of light. In the THz range such measurements have been implemented using electro-optic sampling combined with two ultrashort pulses. The sensitivity of this detection scheme is limited by the use of a bulk non-linear crystal. We propose a solution for the improvement of the setup based on a GaAs waveguide as the non-linear element, in order to achieve single-photon sensitivity in a wide range of frequencies.

I. INTRODUCTION

The quantum nature of a source is often reflected in the temporal distribution of the emitted photons. Very useful quantities to characterize the statistical and coherence properties of an electro-magnetic field are the correlation functions.

The *intensity correlation function*:

$$g^{(2)}(\tau) = \frac{\langle \hat{E}^-(t)\hat{E}^-(t+\tau)\hat{E}^+(t+\tau)\hat{E}^+(t) \rangle}{\langle \hat{E}^-(t)\hat{E}^+(t) \rangle \langle \hat{E}^-(t+\tau)\hat{E}^+(t+\tau) \rangle} \quad (1)$$

gives information about the photon statistics and the output shape of the emission. According to its value at $\tau = 0$ it is possible to distinguish between bunched, coherent and anti-bunched light.

Measurements of the $g^{(2)}(\tau)$ are usually performed in the optical range using a Hanbury-Brown-Twiss setup. Unfortunately such detection scheme is difficult to implement in the THz range, due to the lack of sufficiently fast detectors. An alternative approach to this type of measurement involves the use of electro-optic sampling¹.

II. MEASUREMENT SCHEME

A. Electro-optic sampling

Electro-optic sampling is a non-destructive technique which allows to sample in real time a THz wave through its interaction with an ultrashort probe pulse in a $\chi^{(2)}$ material. The THz field which propagates in the crystal induces a birefringence, causing the two components of the polarization of the probe to acquire a phase shift. The latter can be measured directly through balanced detectors, retrieving so the intensity of the electric field through the relation²:

$$\frac{\Delta I}{I} = \frac{2\pi L_{crystal} n_{probe}^3 r E_{THz}}{\lambda_{probe}} \quad (2)$$

where ΔI and I are the difference and the sum of the current generated in the photodetectors, r the linear electro-optic coefficient of the crystal, $L_{crystal}$ its length

and n_{probe} its refractive index at the wavelength of the probe.

The intensity of the electro-optic signal is given by the formula³:

$$S(\tau) \propto L e^{i\Delta k L/2} \frac{\sin(\Delta k L/2)}{\Delta k L/2} \quad (3)$$

where Δk is the phase mismatch between the THz light and the probe pulse and L is the length of the crystal. The length of the crystal for which the electro-optic signal is maximum, which occurs when $\Delta k L/2 = \pi/2$, is referred to as *coherence length*.

B. Experimental setup

Electro-optic sampling, combined with two ultrashort femtoseconds pulses and fast detectors, has already been employed to measure the correlation functions of a THz QCL all over its dynamic range, which gives access to different types of photon statistics¹.

The THz light is sampled in the non-linear crystal by the two probe pulses, mutually delayed by a time τ (see Fig.1 (a)). The measured values of the THz field at t and $t+\tau$ are then used for a real time calculation of $g^{(1)}(\tau)$ and $g^{(2)}(\tau)$, carried out through a fast computation routine.

In order to enhance the sensitivity of the setup, we propose to replace the bulk nonlinear crystal with a waveguide based on GaAs ($r=1.5$ pV/m). A sketch of the possible experimental setup is reported in Fig.1. It presents several advantages, above all the enhancement of the overlap between the probe pulses and the THz radiation and the possibility to engineer its coherence properties by design.

As can be seen in Fig.2, the presence of a double metal layer allows the plasmonic enhanced confinement of the THz light uniformly in the center of the waveguide (Fig.2 (a)) and a patterned AlGaAs layer causes the probe beams to propagate parallel to each other inside the waveguide (Fig.2 (b)). This configuration allows the probe pulses to overlap with high values of the THz field and so sample them. At the same time it enables them to remain separated, avoiding crosstalk effects, which would compromise the computation of the photon statistics.

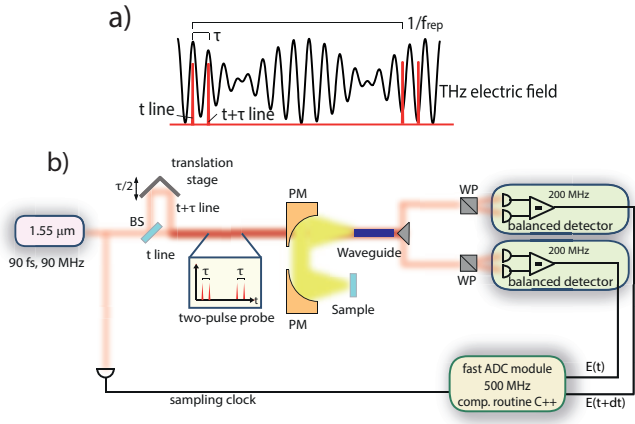


FIG. 1: (a) Electro-optic sampling: the subcycle resolution of the measurement is limited by the width of the probe pulses¹. (b) Sketch of the proposed experimental setup, employing 90 fs pulses and ultrafast acquisition at the repetition rate of the laser (90 MHz). The time average in Eq.(1) can be replaced by the average over the entire set of acquired data.

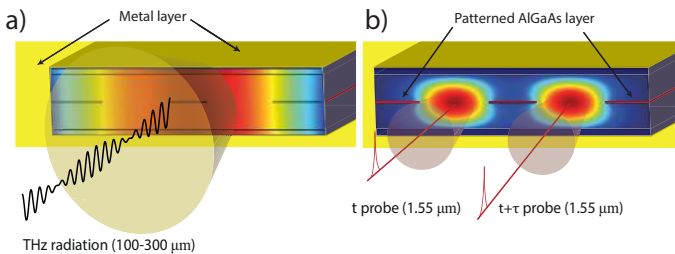


FIG. 2: Simulated intensity profiles of the guided modes in a $12\mu\text{m} \times 70\mu\text{m}$ waveguide. (a) Fundamental mode of the THz radiation (b) Fundamental mode of the NIR probe pulses.

A good indication of the sensitivity of the setup is given by the inverse ratio between the *noise equivalent field* (the electric field needed to obtain a variation in the signal equal to the shot noise (see Eq. 2)) and the *vacuum field fluctuation*:

$$\Delta \bar{E}_{vac} = \sqrt{\frac{h\nu_c \Delta\nu_c}{2n_{THz} \epsilon_0 c A_{eff}}}. \quad (4)$$

This quantity depends strongly on the central frequency ν_c , the bandwidth $\Delta\nu_c$ and the cross section A_{eff} of the cavity. The intensity of the vacuum fluctuation detectable through electro-optic sampling depends strongly

on the dimensions of the non linear element. The phase-matching condition between the probe pulses and the THz radiation (Eq.(3)) can be easily tuned by changing the waveguide's width, as shown in Fig 3. These are obtained from simulations of the dispersion relation of the effective refractive index of the waveguide, carried out with Comsol 5.2.

For a waveguide 2 mm long and 70 μm wide, the predicted value for the ratio $\Delta \bar{E}_{vac}/E_{NEF}$ gives a result of

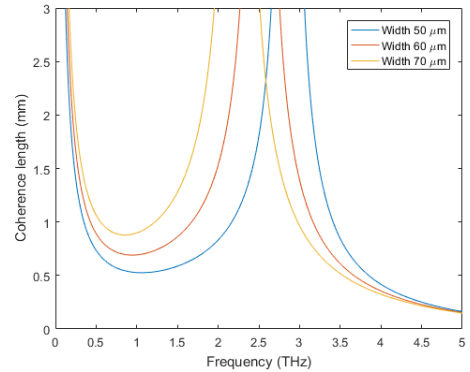


FIG. 3: Simulated coherence length of the electro optic signal reported as a function of the sampled THz field for different waveguide's width, from 50 μm to 70 μm .

3.2%. Such value represents a significant increase in the sensitivity of the setup, which at the moment reaches value of 0.6 %. This would allow us to directly sample and compute the correlation functions of the vacuum field.

III. OUTLOOK

The achievement of single photon sensitivity would allow us to study phenomena such as the production of photon pairs due to the non-adiabatic modulation of ultrastrong coupling in a light-matter system. It would also allow us perform a direct measurement of the correlation functions of the vacuum field.

Acknowledgments

We would like to thank QSIT, ERC Advanced grant "Quantum Metamaterials in the Ultra Strong Coupling Regime (MUSiC)" as well as SNSF.

¹ C. Benea-Chelmus, C. Bonzon, C. Maissen, G. Scalari, M. Beck, and J. Faist, *Subcycle measurement of intensity correlations in the terahertz frequency range*, Phys. Rev. A **93**, 043812 (2016).

² P. Plancken, H. Nienhuys, H. Bakker, and T. Wenckenbach, *Measurement and calculation of the orientation dependence*

of terahertz pulse detection in znte, J. Opt.Soc. Am. B **18** (2001).

³ G. Gallot and D. Grischkowsky, *Electro-optic detection of terahertz radiation*, J. Opt.Soc. Am. B **16** (1999).

Floquet Majorana and Para-Fermions in Driven Rashba Nanowires

Manisha Thakurathi,¹ Daniel Loss,¹ and Jelena Klinovaja¹

¹*Department of Physics, University of Basel, Klingelbergstrasse 82, CH-4056 Basel, Switzerland*

We study a periodically driven nanowire with Rashba-like conduction and valence bands in the presence of a magnetic field. We identify topological regimes in which the non-interacting system hosts zero-energy bound states. We further investigate the effect of strong electron-electron interactions that give rise to parafermion zero energy modes hosted at the nanowire ends. The first setup we consider allows for topological phases by applying only static magnetic fields without the need of superconductivity. The second setup involves both superconductivity and time-dependent magnetic fields and supports topological phases without fine-tuning of the chemical potential. Promising candidate materials are graphene nanoribbons due to their intrinsic particle-hole symmetry.

I. INTRODUCTION

Topological phases in condensed matter systems have been at the center of attention over the past decade. So far most of the studies on topological phases such as topological insulators, Majorana fermions, and parafermions were focused on static systems. However, the dearth of naturally occurring topological materials is stimulating new proposals to engineer systems with topological phases. External driving gives us a powerful tool to turn initially non-topological materials into topological ones¹. This is a most promising approach for both condensed matter and cold atom fields. The existence of exotic edge modes have been demonstrated by direct observation in photonic crystals². The Floquet states have remarkably richer structure than its static counterparts. In this work, we explore one of such phases, namely, Floquet fractional topological insulators which exhibit fractional excitations.

In the first setup, we consider a Rashba nanowire (see Fig. 1) driven by an oscillating electric field [$\mathcal{E}(t)$] with frequency matching the energy difference between the conduction and valence bands. We show that the topological zero energy bound states localized at the nanowire ends can be realized by the mere presence of a uniform static magnetic field without any need of superconductivity. In the second setup, a one-band Rashba nanowire with proximity-induced superconductivity is subjected to a time-dependent magnetic field. This setup has an important advantage over those with time-independent magnetic fields³ in that the chemical potential does not need to be tuned close to the spin-orbit energy. For both setups, we find topological bound states also in the fractional charge regime.

II. FLOQUET RASHBA NANOWIRE IN APPLIED MAGNETIC FIELD

We consider a one-dimensional Rashba nanowire (see Fig. 1) aligned along x -direction characterized by the spin-orbit interaction (SOI) vector α , which points perpendicular to the nanowire axis in the z -direction. The

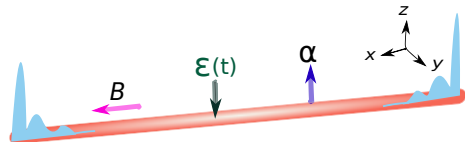
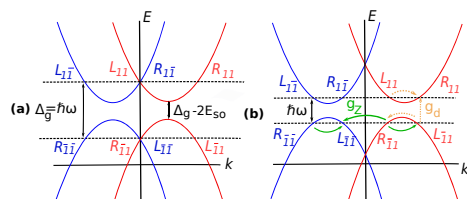


FIG. 1: One-dimensional Rashba nanowire (orange cylinder) with the SOI vector α pointing in the z -direction is aligned along x -direction. The magnetic field \mathbf{B} is chosen in x -direction. A driving electric ac field $\mathcal{E}(t)$ of resonant frequency ω , resulting in the coupling t_F between bands, is applied in transverse z -direction. In the topological regime $\Delta_Z > t_F > 0$, the system hosts zero energy bound states (blue curves) at each wire end.



corresponding Hamiltonian is given by

$$H = \sum_{\eta\sigma} \eta \Psi_{\eta\sigma}^\dagger \left(-\frac{\hbar^2 \partial_x^2}{2m_0} + \alpha \sigma \partial_x + \delta_{1\eta} \Delta_g \right) \Psi_{\eta\sigma} \quad (1)$$

$$+ \Delta_Z \sum_{\eta\sigma\sigma'} \Psi_{\eta\sigma}^\dagger (\sigma_x)_{\sigma\sigma'} \Psi_{\eta\sigma'}$$

where $\Psi_{\eta\sigma}(x)$ annihilates an electron at position x from η band with spin σ . The gap between valence and conduction band is $\Delta_g - 2E_{so}$. Δ_Z is the Zeeman Energy.

III. FLOQUET SPECTRUM

The Floquet term, $H_d = t_F \sum_{\eta\sigma} \Psi_{\eta\sigma}^\dagger \Psi_{\bar{\eta}\sigma}$, with the Floquet coupling amplitude $t_F = e\mathcal{E}d_{cv}/2$, couples conduction and valence bands.

$$\mathcal{H}_F = \begin{pmatrix} E_k + \alpha k & \Delta_Z & t_F & 0 \\ \Delta_Z & E_k - \alpha k & 0 & t_F \\ t_F & 0 & -E_k - \alpha k & \Delta_Z \\ 0 & t_F & \Delta_Z & -E_k + \alpha k \end{pmatrix}$$

$$E_{F\pm}^2 = \left(\frac{\hbar^2 k^2}{2m_0}\right)^2 + (\alpha k)^2 + \Delta_Z^2 + t_F^2 \\ \pm 2\sqrt{\Delta_Z^2 t_F^2 + \left(\frac{\hbar^2 k^2}{2m_0}\right)^2 [(\alpha k)^2 + \Delta_Z^2]}$$

The gap closes for $\Delta_Z = t_F$ at $k = 0$, which indicates toward phase transition. For strong SOI, the linearized Hamiltonian around the Fermi points $k_F = \pm 2k_{so}$ and $k_F = 0$, is given by $\mathcal{H} = \hbar v_F \hat{k} \tau_3 + t_F \eta_1 \tau_1 + \Delta_Z (\tau_1 \sigma_1 + \eta_3 \tau_2 \sigma_2)/2$.

The energy eigenvalues are $E_{1,\pm} = \pm \sqrt{(\hbar v_F k)^2 + t_F^2}$ and $E_{2,\pm}^2 = \sqrt{(\hbar v_F k)^2 + (t_F \pm \Delta_Z)^2}$. For $\Delta_Z > t_F > 0$, system hosts one zero-energy bound state with the localization lengths $\xi_t = \hbar v_F / t_F$ and $\xi_- = \hbar v_F / (\Delta_Z - t_F)$.

IV. FLOQUET PARAFERMIONS

The fractional Floquet modes in interacting nanowire: The chemical potential is moved down to $\mu_{1/3} = E_{so}/9$, such that the Fermi wavevectors are given by $\pm k_{so}(1 \pm 1/3)$. The term coming out from interaction and Zeeman term can be written as $H_Z^{ee} = g_Z [(R_{1\bar{1}}^\dagger L_{11})(R_{1\bar{1}}^\dagger L_{1\bar{1}})(R_{11}^\dagger L_{11}) + (R_{11}^\dagger L_{1\bar{1}})(R_{1\bar{1}}^\dagger L_{11})(R_{1\bar{1}}^\dagger L_{1\bar{1}}) + \mathbf{H.c.}]$. The term which commute with H_Z^{ee} is $H_t^{ee} = g_d [(R_{11}^\dagger L_{1\bar{1}})(R_{1\bar{1}}^\dagger L_{11})(R_{11}^\dagger L_{1\bar{1}}) + (R_{1\bar{1}}^\dagger L_{11})(R_{11}^\dagger L_{1\bar{1}})(R_{1\bar{1}}^\dagger L_{11}) + \mathbf{H.c.}]$. Bosonization leads to

$$H_Z^{ee} = 4g_Z \cos(\theta_1) \cos(3\theta_2), \quad x > 0, \\ H_t^{ee} = 4g_d \cos(\theta_1) \cos(3\phi_2), \quad x < 0.$$

The domain wall at $x = 0$ hosts a zero-energy parafermion state defined by the operator $\alpha_\pm = e^{i4\pi(\hat{n} \pm \hat{1})/3}, \alpha_\pm^3 = 1$.

V. FLOQUET RASHBA NANOWIRE PROXIMITY-COUPLED TO A SUPERCONDUCTOR

We consider one-band Rashba nanowire proximity-coupled to an s -wave superconductor driven periodically by a time-dependent uniform magnetic field $B(t)$ applied perpendicular to the SOI vector.

The pairing term and Floquet term in the Hamiltonian are given by $H_s = \sum_\eta \Delta_{sc} [R_{\eta\bar{1}}^\dagger L_{\eta 1}^\dagger - R_{\eta 1}^\dagger L_{\eta\bar{1}}^\dagger + \mathbf{H.c.}]$ and $H_d = t_F \sum_\eta [R_{\eta\bar{1}}^\dagger L_{\eta\bar{1}} + \mathbf{H.c.}]$.

The linearized Hamiltonian density $\mathcal{H} = \hbar v_F \hat{k} \tau_3 + \Delta_{sc} \tau_1 \sigma_2 \delta_2 + \frac{t_F}{2} \eta_1 \delta_3 (\tau_1 \sigma_1 + \tau_2 \sigma_2)$ with energy eigenvalues $E_{1,\pm} = \pm \sqrt{(\hbar v_F k)^2 + \Delta_{sc}^2}$ and $E_{2,\pm}^2 = \sqrt{(\hbar v_F k)^2 + (t_F \pm \Delta_{sc})^2}$.

For $0 < \Delta_{sc} < t_F$, the system is in the topological phase and hosts two zero-energy Majorana bound states protected by an effective time-reversal symmetry $U_T = \sigma_2 \tau_1 \eta_3$. In the presence of strong electron-electron interactions, we repeat the bosonization procedure and find the fractional topological regime.

VI. CONCLUSIONS

We proposed two simple one-dimensional setups which host zero-energy modes. In the first setup, we consider a single Rashba nanowire with applied uniform static magnetic field driven by a time-dependent electric field. An important feature of this scheme is that no superconductivity is needed, and thus no restrictions on the magnetic field strengths are required. Due to their intrinsic particle-hole symmetry, promising candidates for this setup are carbon nanotubes, graphene, and other two-dimensional crystals.

In the second setup, we consider a model relying on superconductivity with the resonant driving achieved by applying a time-dependent magnetic field. The advantage of this one-band setup is the flexibility in the positioning of the chemical potential. This feature is especially valuable for semiconducting nanowires with large g -factor and with weak proximity-induced superconductivity. The periodic driving brings both systems from the trivial to the topological phase. The systems can be tuned further from standard to fractional topological phase if strong electron-electron interactions are present, which leads in particular to the emergence of parafermions. The potential realization of such systems could be also in cold atoms or optical lattices.

Acknowledgments

We would like to acknowledge Peter Stano for useful discussions. This work was supported by the Swiss National Science Foundation (SNSF) and NCCR QSIT.

¹ N. H. Lindner, G. Refael, and V. Galitski, Nat. Phys. **7**, 490 (2011).

² M. C. Rechtsman, J. M. Zeuner, Y. Plotnik, Y. Lumer, D. Podolsky, F. Dreisow, S. Nolte, M. Segev, and A. Szameit,

Nature **496**, 196 (2013).

³ Y. Oreg, G. Refael, and F. von Oppen, Phys. Rev. Lett. **105**, 177002 (2010).

Imaging of Current Flow at the Nanoscale

Marius Palm,¹ Kevin Chang,¹ Luca Lorenzelli,¹ Jan Rhensius,¹ Alex Eichler,¹ and Christian L. Degen¹

¹Laboratory for Solid State Physics, ETH-Hönggerberg, CH-8093, Zürich, Switzerland

We use the nitrogen-vacancy defect in diamond as a quantum sensor to image the Oersted field resulting from current flow in two-dimensional conductors at ambient conditions. By using a diamond tip hosting a defect at the apex in a scanning probe setup, we obtain spatially resolved magnetic images that can be reconstructed into current density images. We aim to use this technique to investigate current flow in graphene as well as other two-dimensional materials with high spatial resolution.

I. INTRODUCTION

The field of mesoscopic physics has been very active over the last half century due to the interesting phenomena showing up at these length scales. Non-invasive imaging of current flow in these devices is very challenging at the nanometer scale. The negatively charged nitrogen-vacancy (NV) center, a crystal defect in diamond, formed by a substitutional nitrogen next to a vacancy, is a potential sensor that could accomplish this task. The imaging of the current density is done indirectly by measuring the Oersted field outside the conductor and then performing a reconstruction¹. Two-dimensional magnetic field maps are obtained by raster scanning the sample with a scanning probe microscope hosting a NV center at the apex²⁻⁴. This technique has both high spatial resolution and good magnetic sensitivity, while being non-invasive and applicable at a wide range of temperatures. Using this method, current flow has been imaged in carbon nanotubes⁵ and Pt nanowires⁵. Graphene has also been investigated by NV magnetometry⁶, although not in a scanning probe arrangement. Aside from the previously mentioned applications, scanning magnetometry is also actively used to investigate magnetism in thin magnetic films.

A. Optically Detected Magnetic Resonance

We measure the magnetic field parallel to the NV symmetry axis through optically detected magnetic resonance. The electronic level structure of the negatively-charged NV center is shown in FIG. 1c). The ground state is a spin triplet state with a zero field splitting of 2.87 GHz between the $|m_s = 0\rangle$ state and the degenerate $|m_s = \pm 1\rangle$ states. Similarly, the excited state is also a spin triplet state, though with a different zero-field splitting. Radiative spin-conserving transitions can be induced by illumination with a green laser (532 nm) and subsequent relaxation is done via emission of red light. The electronic structure is further complicated by the presence of an additional singlet state, energetically located between the ground and excited state. Moreover, the transition probability from the excited state to the singlet state is highly spin-dependent. The fluorescence of the NV center in the nonzero spin states

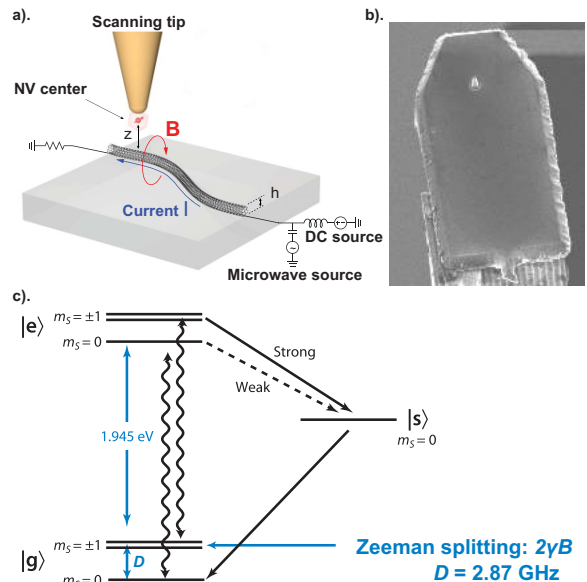


FIG. 1: a). Schematic drawing of the scanning setup used for Oersted field measurement of carbon nanotubes⁵. A nanodiamond containing a single NV center is attached to the apex of a commercial AFM cantilever tip and the illumination of the center is done from below through a transparent substrate. The microwave field required for ODMR is applied through the carbon nanotube itself. Adapted from reference⁵. b). A SEM picture of a new generation of diamond scanning probes with a NV center in the tip of a diamond pillar. c). Diagram of the electronic level structure for a NV center, consisting of spin-triplet ground state $|g\rangle$, excited state $|e\rangle$ and the singlet state $|s\rangle$. Illumination with a green laser results in fluorescence of the NV-center. The unequal transition probabilities from the excited states to the singlet state are indicated by the solid and dashed arrows. An external magnetic field lifts the degeneracy between the $|m_s = \pm 1\rangle$ states. Adapted from reference⁷.

is reduced due to this additional decay channel via the long-lived singlet state. This leads to an optical contrast of roughly 30 % at the electron paramagnetic resonance (EPR) frequency (applying microwaves resonant with the $|m_s = 0\rangle \leftrightarrow |m_s = \pm 1\rangle$ transition). Note that by continuous illumination, the NV center is pumped into the $|m_s = 0\rangle$ state. A magnetic field parallel to the NV quantization axis leads to an energy shift of the $|m_s = \pm 1\rangle$ states through the Zeeman effect, thus lifting the degen-

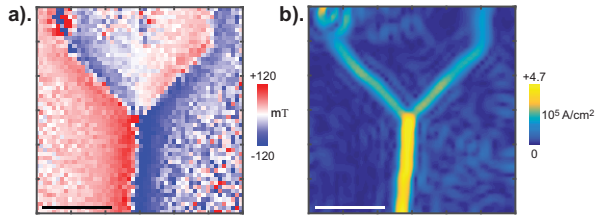


FIG. 2: a). Image of the Oersted field $B_{||}$ of a Y-shaped current-carrying Pt nanowire. b). Current density image reconstructed from the data in a). All scale bars are 1 μ m. Adapted from reference⁵.

eracy. The field component $B_{||}$ can then be obtained by sweeping an auxiliary microwave field, determining the EPR frequency ν and subtracting the zero field splitting D :

$$B_{||} = \frac{2\pi(\nu - D)}{\gamma_e} \quad (1)$$

where $\gamma_e = 2\pi \cdot 28 \text{ GHz T}^{-1}$ is the electron gyromagnetic ratio. A small bias magnetic field is typically applied to separate the $|m_s = \pm 1\rangle$ states.

B. Current Density Reconstruction

Once the Oersted field has been acquired, it is reconstructed into a current density image (FIG. 2). For two-dimensional current densities, this inverse problem to the Biot-Savart law is possible for a single component of the magnetic field taken at a fixed height¹. The reconstruction process is done in Fourier space complemented by spatial filtering techniques.^{1,5}

II. EXPERIMENT AND OUTLOOK

Recently, we started using all-diamond scanning probes⁸ with diamond pillars instead of nanodiamonds, allowing amongst other for higher fluorescence collection⁹. In these probes, the NV-sample standoff distance is set by the implantation depth of the NV center in the diamond ($\approx 10 \text{ nm}$). Controlling the NV-sample standoff distance is important as it limits the achievable spatial resolution of the technique⁷. A SEM image of an all-diamond probe is shown in FIG. 1 b). A further improvement of these probes are the considerably longer spin coherence times¹⁰, allowing us to use pulsed sequences^{7,10} and adaptive sensing protocols¹¹ with higher magnetic field sensitivity than ODMR. For example, by shifting our detection frequency to the MHz regime using pulsed EPR sequences, we project a current sensitivity of less than 10 nA after reconstruction compared to a previous sensitivity of $\sim 1 \mu\text{A}$ ⁵.

Graphene is a great material for our technique as it is a two-dimensional conductor with interesting electron transport properties. With our scanning magnetometer, we want to resolve current density fluctuations with a spatial resolution of less than 10 nm in order to gain a better understanding of the influence of defects and scattering on conductance in graphene.

In the future, we would also like to move to cryogenic temperatures. In addition to an improved instrumental stability, this would also allow us to investigate current flow of many more interesting phenomena in mesoscopic physics.

¹ B. J. Roth, N. G. Sepulveda, and J. P. Wikswo, *Using a magnetometer to image a twodimensional current distribution*, Journal of Applied Physics **65**, 361 (1989).

² C. L. Degen, *Scanning magnetic field microscope with a diamond single-spin sensor*, Applied Physics Letters **92**, 243111 (2008).

³ G. Balasubramanian et al., *Nanoscale imaging magnetometry with diamond spins under ambient conditions*, Nature **445**, 648 (2005).

⁴ B. M. Chernobrod and G. P. Berman, *Spin microscope based on optically detected magnetic resonance*, Journal of Applied Physics **97**, 014903 (2005).

⁵ K. Chang, A. Eichler, J. Rhensius, L. Lorenzelli, and C. L. Degen, *Nanoscale imaging of current density with a single-spin magnetometer*, Nano Letters **17**, 2367 (2017).

⁶ J.-P. Tetienne, N. Dontschuk, D. A. Broadway, A. Stacey, D. A. Simpson, and L. C. L. Hollenberg, *Quantum imaging of current flow in graphene* (2016).

⁷ R. Schirhagl, K. Chang, M. Loretz, and C. L. Degen,

Nitrogen-vacancy centers in diamond: Nanoscale sensors for physics and biology, Annual Review of Physical Chemistry **65**, 83 (2014).

⁸ P. Maletinsky, S. Hong, M. S. Grinolds, B. Hausmann, M. D. Lukin, R. L. Walsworth, M. Loncar, and A. Yacoby, *A robust, scanning quantum system for nanoscale sensing and imaging*, Nature Nanotechnology **7**, 320 (2012).

⁹ T. M. Babinec, B. J. M. Hausmann, M. Khan, Y. Zhang, J. R. Maze, P. R. Hemmer, and M. Loncar, *A diamond nanowire single-photon source*, Nature Nanotechnology **5**, 195 (2010).

¹⁰ L. Rondin, J.-P. Tetienne, T. Hingant, J.-F. Roch, P. Maletinsky, and V. Jacques, *Magnetometry with nitrogen-vacancy defects in diamond*, Reports on Progress in Physics **77**, 056503 (2014).

¹¹ N. M. Nusran, M. U. Momeen, and M. V. G. Dutt, *High-dynamic-range magnetometry with a single electronic spin in diamond*, Nature Nanotechnology **7**, 109 (2012).

Topological states in graphene superconducting hybrid devices

David Indolese,¹ Raphaëlle Delagrangé,¹ Peter Makk,¹ Kenji Watanabe,² Takashi Taniguchi,² and Christian Schönenberger¹

¹*Department of Physics, University of Basel, CH-4056, Basel, Switzerland*

²*National Institute for Materials Science, Namiki 1-1, Tsukuba, Ibaraki 305-0044, Japan*

Topological excitations such as Majorana- and Parafermions are receiving large attention in today's theoretical and experimental studies due to their non-abelian exchange statistics. This property makes them a promising candidate for quantum computing. One possible way to engineer these excitations is to use quantum spin Hall (QSH) states in contact with superconductors. In our approach we will use spin polarized Landau levels (LL) of graphene multilayer systems.

I. INTRODUCTION

Graphene, a single layer of graphite was discovered in 2004, and not much later it was demonstrated by supercurrent measurements that it can be easily coupled to superconductors, contrary to other 2DEGs¹. Until very recently, the investigation of proximity effect has been limited to very low magnetic field. The progress in making very clean samples, as well as the development of high critical field superconducting contacts make it now possible to observe the coexistence of superconducting correlations and quantum hall edge states². In the QH regime the supercurrent is mediated by the edge states and mixed electron-hole state along the superconducting contact. Due to the chiral nature of these states the transport of the charge carriers, i.e. electron and hole, has to take place at the opposite edges of the graphene sheet. The observation of supercurrent in the QH regime opens the possibility to engineer topological excitations in such a system.

Our approach to form topological excitations is based on a stack of two graphene sheets, which can be tuned separately to different QH states using top and bottom gates^{3,4}. If one graphene is in the LL $\nu = +1$ and the other in $\nu = -1$, the edge states are spin polarized with opposite spins and carry the electrons in opposite directions. These form an artificial helical state, which may be assimilated to a QSH system. By inducing supercurrent in the helical states of the QSH system, a gap could open, giving rise to topological superconductivity, and thus to zero energy fractional excitations. This topological superconductivity would be characterized by a 4π -periodic phase-dependence of the Andreev Bound States, that we aim at detecting through Josephson effect.

II. ENGINEERING OF TOPOLOGICAL EXCITATIONS

The measurement of the current-phase relation is quite challenging and several cutting edge building blocks have to be combined: high mobility graphene, broken symmetry Landau levels, transparent superconducting contacts, complex device architectures for gating and measurement of the current-phase relation. Since the Landau levels in

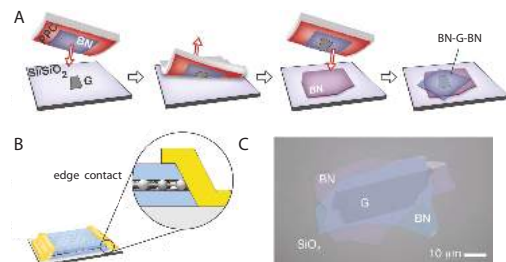


FIG. 1: A) Schematic drawing of the encapsulation process⁵. From left to right: (1) Bring the PPC with exfoliated hBN into contact with graphene (2) Peel it of the substrate (3) place the bilayer stack on the bottom hBN (4) Dissolve the PPC. B) A sketch of a metallic side contact (yellow) is drawn. C) An optical picture of a hBN-graphene-hBN heterostructure

graphene are 4-fold degenerate (spin and valley), the degeneracies of the LL must be broken to form the $\nu = \pm 1$ state. In very clean and high mobility samples this degeneracy is lifted due to electron-electron interactions resulting in conductance steps of e^2/h observed in the QH regime. Different experiment showed that this can be realized by encapsulating the graphene between hexagonal boron nitride (hBN) flakes⁵. To tune the Fermi level of the upper and the lower sheet separately one has to fabricate top and bottom gates, which are tuning the entire graphene homogeneously. For the bottom graphene this can be realized by a global back gate, but the implementation of a global top gate is a challenging task. To observe a supercurrent in graphene transparent superconducting contacts are needed. Finally, a method has to be developed to measure the current-phase relation in the quantum Hall regime, since most of the current methods fail in high magnetic field.

III. SAMPLE FABRICATION

To obtain high mobility graphene devices with transparent superconducting contacts, we encapsulate the graphene between two hBN layers and connect it with MoRe side-contacts out of molybdenum-rhenium. The encapsulation is done by a dry transfer technique (Fig.

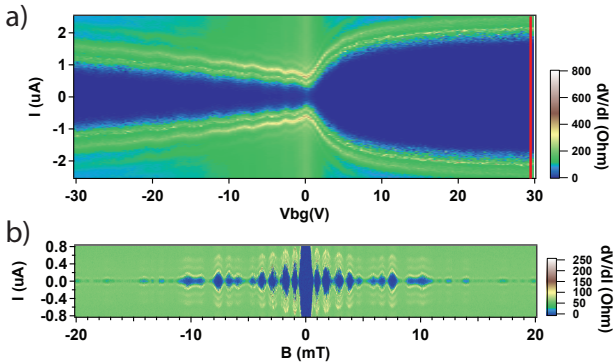


FIG. 2: a) The gate dependence of the critical current was measured at zero magnetic field. One can see oscillations of I_c for negative doping of the graphene, which are due to Fabry-Pérot. b) The differential resistance of the graphene Josephson junction was measured as a function of an applied external field and current at a high back gate voltage (red line on panel).

1), where the graphene flake is picked-up with an hBN due to the strong van der Waals forces between them. Afterwards this bilayer is placed down on a second hBN flake, which was exfoliated on a silicon wafer with a thermally grown oxide layer. To contact the graphene an etching mask is fabricated by e-beam lithography. The hBN-graphene-hBN stack is etched and contacted by co-sputtered MoRe using the same lithography mask.

IV. TOWARDS SUPERCURRENT IN THE QH REGIME

To characterize the transparency of the superconducting contacts and the transport properties of the graphene, we fabricated graphene Josephson junctions. One indication of a clean graphene Josephson junction is the observation of ballistic transport. Fig. 2a) shows the differential resistance as a function of bias current and gate voltage. It can be seen that the supercurrent is gate voltage tunable. Moreover, at negative gate voltages an oscillation of the switching current as a function of gate voltage appears. This results from Fabry-Pérot oscillations

of the critical current I_c and prove the ballistic nature of the supercurrent. The electrons can be reflected from the contacts (due to local doping and formation of pn-junctions in the vicinity of the contacts) and interfere leading to oscillations in the resistance and in the supercurrent. Such oscillations were recently measured in other experiments^{6,7}. We have also found that we can induce sizeable supercurrent in junctions over a distance of 800 nm.

In a planar junction where the supercurrent is homogeneous, we expect the following modulation of the critical current (Fraunhofer pattern) as function of an external magnetic field perpendicular to the junction:

$$I_c(B) = I_c(B = 0) \frac{\sin(\pi\phi/\phi_0)}{\pi\phi/\phi_0}, \quad (1)$$

where $I_c(B = 0)$ is the critical current at zero field, ϕ is the magnetic flux through the junction and ϕ_0 the flux quantum and equals $h/2e$. Fig.2b) shows the Fraunhofer-pattern measurements at high densities (see red line in Fig.2a)). Contrary to the $1/B$ dependence of Equation 1, the supercurrent remains sizeable at higher magnetic fields, and even increases again in some higher B-field regions. These features have been attributed to electron-hole bound states in the graphene, similarly to closed trajectories in classical billiards⁷.

V. OUTLOOK

In the next steps we plan to measure supercurrent in the quantum Hall regime and fabricate graphene bilayer based QSH systems. In further steps we will fabricate a system of a hBN-G-hBN-G-hBN stack with bottom and top gates where topological excitations are expected to appear.

Acknowledgments

We acknowledge SNI, SNF and NCCR QSIT for the financial support.

¹ H. B. Heersche, P. Jarillo-herrero, J. B. Oostinga, L. M. K. Vandersypen, and A. F. Morpurgo, *Nature* **446**, 56 (2007).
² F. Amet, J. Wang, K. Watanabe, T. Taniguchi, R. S. Deacon, M. Yamamoto, Y. Bomze, S. Tarucha, and G. Finkelstein, *Science* **352**, 966 (2016).
³ F. Finocchiaro, F. Guinea, and P. San-Jose, *2D Materials* **2**, 025027 (2017).
⁴ J. D. Sanchez-Yamagishi, J. Y. Luo, A. F. Young, B. M. Hunt, K. Watanabe, T. Taniguchi, R. C. Ashoori, and P. Jarillo-herrero, *Nat. Nanotechnology* **12**, 118 (2016).
⁵ L. Wang, I. Meric, P. Y. Huang, Q. Gao, Y. Gao, H. Tran,

T. Taniguchi, K. Watanabe, L. M. Campos, D. A. Muller, et al., *Science* **342**, 614 (2013).

⁶ V. E. Calado, S. Goswami, G. Nanda, M. Diez, A. R. Akhmerov, K. Watanabe, T. Taniguchi, T. M. Klapwijk, and L. M. K. Vandersypen, *Nat. Nanotechnology* **10**, 761 (2015).

⁷ M. B. Shalom, M. J. Zhu, V. I. Fal, A. Mishchenko, A. V. Kretinin, K. S. Novoselov, C. R. Woods, K. Watanabe, T. Taniguchi, A. K. Geim, et al., *Nat. Physics* **12**, 318 (2016).

Spatial Imaging of Electronic States in Cavities using Scanning Gate Microscopy

Carolin Gold,¹ Richard Steinacher,¹ Andrea Hofmann,¹ Tobias Krähenmann,¹ Christian Reichl,¹ Christina Pörtl,² Rodolfo A. Jalabert,² Dietmar Weinmann,² Werner Wegscheider,¹ Klaus Ensslin,¹ and Thomas Ihn¹

¹Laboratory of Solid State Physics, ETH-Hönggerberg, CH-8093, Zürich, Switzerland

²Institut de Physique et Chimie des Matériaux de Strasbourg,
Université de Strasbourg, F-67034, Strasbourg, France

In the quest to image local electronic properties of an open resonator structure, we perform scanning gate measurements at different tip potentials. Weakly invasive tip-potentials well below the Fermi-energy reveal features reminiscent of the local density of states in the resonator. These features are reproduced by numerical quantum mechanical simulations of the system. Additional finite-bias measurements at weakly invasive tip potentials exhibit a minimum-maximum-transition and vice versa in the differential conductance modulation of the cavity.

I. SCANNING GATE MICROSCOPY

Scanning Gate Microscopy (SGM) is a powerful tool to study electronic transport properties of high mobility two-dimensional electron gases at cryogenic temperatures. By scanning the biased metallic tip of an atomic force microscope over a nanostructure, the potential landscape of the device is perturbed locally (cf Fig.1a). For many years, SGM was anticipated to transfer the huge success of scanning probe experiments to the investigation of electronic systems such as two-dimensional electron gases (2DEGs). However, only few SGM-experiments published address the imaging-process of proper unperturbed local properties. Within this context, our experiments aim at mapping the local density of states (LDOS) and the effect of increased electron-electron scattering in an open resonator structure.

II. EXPERIMENTAL DETAILS

A scanning electron micrograph of the sample structure is depicted in Fig. 1b. The open resonator structure is defined by a Quantum Point Contact (QPC) and a cavity gate (both light grey in Fig. 1b) deposited on a GaAs-AlGaAs-heterostructure. SGM measurements are performed in a He³-cryostat at 270mK by raster-scanning

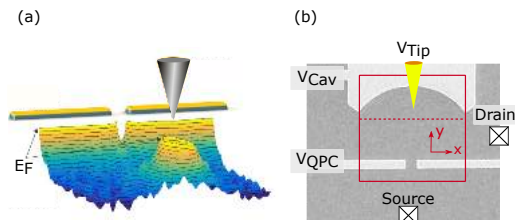


FIG. 1: (a) Tip-induced perturbation of the potential landscape of a 2DEG in close vicinity to a QPC. E_F denotes the Fermi-energy of the system. (b) Scanning electron micrograph of the sample structure depicting the QPC and cavity Schottky gates (light grey) deposited on the GaAs-surface (dark grey). The scan area is indicated by a red frame. Measurements in Fig.3 are obtained along the dashed line.

the tip over the area framed in red in Fig.1b and measuring the conductance of the sample as a function of tip position. In doing so the tip stays at a constant height of 65nm above the GaAs-surface.

III. BRANCHES AND LDOS¹

The impact of the cavity gate as well as differently invasive tip-potentials on the transport properties of the nanostructure are studied in two scan series at different tip and varying cavity gate voltages. While the QPC is tuned to transmit three modes the tip potential is chosen to be either strongly invasive at $V_{\text{tip}} = -6\text{V}$ (upper row in Fig. 2) or weakly invasive at $V_{\text{tip}} = -1\text{V}$ (lower row in Fig. 2). The cavity gate is varied in three distinctly different regimes at both tip-potentials: at first it is unbiased (Fig. 2a,d), then biased but not depleting the 2DEG yet (Fig. 2b,e), before it depletes the 2DEG underneath it completely. For enhanced visibility of distinct features all measurements in Fig. 2 depict the derivative dG/dx in the x-direction of the scan. As reported by Topinka et al.², strongly invasive tip potentials can backscatter electrons previously focused to narrow channels by a background potential of the 2DEG. As long as the cavity gate remains unbiased, the tip induces the only scattering potential in the structure and branched electron flow² is observed in Fig. 2a in the region uncovered by the cavity gate. Once the cavity gate is biased, the emerging potential underneath the gate confines the transport electrons to the area between QPC and cavity gate. The thus increased local density of states (LDOS) in this area alters the backscattering pattern of electrons from the tip potential, giving rise to more complex conductance modulations in the cavity. As soon as the 2DEG below the cavity gate is fully depleted, these modulations oscillate in the range of $\lambda_F/2$ (cf Fig. 2c). SGM-measurements for the weakly invasive tip ($V_{\text{tip}} = -1\text{V}$) however look strikingly different. Almost no influence of the tip on the sample conductance is observed for the unbiased cavity gate. As the weakly invasive tip potential is far below the Fermi-energy of the system, no electrons can backscatter classically from the tip-induced potential. Biasing the

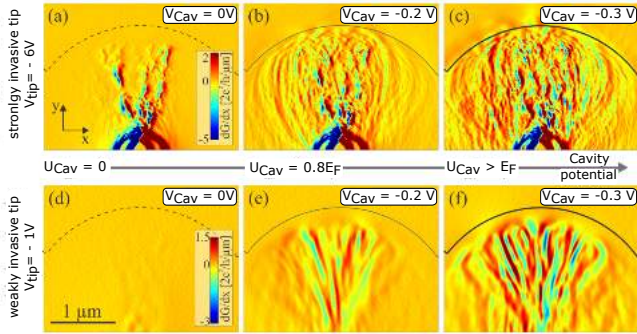


FIG. 2: Scan series at different cavity gate voltages V_{cav} for a weakly invasive ($V_{\text{tip}} = -1\text{V}$, bottom row) and strongly invasive ($V_{\text{tip}} = -6\text{V}$, top row) tip potential. The cavity gate is first unbiased ($V_{\text{cav}} = 0\text{mV}$) then biased but non-depleting ($V_{\text{cav}} = -0.2\text{mV}$) before it completely depletes the 2DEG underneath at $V_{\text{cav}} = -0.3\text{mV}$.

cavity gate in the non-2DEG-depleting regime induces an additional potential barrier which gives rise to distinct, smooth features emanating the QPC in a radial pattern (cf Fig. 2e). Once the 2DEG beneath the cavity gate is fully depleted, more defined features with higher contrast are observed (cf Fig. 2f). Alike the measurements at strongly invasive tip potentials, the cavity gate induced potential barrier in the 2DEG concentrates the LDOS of the system in the resonator. Theoretical simulations of the performed SGM measurements show an astounding qualitative congruence of the SGM data obtained for weakly invasive tip potentials and the LDOS of the system³.

IV. MINIMUM-MAXIMUM-TRANSITION IN THE DIFFERENTIAL CONDUCTANCE

Electron-electron(e-e)-scattering is the predominant inelastic scattering process to cause dephasing in GaAs-2DEGs. When applying a finite source-drain voltage to measurements of branched electron flow, Jura et al.⁴ observe an increase in the differential conductance when the SGM-tip backscatters electrons. They explain this striking observation by an increase of e-e-scattering close to the constriction. Scanning the weakly invasive tip along a line crossing the cavity features slightly below the boarder of the cavity gate for different bias volt-

ages, we measure an effect resembling the observation of Jura and co-workers. Applying a dc source-drain voltage in the range of 0mV to $\pm 4\text{mV}$ on top of the small ac voltage common in SGM-measurements (here $V_{\text{SD,ac}} = 100\mu\text{V}_{\text{RMS}}$), a clear transition from minima to maxima and vice versa is observed in the differential conductance in Fig. 3b at same tip-positions but different bias voltage. This transition is more obvious in cuts at selected bias voltages (Fig. 3a) or in the derivative of the differential conductance (Fig. 3c).

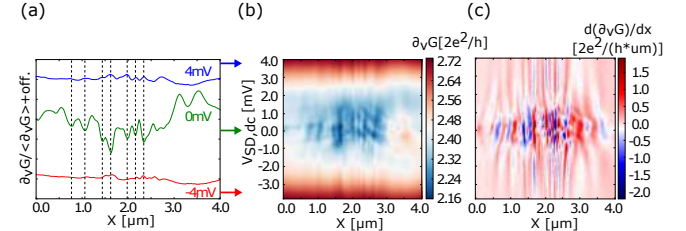


FIG. 3: Different representation of a measurement of the tip position versus finite bias along the dashed line in Fig. 1. (a) single linescans for selected bias voltages of $\pm 4\text{mV}$ and 0mV respectively. (b) Finite bias measurement depicting the differential conductance as a function of bias voltage and the tip positions. (c) derivative dG/dx of the data shown in (b) with respect to the x -direction of the scan.

V. OUTLOOK

The underlying process causing the minimum-maximum transition in the differential conductance for increased bias voltages still remains to be fully understood. A step further are measurements on cavity-quantum dot (QD)-systems in which the QPC is replaced by a QD. As the energy-levels of a QD are much more precisely known than the modes of a QPC, the injection energy of the electrons into the cavity can be controlled in these systems. Granting insights into interesting physical effects such as Kondo physics and maybe even coupling of QDs via whispering gallery modes, these systems are promising to be studied with SGM. In the longer term, we are collaborating with the PoggioLab at University of Basel to combine our knowledge of SGM on 2DEGs with their SQUIDS-on-tips. This could not only enable a new imaging technique to map transport in 2DEGs, but also yield insight into unsolved puzzles such as the exact location of current flow in the Quantum Hall Regime.

¹ R. Steinacher, *Scanning gate imaging in confined geometries* (2017).

² M. A. Topinka, B. J. LeRoy, R. M. Westervelt, S. E. J. Shaw, R. Fleischmann, E. J. Heller, K. D. Maranowski, and A. C. Gossard, *Coherent branched flow in a two-dimensional electron gas*, *Nature* **410**, 183 (2001), ISSN 0028-0836.

³ R. Steinacher, T. Krähenmann, A. Hofmann, C. Reichl,

C. Pörtl, W. Wegscheider, R. Jalabert, D. Weinmann, K. Ensslin, and T. Ihn, *In preparation* (2017).

⁴ M. P. Jura, M. Grobis, M. A. Topinka, L. N. Pfeiffer, K. W. West, and D. Goldhaber-Gordon, *Spatially probed electron-electron scattering in a two-dimensional electron gas*, *Physical Review B* **82**, 155328 (2010).

Towards Majorana Fermions in Graphene Nanoribbons

Timothy Camenzind,¹ Mirko Rehmann,¹ Yemliha Bilal Kalyoncu,¹ and Dominik Zumbühl¹

¹*Department of Physics, University of Basel, Klingelbergstrasse 82, CH-4056 Basel, Switzerland*

Recent theoretical studies have predicted the existence of helical modes in armchair graphene nanoribbons in the presence of rotating magnetic fields. When placed next to a superconductor, the nanoribbon can be tuned into a topological phase which contains Majorana fermions. In order to accomplish this topological phase, the fabrication and characterization of an array of nanomagnets needs to be investigated. The array can be alternated between two distinguishable states of magnetization and can thus produce two different magnetic fields which change the electronic spectrum of the graphene nanoribbons.

I. INTRODUCTION

Computational power has increased tremendously during the past few decades and the demand continues to grow alongside. While new lithographic techniques have allowed companies to build increasingly smaller structures and to increase the density of common transistors on a single chip, the Si based technology will eventually stretched to its limits. In order to overcome these limitations in computational power, researchers all around the world are working on the next logical step: the quantum computer.

In 1998, Daniel Loss and David DiVincenzo proposed use the spin of an electron confined in a quantum dot as a scalable qubit, the information unit of the quantum computer¹. Alternatively, one could use Majorana fermions as qubits. These exotic particles are their own anti-particles and have the advantage of creating a fault-tolerant quantum system². However, Majorana fermions are harder to realize than quantum dots and usual Majorana fermions have insufficient Hilbert space to provide topological protection for all universal gates³.

Jelena Klinovaja and Daniel Loss have shown that graphene nanoribbons (GNRs) can host so-called Majorana bound states at the end of the GNRs when placed in close proximity to an s-wave superconductor and with induced spin-orbit interaction (SOI)⁴. In order to induce SOI into a GNR, a rotating magnetic field generated by an array of anti-parallel magnetized nanomagnets has to be fabricated in close proximity to an armchair graphene nanoribbon (acGNR). The rotating magnetic field with a periodicity of $\lambda_n = 2\pi/k_n$ leads to a modification of the band structure in which the normally spin-degenerate bands are shifted in momentum space. The resulting spin-orbit energy Δ_{SO}^n lies perpendicularly to the rotating magnetic field and has the following form

$$\Delta_{SO}^n = \frac{\hbar\nu_F k_n}{2} \quad (1)$$

where \hbar is the reduced Planck constant and ν_F the Fermi velocity of graphene. The spin-orbit energy can be converted into a separation of the two spin-degenerate parabolas in k -space with the following formula

$$k_{SP} = \frac{\Delta_{SO}^n}{\hbar\nu_F} = \frac{k_n}{2} \quad (2)$$

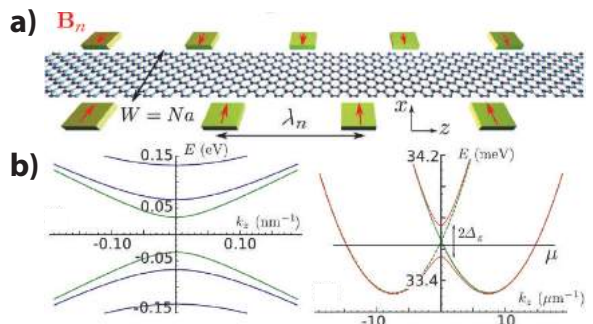


FIG. 1: a) An acGNR aligned along the z-axis with nanomagnets (green slabs) with a periodicity of λ_n creating a spatially rotating magnetic field. b) Low energy spectra without (left) and with (right) induced spin-orbit interaction. Figures taken from Ref. 4.

It is remarkable that the shift in k -space is inverse proportional to the periodicity of the rotating magnetic field which can be tuned by the spacing between the nanomagnets.

When applying an additional magnetic field perpendicularly to the induced SOI, a gap $2\Delta_g$ opens at $k = 0$. The resulting band structure can be seen in figure 1. By shifting the chemical potential μ inside the gap, helical states emerge where the current is spin polarized. By placing a superconductor next to the acGNR in the helical state, the system can be tuned into a topological phase that can host Majorana fermions.

II. FABRICATION

In order to tune an acGNR into the helical state, an array of nanomagnets has to be fabricated in which the magnetization direction of each subsequent nanomagnet is rotated by 180° . As the distance between the nanomagnets determines the periodicity of the thus generated magnetic field and the induced band-shift in k -space, the nanomagnets have to be as periodic as possible. The first idea was to use different widths of rectangular-shaped nanomagnets because they react differently to an externally applied magnetic field and can so be magnetized in the desired configuration. However, this plan was replaced by the idea of using rhombic-shaped nanomagnets

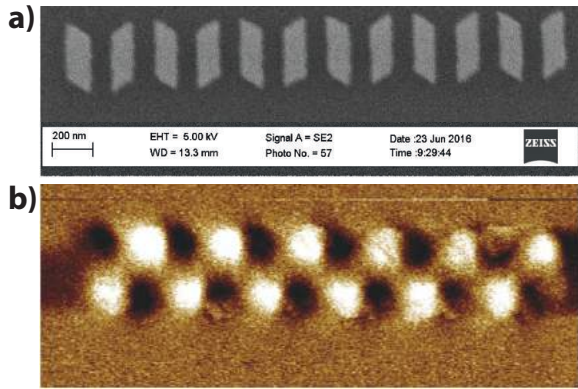


FIG. 2: a) SEM image of the rhombic-shaped nanomagnets with a width of 100 nm and a spacing of 100 nm. b) Magnetic force microscope image of the alternatively magnetized array of nanomagnets.

since they can easily be tuned into both a parallel as well as an anti-parallel configuration⁵. This can be achieved by applying a magnetic field in either the geometrically short or long direction and can be done inside a dilution refrigerator with a vector magnet without needing to warm up the device. This allows to control the induction of SOI in an acGNR in situ.

The fabrication was carried out using standard e-beam lithography and yielded rhombic-shaped nanomagnets of 300 nm length, 50 to 100 nm width, 30 nm height and a spacing of 50 to 100 nm between the nanomagnets. The material used was permalloy with a sticking layer of titanium, because permalloy results in single domain nanomagnets. Alternatively, one could use copper as it generates a stronger magnetic field, however, copper is not always single domain on this length scale.

III. RESULTS AND DISCUSSION

Magnetic force microscopy was used in order to characterize the fabricated array of nanomagnets. The goal was to see if and how the magnetization reacts to both in- and out-of-plane magnetic fields. Therefore, the array of nanomagnets was magnetized in an electromagnet

and investigated in a magnetic force microscope (MFM) using the common lift-off technique. This allows to see the magnetic field gradient without topographic effects disturbing the measurement.

By applying a magnetic field along the geometrically long axes the magnetic moments align in parallel and thus all nanomagnets are magnetized in the same direction. If the magnetic field is applied along the geometrically short axis of the nanomagnets, the magnetic moments first align in parallel to the applied magnetic field, but do relax into two distinct and shape-dependent ground states. This happens due to small misalignments in the top and bottom parts of the rhombic-shaped nanomagnets. The small deviation results then in an anti-parallel magnetization of the nanomagnet array.

In order to open a gap at $k = 0$, an additional magnetic field has to be applied perpendicularly to the nanomagnets. Therefore, an external magnetic field was applied and an upper limit of $B_z = 150mT$ was determined. The upper limit defines the strength under which the nanomagnets do not change their configuration.

IV. CONCLUSION

To sum up, an array of rhombic-shaped nanomagnets has been fabricated, which is capable of creating a rotating magnetic field with the goal to introduce spin-orbit interaction into an acGNR. This is done by shifting the spin-degenerate bands in an acGNR in k -space and by using an additional magnetic field creating a gap at $k = 0$. With the resulting helical state and a superconductor placed in close proximity to the acGNR, the system is predicted to be able to be tuned into a topological phase which can host Majorana fermions.

Acknowledgments

We would like to thank J. Klinovaja and D. Loss for helpful discussions. This work was supported by the Swiss Nanoscience Institute (SNI), NCCR QSIT and Swiss NSF.

¹ D. Loss and D. P. DiVincenzo, *Quantum computation with quantum dots*, Physical Review A **57**, 120 (1998).

² A. Y. Kitaev, *Fault-tolerant quantum computation by anyons*, Annals of Physics **303**, 2 (2003).

³ J. K. Pachos, *Introduction to topological quantum computation* (Cambridge University Press, 2012).

⁴ J. Klinovaja and D. Loss, *Giant spin-orbit interaction due to*

rotating magnetic fields in graphene nanoribbons, Physical Review X **3**, 011008 (2013).

⁵ A. Haldar and A. O. Adeyeye, *Deterministic control of magnetization dynamics in reconfigurable nanomagnetic networks for logic applications*, ACS nano **10**, 1690 (2016).

Hole Spin Qubits in Ge/Si nanowires

Florian N. M. Froning,¹ Ang Li,² Erik P. A. M. Bakkers,² Dominik M. Zumbühl,¹ and Floris R. Braakman¹

¹*Department of Physics, University of Basel, CH-4056, Basel, Switzerland*

²*Department of Applied Physics, Eindhoven University of Technology, Postbox 513, 5600 MB Eindhoven, The Netherlands*

The experimental realization of a quantum algorithm on a quantum computer requires the implementation of long-range qubit-qubit interactions to execute quantum gates. This project aims at the coupling of hole spin qubits hosted in quantum dots in Ge/Si core/shell nanowires. This material system is well-suited because it was predicted to have a strong and tunable spin-orbit interaction, useful for fast qubit manipulation, while maintaining quite long spin relaxation and coherence time, allowed by a potentially nuclear spin free host material and reduced hyperfine coupling. The coupling can be realized by either floating metallic gates or via the intracavity field of a superconducting resonator.

I. INTRODUCTION

The establishment of long-range interactions between qubits is of fundamental interest for the experimental implementation of quantum gates. In the past years, most research was focused on the improvement of quantum bits, so this project aims at the coupling of qubits to take the next step toward the implementation of the surface code. The system of choice are quantum dots electrostatically defined in Ge/Si core/shell nanowires¹, which are well-suited due to the strong and tunable spin-orbit interaction as well as the long spin relaxation times. These nanowires form a radial heterostructure with a quantum well such that holes accumulate in the core of the nanowire², away from the nanowire surface and hence less susceptible to surface effects. By introducing tunnel barriers with electrostatic nanogates, quantum dots can be defined with a low number of confined holes³⁻⁵.

In comparison to electrons in quantum dots, the contact hyperfine interaction with nuclear spins is strongly reduced for holes due to their p-wave character. Together with a potentially nuclear spin free host material, by isotopically purifying both Germanium and Silicon, the spin coherence time of spin qubits can be strongly enhanced^{6,7}. Another major advantage of Ge/Si nanowires is the predicted strong spin-orbit interaction⁸. The tight radial confinement given by the nanowire dimensions creates a mixing of heavy and light-hole states in the valence band, which yields a strong spin-orbit interaction of Rashba type. Moreover, the spin-orbit coupling is electric field tunable⁹⁻¹¹ and depends strongly on the relative orientation of electric and magnetic field, which results in a large g-factor anisotropy¹².

To generate a coupling between qubits, two different methods are to be explored: first, floating metallic gates could couple qubit pairs capacitively¹³. Second, long-range interactions can be mediated by the electric field of a superconducting microwave resonator¹⁴. Here, the key mechanism is the exploitation of the spin-orbit interaction to generate a coupling between the spins and the cavity field via the dipole coupling of the charge.

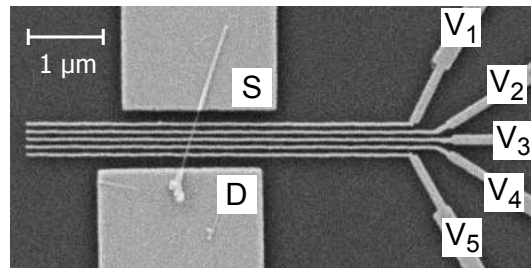


FIG. 1: Scanning electron microscope image of a typical Ge/Si nanowire sample. A single nanowire is placed deterministically with a micromanipulator on top of the predefined gates (V_{1-5}). Source (S) and drain (D) contacts are patterned with electron beam lithography and metallized with Ti/Pd.

II. SAMPLE FABRICATION

The general device scheme as shown in Fig. 1, contains a Ge/Si nanowire placed deterministically on top of nanogates. Electron beam lithography was used to fabricate five gates with a nominal pitch of 100 nm, on top of a p^{++} -doped silicon substrate covered with 290 nm SiO_2 . Subsequently, the gates are covered by 10 nm Al_2O_3 grown by atomic layer deposition. A single Ge/Si nanowire with a diameter between 30 nm and 60 nm is placed deterministically on the gates with a micromanipulator. Ohmic contacts are patterned by electron beam lithography and metallized with Ti/Pd after an HF etch to remove the native oxide on the nanowire.

III. STATE OF THE ART

So far, most of our experimental efforts were focused on the fabrication of Ge/Si nanowire devices as described in Sec. II. As expected, both the intrinsic quality of the nanowire and the ohmic contact transparency play a crucial role for the ability to controllably define quantum dots. Impurities can create natural barriers and define accidental quantum dots, which are especially often observed close to the ohmic contacts. The contact

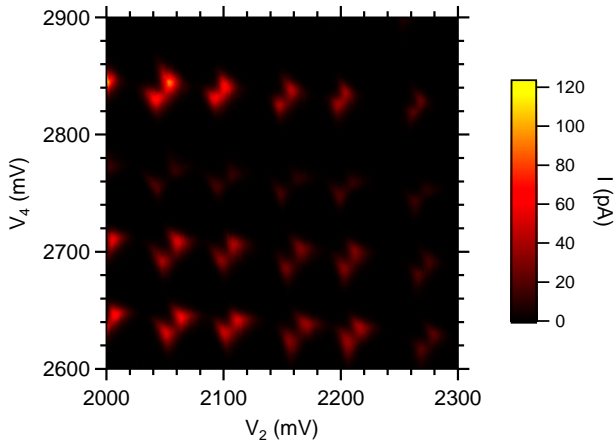


FIG. 2: Several bias triangles of a double quantum dot formed in the Ge/Si nanowire with $V_{SD} = 2$ mV. The voltages V_2 and V_4 are applied to the plunger gates of the left and the right dot, respectively.

transparency is strongly dependent on the removal of the native oxide which grows on the Si surface of the nanowire. Up to now, several devices show good ability to controllably define single and double quantum dots in the nanowire with multiple holes confined. We conduct transport experiments at 4.2 K and measure Coulomb diamonds. Furthermore, we formed double quantum dots with a great stability over a wide range of gate voltages. A typical excerpt of bias triangles is shown in Fig. 2. Here, the left and middle tunnel barriers are formed by V_1 and V_3 , while the right tunnel barrier is formed by the drain contact. Gates with voltages V_2 and V_3 in between serve as plunger gates for the left (V_2) and right (V_3) dot.

IV. OUTLOOK

First experiments will be focused on characterizing the spin-orbit interaction. Previous studies on the anisotropy¹² and the electric field tunability¹⁰ of the spin-orbit coupling strength already showed good agreement with theory. However, especially the tunability with electric fields remains unexplored but yet of great interest, since this will be the key mechanism for long-range interactions as well as qubit gating. Future efforts will include the creation of a hybrid system with a qubit embedded in a superconducting microwave cavity. This will open the door to many interesting experiments on spin resonance and cavity physics.

V. SUMMARY

In summary, hole quantum dots defined in a Ge/Si core-shell nanowire are a promising platform for the implementation of long-range qubit interactions because of their outstanding intrinsic material properties. First of all, the spin coherence times can be very long due to the reduced contact hyperfine interaction of holes inside a potentially nuclear spin-free host material. Second, the electric field tunable spin-orbit interaction could form the basis for fast qubit gating, however, only little experimental research has been done on its nature until now. In a first step, the formation of double quantum dots has been shown. Future experiments include spin resonance experiments and qubit coupling via a superconducting microwave cavity or floating metallic gates.

-
- ¹ C. Kloeffer and D. Loss, *Ann. Rev. Condens. Matter Phys.* **4**, 51 (2013).
² W. Lu, J. Xiang, B. P. Timko, Y. Wu, and C. M. Lieber, *PNAS* **102**, 10046 (2005).
³ Y. Hu, H. O. H. Churchill, D. J. Reilly, J. Xiang, C. M. Lieber, and C. M. Marcus, *Nature nanotech.* **2**, 622 (2007).
⁴ S. Roddaro, A. Fuhrer, P. Brusheim, C. Fasth, H. Q. Xu, L. Samuelson, J. Xiang, and C. M. Lieber, *Phys. Rev. Lett.* **101**, 186802 (2008).
⁵ M. Brauns, J. Ridderbos, A. Li, E. P. A. M. Bakkers, and F. A. Zwanenburg, *Appl. Phys. Lett.* **109**, 143113 (2016).
⁶ Y. Hu, F. Kuemmeth, C. M. Lieber, and C. M. Marcus, *Nature Nanotech.* **7**, 47 (2012).
⁷ A. P. Higginbotham, T. W. Larsen, J. Yao, H. Yan, C. M. Lieber, C. M. Marcus, and F. Kuemmeth, *Nano Lett.* **14**, 3582 (2014).
⁸ C. Kloeffer, M. Trif, and D. Loss, *Phys. Rev. B* **84**, 195314

- (2011).
⁹ F. Maier, C. Kloeffer, and D. Loss, *Phys. Rev. B* **87**, 161305 (2013).
¹⁰ X. J. Hao, T. Tu, G. Cao, C. Zhou, H. O. Li, G. C. Guo, W. Y. Fung, Z. Ji, G. P. Guo, and W. Lu, *Nano Lett.* **10**, 2956 (2010).
¹¹ A. P. Higginbotham, F. Kuemmeth, T. W. Larsen, M. Fitzpatrick, J. Yao, H. Yan, C. M. Lieber, and C. M. Marcus, *Phys. Rev. Lett.* **112**, 216806 (2014).
¹² M. Brauns, J. Ridderbos, A. Li, E. P. A. M. Bakkers, and F. A. Zwanenburg, *Phys. Rev. B* **93**, 121408 (2016).
¹³ L. Trifunovic, O. Dial, M. Trif, J. R. Wootton, R. Abebe, A. Yacoby, and D. Loss, *Phys. Rev. X* **2**, 011006 (2012).
¹⁴ C. Kloeffer, M. Trif, P. Stano, and D. Loss, *Phys. Rev. B* **88**, 241405 (2013).

Graphene cyclotron polaritons and the Dicke Model

Shima Rajabali,¹ Janine Keller,¹ Giacomo Scalari,¹ and Jérôme Faist¹

¹*Institute of Quantum Electronics, ETH-Hönggerberg, CH-8093, Zürich, Switzerland*

Investigation of the coupling between complementary split-ring resonators as the metamaterial surface and graphene cyclotron transition is the aim of our ongoing project. Terahertz time domain spectroscopy, as well as electrical characterization, are utilized for this purpose. A high mobility and large area graphene sample on a doping level engineered substrate together with an adapted resonator design are needed to be able to observe this energy exchange in the ultrastrong coupling regime and the superradiant phase transition predicted by Dicke.

I. INTRODUCTION

Manipulation of light and matter interaction is a critical topic for investigating cavity quantum electrodynamics(QED) and its application¹. The rate of energy exchange between the cavity photon and the matter excitation is quantified by vacuum Rabi splitting (Ω) which can determine the coupling strength. The strong coupling regime is defined in case Ω surpasses the loss rates of the system. However, if this quantity becomes comparable with the frequency of the unperturbed system, an ultrastrong coupling regime can be obtained. Modified ground and excited state properties are predicted in this regime².

Because of the large vacuum Rabi splitting in the ultrastrong coupling regime, the counter-rotating coupling terms and the quadratic field term, which are neglected in the strong coupling case, contribute dominantly to the Hamiltonian. The ground state of such system is predicted to be a squeezed vacuum state containing correlated pairs of cavity virtual photons which could potentially be released by switching off the coupling nonadiabatically³. On the other hand, the quadratic field term prohibits having a superradiant quantum critical point (no-go theorem)⁴. However, if one uses a material with linear dispersion instead of the one with parabolic dispersion, the new system is predicted to show a superradiant phase transition at a coupling rate of 50% of the bare resonant frequency called Dicke phase transition⁵⁻⁷. Consequently, graphene seems to be promising as a material with linear dispersion, although there are some debates about it^{5,6}.

In this work, we would like to investigate experimentally the validity of proposed theory in reference⁵. To do so, a high mobility graphene flake has to be coupled to terahertz (THz) metamaterial resonators. Applying a magnetic field \vec{B} perpendicular to the graphene surface induces a cyclotron resonance. Since the carriers are confined in z-direction, the energies of the cyclotrons are quantized (Landau levels). The transitions between these levels in graphene lie in THz regime and can be coupled to our THz metamaterial resonators.

The constitutive relation for the coupling strength is $\hbar\Omega = d \times E_{vac} \times \sqrt{N}$ ^{8,9}. Considering a graphene sample coupled to a simple cavity resonator ($\omega_{cav} = \frac{c\pi}{L_z\sqrt{\epsilon}}$), one can calculate the normalized coupling strength as in

reference⁵

$$\frac{\Omega}{\omega_c} \approx \sqrt{\nu} \sqrt{\frac{\alpha g_s}{\pi\sqrt{\epsilon}}} \quad (1)$$

which can be tuned by increasing the filling factor(ν). In our system, a single or an array of complementary split-ring resonators(CSRRs) are used as cavity (figure 2(a)). In this case, Ω can be enhanced very efficiently by decreasing the cavity volume. With the same approach as in reference⁵, the normalized coupling ratio in our case can be simplified as

$$\frac{\Omega}{\omega_c} \simeq \sqrt{\nu} \sqrt{\frac{\alpha g_s}{\epsilon}} \sqrt{\frac{\lambda_{cav}}{L_{zeff}}}. \quad (2)$$

Observing ultrastrong coupling in graphene needs a high mobility sample to overcome the loss rate due to the scattering. Indeed, it allows electrons to complete their cyclotron orbit without engaging in a collision.

II. EXPERIMENT AND RESULTS

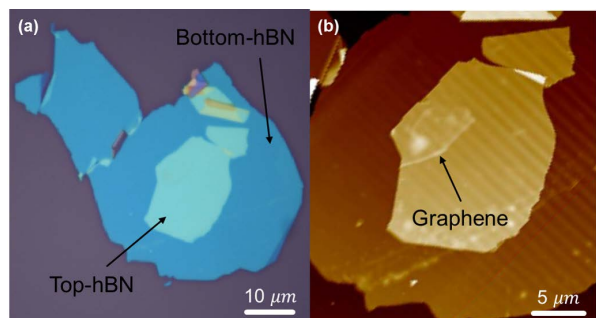


FIG. 1: (a) Optical microscope (b) and atomic force microscopy image of a hBN/graphene/hBN stack using the method suggested in reference¹⁰.

There are several ways to fabricate high mobility graphene sample such as: suspended graphene¹¹⁻¹³, hexagonal Boron Nitride (hBN)/graphene stacks^{10,14}, and chemically vapor deposited stacks¹⁵. We are working on hBN/graphene/hBN stacks. Figure 1 shows optical and atomic force microscope figures of a sandwiched

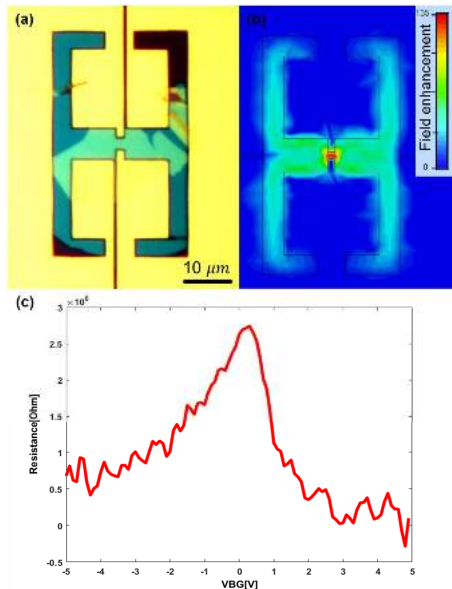


FIG. 2: (a) Optical microscope image and (b) Electric field distribution simulated by CST microwave simulation for a CSRR fabricated on the hBN/graphene/hBN stack. (c) The resistance measurement vs. back gate voltage (V_{BG}) for the CSRR with a bias voltage of $V_{DS} = 0.1$ V.

mono-layer graphene between two hBN flakes. A CSRR on top of the stack (figure 2(a)) can enhance the electric field at its center up to 135 times (according to the simulation with CST microwave Studio shown in figure 2(b)). The two cuts around the resonator separate its left and right sides to form drain and source. With this design, electrical and optical measurements can be done simultaneously. A Dirac curve of this sample is measured and shown in figure 2(c). According to the literature^{10,14}, the mobility of a graphene stack with 2.45V full width at half maximum (FWHM) of the Dirac curve is very promising (comparable with the samples having the mobility around $100,000 \text{ cm}^2/\text{Vs}$). At the moment, we are working to improve the resistance which is still too high probably due to the poor contacts.

Moreover, having a doped substrate to be able to gate the graphene at low temperature leads to a decrease in the quality factor of the cavity resonance which is another technical point to be taken into account.

To conclude, our ongoing research topic is to ultra-strongly couple the graphene cyclotron transitions with CSRRs in order to verify Dicke phase transition in the high coupling rates. To reach this goal, a high mobility graphene is needed for a low loss matter-side, as well as an optimized CSRR for the light-side.

- ¹ J. M. Raimond, M. Brune, and S. Haroche, “Manipulating quantum entanglement with atoms and photons in a cavity,” *Rev. Mod. Phys.*, vol. 73, pp. 565–582, Aug 2001.
- ² C. Ciuti, G. Bastard, and I. Carusotto, “Quantum vacuum properties of the intersubband cavity polariton field,” *Phys. Rev. B*, vol. 72, p. 115303, Sep 2005.
- ³ S. D. Liberato, C. Ciuti, and I. Carusotto, “Quantum vacuum radiation spectra from a semiconductor microcavity with a time-modulated vacuum rabi frequency,” *Phys. Rev. Lett.*, vol. 98, p. 103602, Mar 2007.
- ⁴ P. Nataf and C. Ciuti, “No-go theorem for superradiant quantum phase transitions in cavity qed and counterexample in circuit qed,” *Nature Communications*, vol. 1, pp. 72 EP –, Sep 2010. Article.
- ⁵ D. Hagenmüller and C. Ciuti, “Cavity qed of the graphene cyclotron transition,” *Phys. Rev. Lett.*, vol. 109, p. 267403, Dec 2012.
- ⁶ L. Chirolli, M. Polini, V. Giovannetti, and A. H. MacDonald, “Drude weight, cyclotron resonance, and the dicke model of graphene cavity qed,” *Phys. Rev. Lett.*, vol. 109, p. 267404, Dec 2012.
- ⁷ F. Valmorra, G. Scalari, C. Maissen, W. Fu, C. Schenberger, J. W. Choi, H. G. Park, M. Beck, and J. Faist, “Low-bias active control of terahertz waves by coupling large-area cvd graphene to a terahertz metamaterial,” *Nano Letters*, vol. 13, no. 7, pp. 3193–3198, 2013. PMID: 23802181.
- ⁸ D. Hagenmüller, S. De Liberato, and C. Ciuti, “Ultrastrong coupling between a cavity resonator and the cyclotron transition of a two-dimensional electron gas in the case of an integer filling factor,” *Phys. Rev. B*, vol. 81, p. 235303, Jun 2010.
- ⁹ G. Scalari, C. Maissen, S. Cibella, R. Leoni, P. Carelli, F. Valmorra, M. Beck, and J. Faist, “Superconducting complementary metasurfaces for thz ultrastrong light-matter coupling,” *New Journal of Physics*, vol. 16, no. 3, p. 033005, 2014.
- ¹⁰ L. Wang, I. Meric, P. Y. Huang, Q. Gao, Y. Gao, H. Tran, T. Taniguchi, K. Watanabe, L. M. Campos, D. A. Muller, J. Guo, P. Kim, J. Hone, K. L. Shepard, and C. R. Dean, “One-dimensional electrical contact to a two-dimensional material,” *Science*, vol. 342, no. 6158, pp. 614–617, 2013.
- ¹¹ K. Bolotin, K. Sikes, Z. Jiang, M. Klima, G. Fudenberg, J. Hone, P. Kim, and H. Stormer, “Ultrahigh electron mobility in suspended graphene,” *Solid State Communications*, vol. 146, no. 910, pp. 351 – 355, 2008.
- ¹² X. Du, I. Skachko, A. Barker, and E. Y. Andrei, “Approaching ballistic transport in suspended graphene,” *Nat Nano*, vol. 3, pp. 491–495, Aug 2008.
- ¹³ D.-K. Ki and A. F. Morpurgo, “High-quality multiterminal suspended graphene devices,” *Nano Letters*, vol. 13, no. 11, pp. 5165–5170, 2013. PMID: 24080018.
- ¹⁴ F. Pizzocchero, L. Gammelgaard, B. S. Jessen, J. M. Caridad, L. Wang, J. Hone, P. Bøggild, and T. J. Booth, “The hot pick-up technique for batch assembly of van der waals heterostructures,” *Nature Communications*, vol. 7, pp. 11894 EP –, Jun 2016. Article.
- ¹⁵ L. Banszerus, M. Schmitz, S. Engels, J. Dauber, M. Oellers, F. Haupt, K. Watanabe, T. Taniguchi, B. Beschoten, and C. Stampfer, “Ultrahigh-mobility graphene devices from chemical vapor deposition on reusable copper,” *Science Advances*, vol. 1, no. 6, 2015.

A double junction segmented ion trap with integrated optical delivery

Chiara Decaroli¹ and Jonathan Home¹

¹*Institute of Quantum Electronics, ETH-Hönggerberg, CH-8093, Zürich, Switzerland*

Ion traps are a robust and promising platform for quantum information processing and for the implementation of a quantum computer. However, major challenges exist in scaling these systems to the level required for full-scale quantum computing. I will describe work concerned with addressing two of these challenges; namely connecting multiple trap zones in more than one dimension, and integrating laser light delivery into the trapping structures.

I. MOTIVATION

In the last few decades, the limitations of classical computation have motivated scientists to turn to quantum computation. Quantum algorithms that can outperform classical algorithms were developed, such as Shor's factoring algorithm¹. While we don't yet have a quantum computer, a number of quantum systems are known to be good candidates for its implementation. In the attempt of identifying the key requirements for a quantum system to be a viable quantum computer, the Di Vincenzo criteria were formulated², and in 1995 Cirac and Zoller proposed cold trapped ions as a promising system to realise a quantum computer³.

Trapped ions satisfy all of the Di Vincenzo criteria: a subset of the atomic levels is chosen as the qubit, it is chosen to have very long decoherence times⁴. Optical pumping is used for state initialisation and qubit readout performed by state dependent resonance fluorescence collection⁵. Finally, a universal set of quantum gates can be realised⁶ using laser light, inducing Rabi oscillations for single-qubit rotations and light-induced forces combined with the inter-ion Coulomb repulsion for multi-qubit gates.

There is, however, an important criterion on which research is still open: that the system can be scaled to a large number of qubits while still satisfying all other criteria⁷.

One approach towards scalability⁸ is that of creating a trap with several trapping regions. This allows gates to be performed on small numbers of ions, and that gates can be performed in parallel on ions stored in different regions of the processor. In a standard linear rf Paul trap, an almost harmonic three dimensional potential is created by a combination of static (dc) and oscillating (rf) electric fields. The rf fields provide a tight confinement in the radial directions, and are not confining in the axial direction. In order to confine the ions in the axial direction, dc fields are applied. Shifting dc fields also allows for transport of the ions and splitting of potential wells. Linear traps, however, have a limitation: as the ions are arranged in a linear string, it is impossible to arbitrarily entangle two ions separated by a long string of other ions. In order to achieve order

switching on a large number of ions, junction traps have been proposed⁹. The three main junction geometries are the 'T' (a), 'X' (b) and 'Y' (c) junctions as shown in Figure 1. The ability to transport ions across a junction allows for reordering of ions and transfer of quantum information. The ultimate goal is to be able to create several of such units to realise a large scale array where a large number of ions are manipulated.

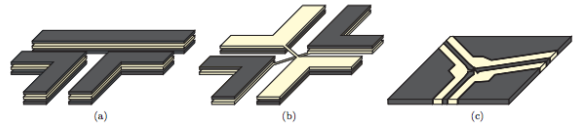


FIG. 1: Junction trap geometries: T⁹, X⁸ and Y.

Our work focuses on pursuing the scalability requirement, by the creation of a double-junction ion trap in which ions will be transported, stored, split and recombined. The trap geometry and the electric fields provide control over the motion of the ions, while laser light is used to perform quantum gates and state detection. Our novel trap will introduce new features to improve both the ion motion control and the ion manipulation. We make use of a new fabrication technique based on subtractive 3D printing and we are developing a new method for integration of optical delivery within the trap structure.

II. TRAP DESIGN

We envision our trap to have three experimental zones where quantum gates are applied, several splitting and recombining zones and storage zones located along the vertical legs of the junction. The trap is made of a stack of silica glass wafers, two host the junction trap structure, the middle wafer is used for optical integration and outer wafers hold shim electrodes for stray electric field compensation. With these requirements in mind, the design of the trap must take into account several aspects.

One of the most detrimental effects for manipulation of ions is a decoherence mechanism called the heating rate. It has been demonstrated¹⁰ to follow a behaviour $\propto r^{-3.5}$, with r the electrode-ion distance, and to be associated with imperfections of electric field

surface structures. A compromise between high secular frequencies (smaller trap) and low heating rates (larger trap) has to be made.

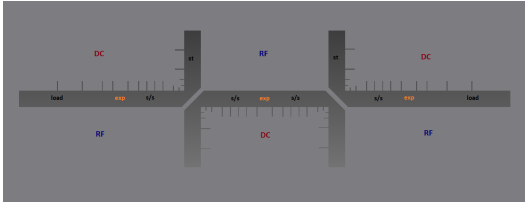


FIG. 2: A double X junction trap top wafer, the trapping zones and shown and their function labelled. Rf bridges connect the rf electrodes. Dc electrodes are segmented.

The drive frequency is determined by consideration of ion motion stability in the trap. The maximum voltages applied to the electrodes, which are segmented, is determined by the breakdown voltage. The electrodes geometry affects both the ability to split and recombine potential wells, and the transport of ions across the junction.

Finally, optical access and delivery constrain the design. The integration of optical elements within the trap affects the thickness of the middle wafer, in turn the trap geometry determines the optical access angle through which light is collected for state detection. The optical access angle is optimised by tapering the electrode fingers.

TABLE I: A comparison of 3D multilayer trap dimensions.

Reference	trap dim (μm)	op angle ($^\circ$)	el-ion (μm)
Blakestad	200x250	34	160
Josts	200x220	45	140
Kienzler	350x125	43	186

Table 1 shows a comparison of dimensions, optical access

angles and electrode-ion distances of the main segmented traps which have been successfully operated. Our trap, with dimensions 300x220 μm and electrode-ion distance 185 μm will have an optical access angle of 50°. It resembles the most the X junction trap developed by Blakestad⁸, and it extends it including two junctions and the integrated optical delivery.

III. NOVEL FEATURES

There are two main novel features in our design: first, the use of a new selective subtractive 3D printing technology to fabricate the wafers. This technology offers a way of incorporating the alignment of the wafers into the trap structure, minimising misalignment and providing a way to create larger arrays of traps. Secondly, the integration of optical delivery via micro-lensed optical fibres. Optical fibres have been successfully used to collect light in surface traps¹², however for 3D multilayer traps light delivery has not been demonstrated yet. We plan to either use lensed optical fibres or compact multi-lens objectives¹³ on the tip of the fibres in order to achieve a beam waist of <20 μm for a working distance of 200 μm .

IV. SUMMARY

We are working on the design and fabrication of a novel segmented 3D ion trap featuring two X-junctions and delivery of light integrated within the trap wafers. This work will be useful in investigating approaches to scalability of quantum computers.

Acknowledgments

We kindly thank QSIT and the Swiss National Science Foundation.

¹ P. Shor, *Algorithms for quantum computation: discrete logarithms and factoring.*, 35th Annual Symposium on the Foundations of Computer Science **35**, 124 (1994).

² D. DiVincenzo and D. Loss, *Quantum information is physical.*, Superlattices Microstruct. **23**, 419 (1998).

³ J. Cirac and P. Zoller, *Quantum Computations with Cold Trapped Ions.*, Phys. Rev. Lett. **74**, 40914094 (1995).

⁴ D. Lucas and et al., *A long-lived memory qubit on a low-decoherence quantum bus.*, arXiv:0710.4421v1 (2007).

⁵ D. Leibfried and et al., *Experimental preparation and measurement of quantum states of motion of a trapped atom.*, J. Mod. Opt. p. 2485 (1997).

⁶ J. Benhelm, G. Kirchmair, C. Roos, and R. Blatt, *Towards fault-tolerant quantum computing with trapped ions.*, Nature Phys **4**, 463466 (2008).

⁷ D. Kielpinski, C. Monroe, and D. Wineland, *Architecture*

for a Large-Scale Ion-Trap Quantum Computer., Nature **417**, 709711 (2002).

⁸ B. Blakestad, Ph.D. thesis, University of Colorado (2010).

⁹ H. W. K. and et al., *T-junction ion trap array for two-dimensional ion shuttling, storage, and manipulation.*, Appl. Phys. Lett. (2005).

¹⁰ L. Deslauriers and et al., *Scaling and suppression of anomalous heating in ion traps*, Phys. Rev. Lett. **97**, 103007 (2006).

¹¹ D. Kienzler, Ph.D. thesis, ETH (2015).

¹² A. VanDevender and et al., *Efficient Fiber Optic Detection of Trapped Ion Fluorescence.*, PRL p. 105 (2010).

¹³ T. Gissibl and et al., *Two-photon direct laser writing of ultracompact multi-lens objectives.*, Nature Photonics p. 10 (2016).

Towards Ground State Cooling of Optically Levitated Nanoparticle

Felix Tebbenjohanns,¹ Vijay Jain,¹ and Lukas Novotny¹

¹Photonics Laboratory, ETH-Hönggerberg, CH-8093, Zürich, Switzerland

Recent progress in the laser control of optically levitated nanoparticles has resulted in cooling of the center of mass motion from room temperature into the micro-Kelvin regime. Limitations to further reducing the motion arise from limited measurement precision, which affects the performance of an active feedback control scheme. Here, we propose changes to the particle tracking design in order to increase the detection efficiency. With this new design, we will overcome precision limits in detecting and controlling the movement of a levitated nanoparticle in three dimensions with the ultimate goal of cooling it into its quantum ground state.

I. INTRODUCTION

Remarkable advances in the optical control of micro- and nano-scale resonators has resulted in cooling of macroscopic objects into the quantum ground state^{1,2}. Despite elegant low-loss designs of micro-structured devices, decoherence due to acoustic vibrations from clamping losses limit the ground-state occupation time and prohibit measurement schemes in the domain of macroscopic quantum control. To overcome this limitation, we optically levitate nanoparticles in vacuum, which assures an open geometry that is devoid of clamping losses. A levitated nanoparticle would undergo several oscillation cycles in its ground state of motion before its motion is decohered by quantum fluctuations of the light field³. Current developments in optical levitation have demonstrated that a nanoparticle's motion can be extremely well controlled and as such provides a useful platform for both sensing and precision tests of the fundamental laws of physics³⁻⁵.

The motion of an optically trapped particle in vacuum is well described by a prototypical mass m on a spring. Its center of mass motion resembles a thermally driven, underdamped harmonic oscillator, whose equation of motion is given by

$$\ddot{y} + \gamma\dot{y} + \Omega_0^2 y = \frac{1}{m} (\mathcal{F}_{\text{fluct}}(t) - k(t)y) \quad (1)$$

The left side of the equation describes an harmonic os-

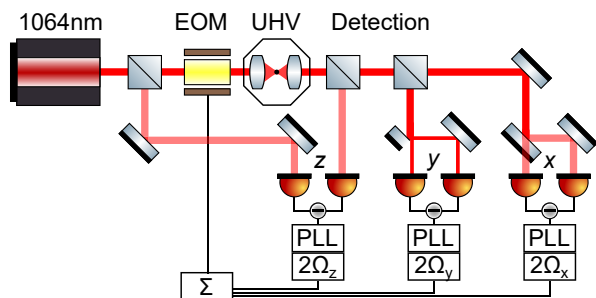


FIG. 1: Optical set-up. A 1064 nm laser is used to trap a particle in ultra high vacuum. Its motion is detected in all three directions using balanced photodetectors and parametric feedback is used to cool the motion.

cillator with resonance frequency Ω_0 and damping rate γ , which are given by the gradient of intensity in the focus and gas pressure, respectively. Collisions with residual air molecules (at large pressures) and photons (at ultra low pressures) give rise to a fluctuating force, $\mathcal{F}_{\text{fluct}}$. According to the fluctuation-dissipation theorem, a fluctuating force leads to both damping and heating, which we control using a time-varying parameter, $k(t)$. It reflects a modulation of the beam intensity which affects the trapping spring constant accordingly.

By applying parametric feedback ($k(t) \propto y\dot{y}$) the motion of the particle can be cooled into the micro-Kelvin regime⁴.

To identify the limitations to measurement precision in the y direction, we turn to the power spectral density of displacement, which is comprised of three dominant contributions (imprecision, backaction, and feedback noise)

$$S_y(\Omega) = S_y^{\text{imp}}(\Omega) + S_y^{\text{back}}(\Omega) + S_y^{\text{FB}}(\Omega). \quad (2)$$

Measurement imprecision originates from limited detection efficiency and shot-noise on the detector. Measurement backaction results from photons that scatter from the particle and heat it up. Feedback noise results from additional imprecisions in determining y that are fed back onto the particle. The first two terms can be expressed on resonance Ω_0 as³

$$S_y^{\text{imp}}(\Omega_0) = \frac{\hbar c^2}{8\pi\omega_0\eta_c} \frac{1}{P_{\text{scatt}}}, \quad (3)$$

$$S_y^{\text{back}}(\Omega_0) = \frac{\hbar\omega_0}{5\pi m^2 c^2 \gamma^2 \Omega_0^2} P_{\text{scatt}} \quad (4)$$

where ω_0 is the light's angular frequency, m is the mass of the particle, η_c is the total detection efficiency, and P_{scatt} is the scattered power from the particle. The latter term decreases imprecision noise and increases backaction noise. It can be controlled by the incident power which enables us to set both terms equal for minimum contribution.

Further reducing the noise is only possible by increasing η_c , which accounts for the fraction of the scattered power that reaches the detector, the detector's conversion efficiency, and the efficiency of mapping the particle's displacement into a phase shift of the beam.

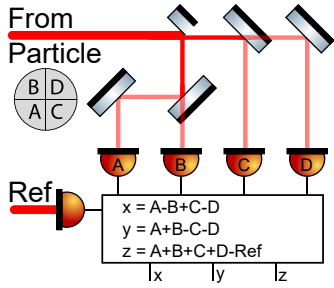


FIG. 2: Scheme of the updated detection. The beam is split into its four quadrants (A, B, C, D) and each of them is measured shot-noise limited. The positions are extracted afterwards by building the indicated sums. Here, *Ref* describes a reference beam which cancels both the DC photocurrent and common mode noise of the laser beam. Thus, all available information in the beam can be used to determine the particle's position.

II. HIGH POWER PHOTODETECTION

The total power collected from the trap in our experiment is around 70 mW, which saturates high bandwidth, off-the-shelf photodetectors. Rather than attenuate the optical signal and reduce the effective η_c , we built high power photodetectors with 1 MHz bandwidth and shot-noise limited performance. At the moment, the beam leaving the chamber is split three ways and balanced photodetection is used to determine the position in each direction (see Figure 1). In the current scheme we are therefore bound to trade the accuracy of the measurement between the three directions.

We propose a different detection scheme as illustrated in Figure 2 that harnesses high-power detection in all three dimensions. Here, the outgoing beam is split into four quadrants each of which is measured above a shot-noise limited noise floor. An additional reference input enables optimal three-dimensional detection for further cooling. The scheme is equivalent to that of a quadrant photodetector which is commonly used in optical tweezers with the advantage of making use of high-power photodiodes which do not exist off-the-shelf in a quadrant version.

Building such detectors is an electronic challenge because the DC current generated by the laser light is not automatically canceled like in balanced photodetectors. A high DC offset requires either limiting the transimpedance amplifier's gain or reducing the optical power, which is sub optimal in both regards due to a limited signal-to-noise ratio. To overcome this challenge, we will incorporate low noise current sources on each detector such that the DC photocurrent is subtracted away prior to transimpedance amplification (see Figure 3). The technical challenge here is that the current source needs to be shot-noise limited. As a side-product, we will be able to read out classical laser noise to stabilize the beam to unprecedented accuracy.

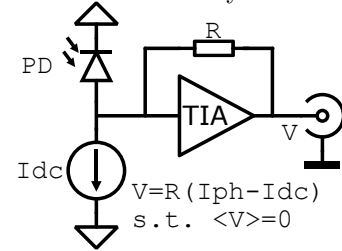


FIG. 3: Simplified schematic of single photodetector. The current source I_{DC} is controlled such that it cancels the DC of the photocurrent as to maximize the detector's gain R and dynamic range at frequencies of interest. The current source needs to be less noisy than equivalent shot-noise.

Using the high power photodetector we increased η_c enough to cool the particle's y -axis motion to $145\mu K$ or, equivalently, $n = 21$ phonons⁶. With the proposed quadrant detection scheme we expect to cool all three axes to similar temperatures. In addition, any remaining coupling effects between the three spatial modes will be equivalently reduced.

Acknowledgments

We acknowledge support from QSIT (SNF grant 51NF40-160591).

¹ J. Chan, T. P. M. Alegre, A. H. Safavi-Naeini, J. T. Hill, A. Krause, S. Grblacher, M. Aspelmeyer, and O. Painter, *Laser cooling of a nanomechanical oscillator into its quantum ground state*, Nature **478**, 8992 (2011).
² R. Riviere, S. Delglise, S. Weis, E. Gavartin, O. Arcizet, A. Schliesser, and T. J. Kippenberg, *Optomechanical sideband cooling of a micromechanical oscillator close to the quantum ground state*, Physical Review A **83** (2011).
³ V. Jain, J. Gieseler, C. Moritz, C. Dellago, R. Quidant, and L. Novotny, *Direct measurement of photon recoil from a*

levitated nanoparticle, Phys. Rev. Lett. **116**, 243601 (2016).
⁴ J. Gieseler, B. Deutsch, R. Quidant, and L. Novotny, *Subkelvin parametric feedback cooling of a laser-trapped nanoparticle*, Phys. Rev. Lett. **109**, 103603 (2012).
⁵ T. Li, *Fundamental tests of physics with optically trapped microspheres* (Springer, 2013).
⁶ V. Jain, F. Tebbenjohanns, and L. Novotny, in *Frontiers in Optics* (Optical Society of America, 2016).

Scalable cryogenic experiment for trapped-ion quantum computing

Roland Matt,¹ Robin Oswald,¹ John McCann,¹ Joseba Alonso,¹ and Jonathan Home¹

¹*Trapped Ion Quantum Information group (TIQI),
Institute of Quantum Electronics, ETH-Hönggerberg, CH-8093, Zürich, Switzerland*

In this paper, we discuss the physical challenges en route to fault-tolerant scalable quantum computation with trapped atomic ions and possible technical solutions to overcome them used in the TIQI group.

I. INTRODUCTION

Trapped atomic ions are promising candidates for implementing scalable quantum information processing (QIP). Their internal electronic states can be used as quantum information carrying two-level systems called qubits. Hyperfine ground-level atomic levels have very long lifetimes, with transitions in the microwave regime which can be resilient to first-order Zeeman shifts caused by magnetic field fluctuations¹. Current QIP devices based on trapped ions² require multiple powerful laser sources with accompanying optics which impose increasing technical complications as systems grow larger. One promising alternative is to drive qubits using near-field microwaves produced by current carrying structures in the trap³, in which case the gate times become dependent on the size scale of the trap and logical gates become immune to photon scattering error - a relevant source of infidelity for laser-driven gates. Universal quantum computation becomes possible when the decoherence of quantum states is controlled and logical gate infidelities are below the fault-tolerant computation threshold such that error correction becomes possible⁴.

I will describe two areas of development towards scaling up ion trap quantum computers. In the first, which comprises a theoretical design study, I have investigated new trap designs for performing multi-qubit control using only microwave (MW) fields. This would obviate the need for high power control lasers and may be easier to scale. In the second part of my talk, I will describe the development of a new cryogenic apparatus for testing new technologies for ion trap control. In the first instance we plan to trap up to 12 ions in a micro-fabricated trap as part of a project to demonstrate a real advantage in quantum error correction. Design considerations as well as experimental progress will be discussed.

II. MICROWAVE DRIVEN QIP

We have designed⁵ a superconducting ion-trap based on multi-layer Niobium processes with novel electrode geometries for magnetic-field-driven QIP. The surface layout (see Fig.1) shows three long MW electrodes used to create the magnetic-field gradient for driving multi-qubit gates and ten small current carrying electrodes for single ion addressing. These have been integrated between the RF and DC electrodes which form the conventional sur-

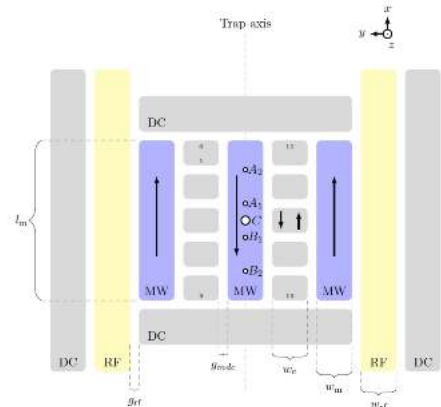


FIG. 1: Proposed trap layout. The main trapping position is marked with C . Arrows on the microwave (MW) lines show the current directions during one half of the MW period. The three MW lines could be independently controlled or connected in subsurface layers. The small addressing electrodes (one marked with $\downarrow\uparrow$) can be used for both DC control and applying magnetic fields.

face electrode Paul trap. Multi-layer fabrication makes it possible to use “island”-like electrodes (connectors can be hidden in sub-surface layers) and superconducting materials tolerate high currents without resistive loss. Scaling to smaller traps is promising because it allows for faster microwave gates but is currently limited by anomalous motional heating⁶.

III. OUR SETUP

We are building a next generation setup (see Fig.2) which houses the ion trap in a cryogenic environment. A low working temperature (<10 K) helps to decrease the ions’ unwanted interaction with the surrounding environment therefor reducing decoherence of quantum states. Firstly, the cryostat acts as a cryo-pump creating ultra high vacuum which reduces the possibility of collisions with background gasses. Secondly, low temperature lead to the reduction of anomalous motional heating. Thirdly, the increase of electrical conductivity leads to lower resistive losses (electrical heating of the trap which becomes important when driving high power microwave currents) and decreased skin depth which means that conducting enclosures can be used for shielding AC magnetic field

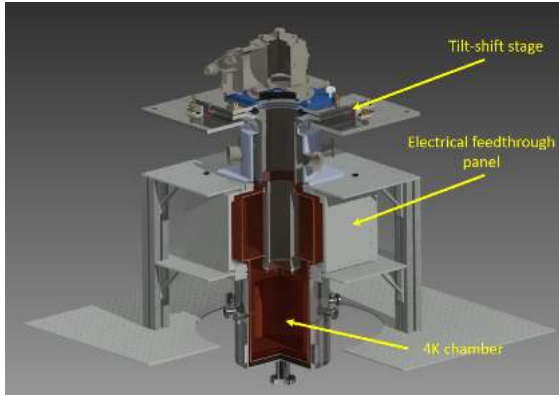


FIG. 2: The trap cryostat design, including an electronics test chamber with large panels for many electrical connections and a positioning stage for avoiding mechanical connections between the vibrating pulse tube head and the low-temperature stage.

fluctuations.

The cold head of the low vibration cryogenic refrigerator operating on the Gifford-McMahon cycle is housed in a two-part vacuum chamber. The rectangular vacuum chamber provides room for cryogenic digital-to-analog converters which should help to reduce the number of through-vacuum connections, signal latency, and noise pick-up. The cylindrical chamber holds viewports for optical access and surrounds a thick-walled copper chamber housing the trap (see Fig.3). Light collection and optical addressing of ions is realized using a high NA objective lens. The new setup will make use of superconducting coils in a self-shielding configuration⁷ close to the trap, providing a stable quantization magnetic field and shielding of even sub-hertz fluctuations.

IV. FIRST PLANNED EXPERIMENTS

The first trap this setup will test is a high-optical access trap built by Sandia National Laboratories. The long-term aim is to realize an error-free logical qubit com-

prised of at least seven Ca^+ ions as physical qubits.

Parallel individual control of up to seven ions in a Coulomb crystal will be tested using a setup where seven individual optical fibers are connectorized to seven cores of a multi-core photonic crystal fiber which is then tightly focused to address the ions. What is more, parallel readout can be realized with a low noise sensor array such as an electron multiplying CCD or a CMOS sensor. If the parallel readout has sufficiently low latency then it can be integrated with the field-programmable gate-array-based control system for implementing run-time feedback for error-correction protocols.

We plan to trap even Ca^+ isotopes for encoding qubits into the decoherence-free subspace of ion-pairs. In this way, the logical qubits are immune to collective dephasing – a major source of decoherence⁸. Good candidates are

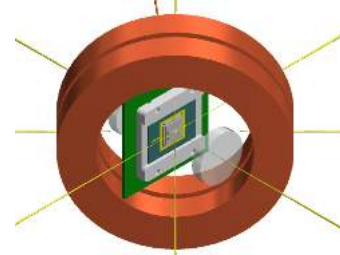


FIG. 3: The schematic drawing of the surface electrode trap mount including to-scale self-shielding coils and objective lenses. This is housed in the 4 K chamber. Laser beam directions shown in yellow.

the two most abundant isotopes $^{40}\text{Ca}^+$ and $^{44}\text{Ca}^+$.

V. SUMMARY

We are developing a modular setup for trapped ion QIP with parallel addressing and readout of seven ions and a novel superconducting self-shielding setup. This setup will soon be followed by a second iteration which will be used as a testbed for emerging technical solutions.

¹ D. A. Craik, N. Linke, T. Harty, C. Ballance, D. Lucas, A. Steane, and D. Allcock, *Microwave control electrodes for scalable, parallel, single-qubit operations in a surface-electrode ion trap*, Applied Physics B **114**, 3 (2014).

² S. Debnath, N. M. Linke, C. Figgatt, K. A. Landsman, K. Wright, and C. Monroe, *Demonstration of a small programmable quantum computer with atomic qubits*, Nature **536**, 63 (2016), ISSN 0028-0836, letter.

³ U. Warring, C. Ospelkaus, Y. Colombe, K. Brown, J. Amini, M. Carsjens, D. Leibfried, and D. Wineland, *Techniques for microwave near-field quantum control of trapped ions*, Physical Review A **87**, 013437 (2013).

⁴ A. M. Steane, *Error correcting codes in quantum theory*,

Physical Review Letters **77**, 793 (1996).

⁵ R. Matt, Master's thesis, ETH Zurich, Switzerland (2016).

⁶ C. Ospelkaus, C. E. Langer, J. M. Amini, K. R. Brown, D. Leibfried, and D. J. Wineland, *Trapped-ion quantum logic gates based on oscillating magnetic fields*, Physical review letters **101**, 090502 (2008).

⁷ G. Gabrielse and J. Tan, *Self-shielding superconducting solenoid systems*, Journal of Applied Physics **63**, 5143 (1988).

⁸ D. Kielpinski, V. Meyer, M. Rowe, C. Sackett, W. M. Itano, C. Monroe, and D. J. Wineland, *A decoherence-free quantum memory using trapped ions*, Science **291**, 1013 (2001).

Photovoltaic THz photoresponse of high mobility two-dimensional electronic materials due to cyclotron resonance

Felice Appugliese,¹ Gian Lorenzo Paravicini Bagliani,¹ Elena Mavrona,¹ Giacomo Scalari,¹ Werner Wegscheider,¹ and Jérôme Faist¹

¹*Institute of Quantum Electronics, ETH-Hönggerberg, CH-8093, Zürich, Switzerland*

We investigate Landau level spacing of two-dimensional electronic systems measuring the photovoltage response. We show preliminary results obtained for a Hall bar fabricated on a GaAs/Al_{0.3}Ga_{0.7}As single triangular quantum well. This configuration can be exploited to study ultra strongly coupled system consisting of THz sub-wavelength resonators on the top of 2 dimensional electron gas Hall bars.

I. INTRODUCTION

Light-matter interaction is the cornerstone of quantum electrodynamics (QED). It is possible to discriminate different regimes, depending on the coupling strength between the light part (cavity photon) and the matter part (elementary electronic oscillation). The relevant quantity describing this coupling is the vacuum Rabi frequency Ω : when Ω is larger than the losses of the system we speak of strong coupling regime. When the vacuum Rabi frequency becomes comparable to the unperturbed frequency of the system we speak about ultra strong coupling. The main feature of this regime is the presence of a squeezed ground vacuum state, containing virtual photons¹. Experimentally ultra strong coupled states have been demonstrated in different systems^{2,3}. Applying magnetic field to a high mobility two dimensional electron gas (2DEG) creates a quantum harmonic oscillator. The energy levels of this system are the so called Landau levels. The distance between two levels is given by the cyclotron frequency, which can be described as:

$$\omega_c = \frac{eB}{m^*}. \quad (1)$$

where e is the charge and m^* is the effective mass. The number of occupied levels at zero temperature is determined by the filling factor, which depends on the density of the electrons (ρ).

$$\nu = \frac{h\rho}{|e|B}. \quad (2)$$

Ultra strong coupling has already been demonstrated in systems where sub-wavelength LC resonators are placed on the top of 2DEGs in strong perpendicular magnetic fields².

It has been suggested to exploit the cyclotron photoresponse, in order to study the Landau level spacing of two dimensional materials⁴. This can be implemented by measuring the photovoltage of hall bars under the illumination of a THz source in high magnetic fields.

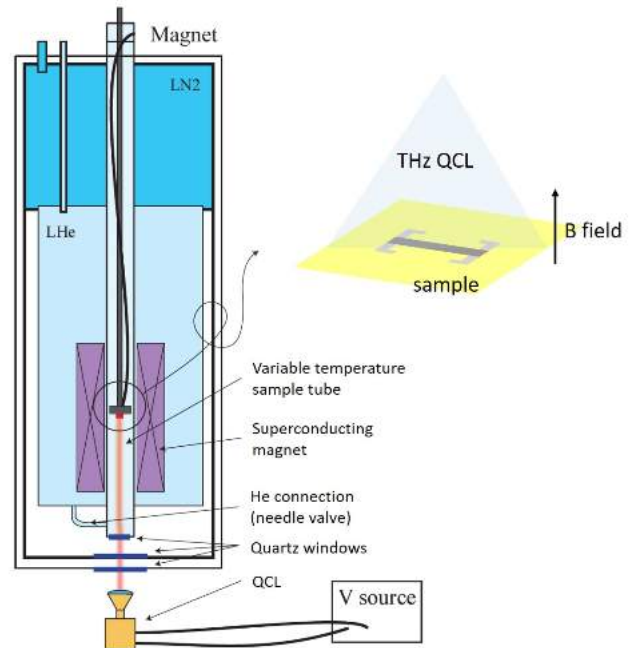


FIG. 1: Schematic picture of the setup. The sample is shined with a 3.2 THz laser in the presence of a strong perpendicular magnetic field inside a superconducting magnet.

II. METHODS

In this work, Landau level spacing of GaAs based 2DEGs and graphene are investigated. The samples are characterized under the illumination of THz quantum cascade lasers (QCLs) in high magnetic fields.

A. Setup

The measurements are performed with a liquid-He-cooled superconducting magnet, allowing to change the magnetic field in the range between -12 to 12 T. The vertical-solenoid magnet is provided with bottom optical opening through quartz windows (Fig.1). The light source is a THz QCL emitting at 3.2 THz, operating at 40 K, with a power of 10 mW.

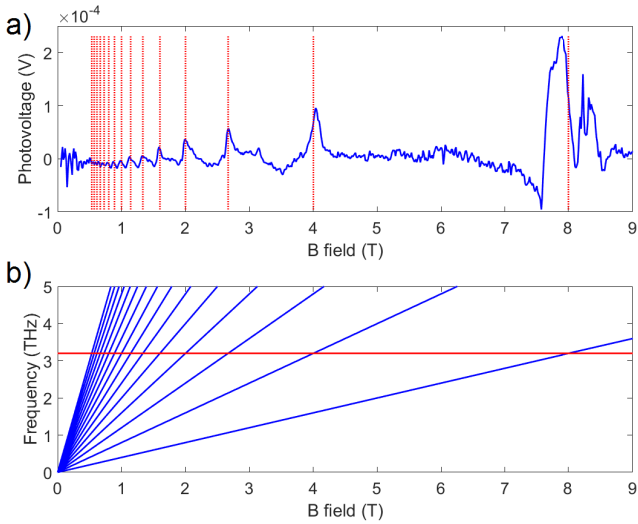


FIG. 2: (a) Measured photovoltage (solid blue) as a function of the magnetic field for a GaAs based hall bar. The predicted value for the absorptions are superimposed (dashed red). (b) Landau fan (blue) and the emitting frequency of the laser (red)

B. Materials: 2DEG and Graphene

The first sample is based on a GaAs/Al_{0.3}Ga_{0.7}As single triangular quantum well 90 nm below the sample surface grown by molecular beam epitaxy by Wegscheider's group². A Si δ -doping layer with density $3.5 \times 10^{12} \text{ cm}^{-2}$ is located 50 nm below the sample surface. The electron transport mobility is $\mu = 2 \times 10^6 \text{ cm}^2/\text{Vs}$ and the electron density is $N = 2.7 \times 10^{11} \text{ cm}^{-2}$ at zero gate bias. In this sample several 4 mm long $3.4 \mu\text{m}$ wide stripes spaced by $300 \mu\text{m}$ were etched, in order to achieve the Hall bars. Afterwards ohmic contacts were placed by evaporating and annealing 18/48/15/150 nm thick Ge/Au/Ni/Au at both ends of each stripe. A two dimensional square array of complementary split-ring resonators with an LC resonance frequency of around 500 GHz and a pitch of $300 \mu\text{m}$ is placed on the stripes. Additionally in the same sample a $300 \mu\text{m}$ long $100 \mu\text{m}$ wide Hall bar was fab-

ricated. The second sample is high-mobility graphene deposited on h-BN. The graphene on h-BN quantum Hall system was prepared using the transfer technique for mechanically exfoliated monolayer graphene, followed by electron-beam lithography, oxygen-plasma etching, and lift-off. The carrier mobility, limited by long-range scattering, is $\mu = 150\,000 \text{ cm}^2/\text{Vs}$ at $T = 4 \text{ K}$. This sample was already characterized in mid-IR regime⁴.

III. PRELIMINARY RESULTS

As shown in figure 2 the photovoltage from a wide hall bar on the GaAs 2DEG was measured. We expect to observe absorptions at positions corresponding to the transitions between different Landau levels. In order to determine the predicted values, it is possible to calculate the Landau fan for our sample, knowing the effective mass of GaAs ($m^* = 0.070$). The crossing between the frequency of the exciting laser and the Landau fan gives the theoretical values of the absorptions. The measurements were performed at 1.2 K. We observed transitions up to the 10^{th} order.

IV. CONCLUSIONS AND OUTLOOK

In this work, Landau level spacing of GaAs based 2DEGs is measured, finding a good agreement between theoretical and experimental values. Following this work we aim to examine the Hall bar in the gap of the gold resonator, in order to explore signature of the ultra strong coupling regime. Finally we will apply this technique to graphene, for which a Dicke phase transition at a coupling rate of 0.5 has been predicted⁵.

Acknowledgments

We acknowledge Prof. T. Machida for the growth of graphene and Prof. K. Ensslin for helpful discussions.

¹ C. Ciuti, G. Bastard, and I. Carusotto, *Quantum vacuum properties of the intersubband cavity polariton field*, Physical Review B **72**, 115303 (2005).

² G. Scalari, C. Maissen, D. Turčinková, D. Hagenmüller, S. De Liberato, C. Ciuti, C. Reichl, D. Schuh, W. Wegscheider, M. Beck, et al., *Ultrastrong coupling of the cyclotron transition of a 2d electron gas to a thz metamaterial*, Science **335**, 1323 (2012).

³ Y. Todorov, A. M. Andrews, R. Colombelli, S. De Liberato, C. Ciuti, P. Klang, G. Strasser, and C. Sirtori, *Ultrastrong light-matter coupling regime with polariton dots*, Physical

review letters **105**, 196402 (2010).

⁴ S. Masubuchi, M. Onuki, M. Arai, T. Yamaguchi, K. Watanabe, T. Taniguchi, and T. Machida, *Photovoltaic infrared photoresponse of the high-mobility graphene quantum hall system due to cyclotron resonance*, Physical Review B **88**, 121402 (2013).

⁵ D. Hagenmüller and C. Ciuti, *Cavity qed of the graphene cyclotron transition*, Physical review letters **109**, 267403 (2012).

Towards quantum scattering at low collision energies with merged beams

Katharina Höveler,¹ Pitt Allmendinger,¹ Johannes Deiglmayr,¹ Otto Schullian,¹ and Frédéric Merkt¹

¹*Institute of Physical Chemistry, ETH-Hönggerberg, CH-8093, Zürich, Switzerland*

As the collision energy approaches zero quantum-mechanical effects start to influence the kinetics of chemical reactions. For barrierless ion-molecule reactions, the quantized angular momentum of the relative motion leads to a discretization of the centrifugal barriers associated with the different partial waves. The reaction $\text{H}_2 + \text{H}_2^+ \rightarrow \text{H}_3^+ + \text{H}$ provides the opportunity to observe quantum effects at collision energies around $k_B \cdot 1 \text{ K}$. In past experiments, the cross section could be measured down to collision energies of $k_B \cdot 60 \text{ K}$, limited by the presence of stray electric field effects. To avoid these effects, we substitute the ionic reactant by the ionic core of a molecule in a high Rydberg state. The Rydberg electron for states with a principal quantum number $n \geq 20$ does not influence the reaction but provides electric neutrality. We exploit a curved Rydberg-Stark surface-electrode deflector to merge two supersonic beams. The collision energy is tuned by adjusting the temperature of the supersonic valves or by the Rydberg-Stark deceleration. We measure the cross section at collision energies from $k_B \cdot 60 \text{ K}$ down to temperatures below $k_B \cdot 1 \text{ K}$ where deviations from classical Langevin capture model behaviour were observed, primarily caused by the influence of the quadrupole and the quantized rotation of H_2 .

I. INTRODUCTION

Ion-molecule reactions are important chemical processes in low-density gaseous environments. Many ion-molecule reactions are exothermic and have low reaction barriers or are barrierless, and have large rate coefficients even at very low temperatures, for which exothermic reactions with a barrier are exponentially suppressed. The temperature dependence of barrierless ion-molecule reactions is often described by the classical Langevin capture model. This model approximates the reaction by a classical collision of two reactants with reduced mass μ and asymptotic relative velocity v_{rel} in a long-range interaction potential between a charge e (the ion) and the induced dipole moment of the neutral molecule with polarizability α . A reaction occurs with 100% probability if the initially available energy, $E_{\text{coll}} = \frac{1}{2}\mu v_{\text{rel}}^2$ is larger than the centrifugal barrier resulting from the contribution $\frac{L^2}{2\mu R^2}$ to the effective potential $V_{\text{eff}}(R)$:

$$E_{\text{coll}} = \frac{1}{2}\mu \left(\frac{dR}{dt}\right)^2 + \frac{L^2}{2\mu R^2} + V(R) = \frac{1}{2}\mu \left(\frac{dR}{dt}\right)^2 + V_{\text{eff}}(R),$$

where $V(R) = -\frac{1}{2}\alpha|\vec{E}_{\text{ion}}|^2 = -\frac{1}{2}\alpha\left(\frac{e}{4\pi\epsilon_0 R^2}\right)^2$. Collisions with angular momenta smaller than the maximum angular momentum $L_{\text{max}} = \mu v_{\text{rel}} b_{\text{max}}$ corresponding to a maximal impact parameter b_{max} , have sufficient energy to overcome the centrifugal barrier and contribute to the cross section $\sigma = \pi b_{\text{max}}^2$. The classical Langevin rate coefficient

$$k_{\text{L}} = \sigma v_{\text{rel}} = \frac{e}{\epsilon_0} \sqrt{\frac{\alpha}{4\mu}} \quad (1)$$

is independent of v_{rel} and T . A classical example of a reaction following the Langevin model is the reaction $\text{H}_2 + \text{H}_2^+ \rightarrow \text{H}_3^+ + \text{H}^1$, as confirmed by Glenewinkel-Meyer and Gerlich down to collision energies corresponding to 60 K.² Deviations from the purely classical Langevin model are expected for collision energies much below 1 K, where the de Broglie wavelength associated with the rela-

tive velocity of the collision partners becomes comparable or larger than the size of the reacting molecules. The angular momentum of the relative motion of the approaching reaction partners is quantized: $|\vec{L}| = \hbar\sqrt{L(L+1)}$, leading to barrier heights that depend on the collisional partial wave. The total cross section is the sum of contributions from all partial waves that correspond to centrifugal barriers with maxima below the collision energy. As $T \rightarrow 0$, s-wave scattering becomes dominant. In this limit, called the Bethe-Wigner limit, the rate coefficient becomes $k = 2k_{\text{L}}$.³⁴ At low collision energies, the rotational motion of the neutral molecule with rotational quantum number j must also be considered. Homonuclear diatomic molecules do not have a permanent dipole moment but a quadrupole moment. For $j \geq 1$ it interacts with the charge leading to an additional anisotropic term in the interaction potential which favors the collisions of H_2 molecules approaching the H_2^+ ions in a helicopter-like motion ($|m_j| = 1$) over collisions of H_2 molecules approaching H_2^+ ions in a cartwheeling motion ($|m_j| = 0$).

II. EXPERIMENTAL METHODS AND RESULTS

To study the $\text{H}_2 + \text{H}_2^+ \rightarrow \text{H}_3^+ + \text{H}$ reaction at low temperatures we substitute the H_2^+ reactant by an H_2^* molecule excited to a high Rydberg state ($n \geq 20$). The reaction is thus observed within the orbit of a Rydberg electron, which effectively shields against stray fields without significantly influencing the reaction.⁵ An additional feature is the possibility to manipulate Rydberg molecules with inhomogeneous electric fields \vec{E} by exploiting their large dipole moments. We use molecules in low-field seeking states with Stark energy $E_S = \frac{3}{2}a_0 e k n |\vec{E}|$ ($k \approx n$) which experience a force towards the low electric-field region:⁶ $\vec{F} = -\nabla E_S = -\frac{3}{2}a_0 e k n \nabla |\vec{E}|$, and load them in tubular electric traps generated by

applying suitable potentials to electrodes on a printed circuit board (PCB). By modulating the potentials in time, these traps are moved above the PCB. By bending the PCB, the Rydberg molecules can be deflected. The Rydberg-Stark deflector is the core component to realise our merged-beam approach (Fig. 1). Two supersonic beams are emitted by liquid-nitrogen-cooled pulsed supersonic valves. Molecules in one beam are excited to Rydberg-Stark states, deflected and merged with the other beam. The collision energy, determined by the rel-

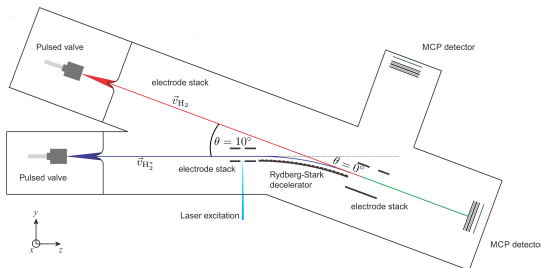


FIG. 1: Schematic representation of the experimental setup. The apparatus consists of a differential pumped beam-source chambers, the Rydberg-Stark decelerator and a reaction chamber with a time-of-flight mass spectrometer.

ative velocity of both reactants, can be tuned by changing the temperature of the supersonic valves or by acceleration/deceleration during deflection. We measure the relative cross section by recording the H_3^+ ion yield as a function of the collision energy. For normalisation, the number of H_2^* molecules is monitored by pulsed-field ionization. The density of H_2 ground-state molecules is determined by electron-impact ionization. As the measured H_3^+ yield strongly depends on the overlap of the distributions of the H_2^* and H_2 beams in the reaction region (and on the detection efficiencies) the expected signal is obtained from Monte-Carlo simulation of the full reaction and detection process and compared to the raw data. The comparison of data obtained by simulation to the measured data demonstrated that Langevin behaviour is valid in a range between 5-60 K. At lower collision energies an increase of 20 % of the rate coefficient is observed⁷ (Fig. 2). The comparison with the theoretical predictions enables us to attribute this increase to the contributions of *ortho*- H_2 ($j = 1$) molecules, which form 75 % of the beam. At present, lower collision energies cannot be reached because of the distribution of

relative velocities, which correspond to 300 mK. At this collision-energy resolution, the predicted modulations of the rate coefficient were not observable yet. Measurements of the H_3^+ ion yield at different principal quantum numbers $n = 24 - 35$ demonstrated that the Rydberg electron has no influence on the reaction.

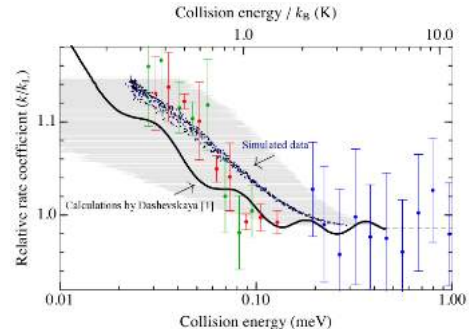


FIG. 2: Comparison of the energy dependence of the measured rate constants $\frac{k}{k_L}$ for a natural mixture of *para*- and *ortho*- H_2 to calculations of Dashevskaya *et al.*⁴ for different sets of measurements.

III. CONCLUSIONS AND OUTLOOK

We demonstrated the possibility to observe ion-molecule reactions within the Rydberg orbit in a merged beam approach. Our measurements verify the assumption of classical Langevin capture model behaviour of the reaction $\text{H}_2 + \text{H}_2^+ \rightarrow \text{H}_3^+ + \text{H}$ in a range between 5-60 K. At lower temperatures a deviation caused by ion-quadrupole interaction was observed, validating recent theoretical models. As theoretical predicted modulations in the rate coefficient could not be observed yet, the experimental energy resolution has to be increased. We expect further insights by studying other reactions. For the isotopic reaction $\text{D}_2 + \text{H}_2^+$, the deviation from classical behaviour should occur at much lower temperatures because of the larger reduced mass. Substituting the natural H_2 mixture by pure *para*- H_2 should reveal only partial wave effects while substituting the neutral H_2 by HD that has a permanent dipole moment allows to study the effect of ion-dipole interaction. The broad applicability of our experimental apparatus also allows us to study reactions as $\text{H} + \text{H}_2^+$, $\text{Ar} + \text{H}_2^+$, $\text{Ne} + \text{H}_2^+$ or $\text{He} + \text{H}_2^+$ where resonances are expected to be present.

This work is supported by QSIT, the SNSF and the ERC.

¹ T. Oka, Chem. Rev. **113**, 8738 (2013).

² T. Glenewinkel-Meyer and D. Gerlich, Isr. J. Chem. **37**, 343 (1997).

³ B. Gao, Phys. Rev. A **83**, 062712 (2011).

⁴ E. I. Dashevskaya, I. Litvin, E. E. Nikitin, and J. Troe, The Journal of Chemical Physics **145**, 244315 (2016).

⁵ P. Allmendinger, J. Deiglmayr, O. Schullian, K. Höveler, J. A. Agner, H. Schmutz, and F. Merkt, ChemPhysChem

17, 3596 (2016).

⁶ E. Vliegen, H. J. Wörner, T. P. Softley, and F. Merkt, Phys. Rev. Lett. **92**, 033005 (2004).

⁷ P. Allmendinger, J. Deiglmayr, O. Schullian, K. Höveler, J. A. Agner, H. Schmutz, and F. Merkt, J. Chem. Phys. **145**, 244316 (2016).

Scaling up a superconducting qubit quantum computer architecture

Ants Remm,¹ Christian Kraglund Andersen,¹ Johannes Heinsoo,¹ and Andreas Wallraff¹

¹*Department of Physics, ETH Zurich, CH-8093 Zurich, Switzerland*

In moving towards scalable architectures of superconducting qubit circuits, several problems have to be overcome. We look at reducing the amount of hardware required using multiplexed readout and improving the classical control software to gain more flexibility in running big experiments. Our group is developing an 8-qubit chip that will be read out using a single instrument containing 2 ADC and 2 DAC channels. At the same time we are transitioning to a new software package in Python that handles all aspects of controlling the experiment.

I. INTRODUCTION

Recent progress in superconducting qubit fabrication and control systems has allowed excellent results using a few qubits in the circuit quantum electrodynamics setting. For example qubit readout¹ and control² fidelities above the threshold required for combining physical qubits together as one logical qubit using error correcting codes have been demonstrated.

To implement a large-scale quantum algorithm finding the prime factors of numbers of length 2000 bits for example, millions of physical qubits³ have to be controlled in a coordinated fashion. To make it feasible to build such a big quantum device, it is important that the amount of classical control infrastructure scales well with the size of the quantum circuit. This is a complex problem that is actively studied from different aspects^{4,5}.

Current efforts in our group are to reduce the amount of microwave hardware required to read out the state of multiple qubits by using frequency-division multiplexed readout (section II) and to move from a control software set-up using a collection of LabVIEW virtual instruments and Mathematica to a more easily extensible control software package implemented in Python (section III).

II. MULTIPLEXED READOUT

In the circuit quantum electrodynamics architecture qubits are read out by measuring the transmittance or reflectance of a microwave resonator that is strongly and dispersively coupled to the qubit and whose resonance frequency depends on the state of the qubit⁶. To determine the state of multiple qubits, one has to generate and measure a microwave signal for each one. The naive solution is to have a separate signal generation and detection instruments for each qubit. A more hardware-efficient solution, called frequency-division multiplexing, is to generate a multi-tone baseband signal using a fast DAC and up-convert it to the frequency range required for qubit readout using an IQ mixer (see FIG. 1a). The multi-tone signal is fed through a feed-line that is coupled to each of the readout resonators. The transmitted signal is then down-converted and digitized using a fast ADC. The digitized signal can be analysed to extract the amplitude and phase of each of the readout tones.

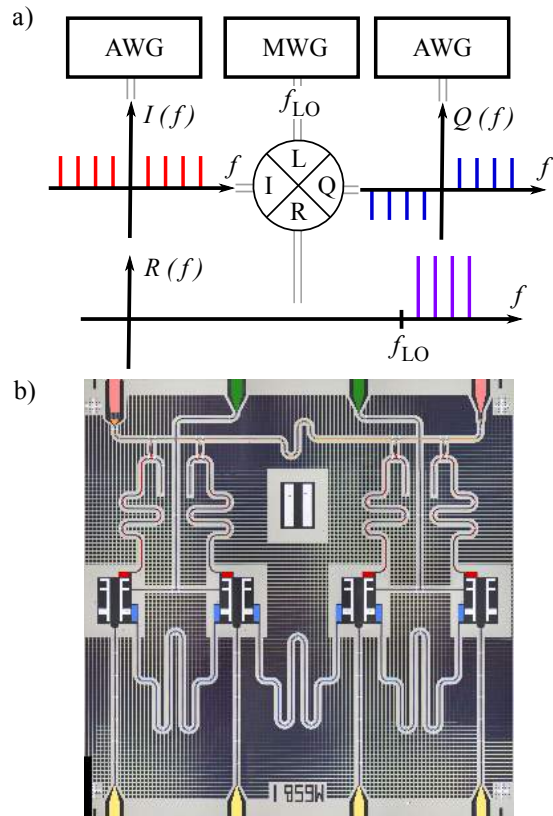


FIG. 1: a) A simplified schema showing the spectrum of the signals involved in generating a probe signal for reading out 4 qubits. b) A false colour image of a sample with the read-out resonators (red) of 4 superconducting qubits coupled to a single feed-line (pink).

Multiplexed readout scheme has already been demonstrated⁷, but the current challenge lies in achieving fast readout times without compromising qubit lifetimes. One also needs to reduce crosstalk between qubits to a minimum: the result of reading out one qubit should be independent of the states of the others which should remain unchanged.

In our group we have fabricated and successfully used a chip with 4 qubits and readout resonators coupled to a common feed-line (see FIG. 1b). An 8-qubit chip that is going to be read out using a single Zurich Instruments UHFLI instrument is currently being developed.

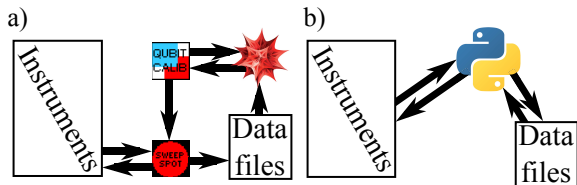


FIG. 2: The a) old and b) new software framework with arrows depicting data flow

III. CLASSICAL CONTROL SOFTWARE

Most measurements with a few qubits usually follow a similar pattern. One chooses some software parameters (value updated immediately by the control computer) to sweep over or uploads lists of waveforms to AWGs where some hardware parameter (values preprogrammed to the hardware before starting the measurement) is varied from waveform to waveform. Data is acquired by an ADC, pre-processed in a FPGA and then transmitted to the computer. The preprocessing can include integrating signals over time, averaging over many runs or histogramming the integrated results. The computer then analyses the data and extracts the relevant quantities.

For this purpose LabVIEW software packages called SweepSpot and QubitCalib were developed in our group. SweepSpot handles the communication with the instruments, setting the correct parameter values for each sweep point. In QubitCalib sequences of different measurements can be loaded as external Mathematica scripts that generate AWG waveforms and analyse the results.

This set-up has worked well with our needs so far, but scaling up places new requirements for the flexibility of the control software. For example we would like to have

modular and reusable code for programming the AWG waveforms, as we might want to use parts of a chip for different experiments at the same time.

To maintain flexibility while the number of qubits is increasing, our group is testing a Python software package PycQED⁸. Although PycQED is still being actively developed to increase the ease of use and the choice of available experiments, it has the potential to scale better than a solution based on a combination of different LabVIEW interfaces and Mathematica. This is also why we are implementing multiplexed readout code in Python. A simple comparison between the old and the new software framework is shown in FIG. 2.

IV. OUTLOOK

Superconducting qubits are one of the most promising candidates for building a large scale general purpose quantum computer. On the road to achieving this, reducing the amount of readout hardware and improving the classical control software framework are small, but necessary steps. With these tasks behind us, we can move towards fabricating a superconducting chip containing tens of qubits and demonstrating error correcting codes or quantum supremacy over classical computation.

Acknowledgments

We acknowledge financial support from the NCCR QSIT, from the IARPA, from Skype and HITSA and from ETH Zurich.

¹ T. Walter, P. Kurpiers, S. Gasparinetti, P. Magnard, A. Potocnik, Y. Salathe, M. Pechal, M. Mondal, M. Oppliger, C. Eichler, et al., *Realizing rapid, high-fidelity, single-shot dispersive readout of superconducting qubits*, arXiv:1701.06933 (2017), URL <https://arxiv.org/abs/1701.06933>.

² M. A. Rol, C. C. Bultink, T. E. O'Brien, S. R. de Jong, L. S. Theis, X. Fu, F. Luthi, R. F. L. Vermeulen, J. C. de Sterke, A. Bruno, et al., *Restless tuneup of high-fidelity qubit gates*, arXiv:1611.04815 (2016), 1611.04815, URL <https://arxiv.org/abs/1611.04815>.

³ A. G. Fowler, M. Mariantoni, J. M. Martinis, and A. N. Cleland, *Surface codes: Towards practical large-scale quantum computation*, Phys. Rev. A **86**, 032324 (2012), URL <http://link.aps.org/doi/10.1103/PhysRevA.86.032324>.

⁴ R. Versluis, S. Poletto, N. Khammassi, N. Haider, D. J. Michalak, A. Bruno, K. Bertels, and L. DiCarlo, *Scalable quantum circuit and control for a superconducting surface code*, arXiv:1612.08208 (2016), URL <https://arxiv.org/abs/1612.08208>.

⁵ S. Asaad, C. Dickel, N. K. Langford, S. Poletto, A. Bruno,

M. A. Rol, D. Deurloo, and L. DiCarlo, *Independent, extensible control of same-frequency superconducting qubits by selective broadcasting*, Npj Quantum Information **2**, 16029 (2016), URL <http://dx.doi.org/10.1038/npjqi.2016.29>.

⁶ A. Blais, R.-S. Huang, A. Wallraff, S. M. Girvin, and R. J. Schoelkopf, *Cavity quantum electrodynamics for superconducting electrical circuits: An architecture for quantum computation*, Phys. Rev. A **69**, 062320 (2004), URL <https://link.aps.org/doi/10.1103/PhysRevA.69.062320>.

⁷ M. Jerger, S. Poletto, P. Macha, U. Hbner, E. Ilichev, and A. V. Ustinov, *Frequency division multiplexing readout and simultaneous manipulation of an array of flux qubits*, Applied Physics Letters **101**, 042604 (2012), <http://dx.doi.org/10.1063/1.4739454>, URL <http://dx.doi.org/10.1063/1.4739454>.

⁸ M. Rol, C. Dickel, S. Asaad, N. Langford, C. Bultink, R. Sagastizabal, N. Langford, G. de Lange, X. Fu, S. de Jong, et al., *DiCarloLab-Delft/PycQED-py3: Initial public release* (2016), URL <https://doi.org/10.5281/zenodo.160327>.

EPR steering in a Bose Einstein Condensate

Boris Décamps,¹ Matteo Fadel,¹ Tilman Zibold,¹ and Philipp Treutlein¹

¹*Quantum Atom Optics Laboratory, Department of Physics,
University of Basel, Klingelbergstrasse 82, 4056 Basel, Switzerland*

Many-body entanglement is an active field of research due to both its fundamental aspects and its potential applications in quantum communications and in metrology. We study entanglement properties between spatially separated spin regions in a ⁸⁷Rb Bose-Einstein condensate. We observe strong correlations between them which violate the EPR steering criterion^{1,2}. Hence, we both show that the underlying correlations are strong enough to demonstrate the EPR paradox and that the distributed entanglement can be converted into a useful entanglement between distinct spatial regions.

I. INTRODUCTION

From the original discussion on the Einstein-Podolsky-Rosen (EPR) paradox³, various form of correlations have been introduced. In particular, the non separability of a state defines its entanglement which is not only useful for quantum communication and metrology but also a necessary condition for even stronger correlations, such as EPR or Bell correlations.. One of the most striking feature of these correlations is revealed when a quantum state is split between two spatially separated regions A and B. As introduced by Schrödinger⁴, upon measurements on the A region, the quantum state in the B regions gets steered. This implies that the information on the measurement result in A is sufficient to accurately predict the result of a measurement in B even in the absence of classical communication channels. This type of predictions are in direct contradiction with local causality which is at the core of the EPR paradox.

II. EPR STEERING CRITERIA

In a spin framework, one² can express a criterion which cannot be violated in any local description of reality. It takes the form:

$$\mathcal{E}_{EPR}^{A \rightarrow B} := \frac{4\Delta^2 \left(\hat{S}_z^B + g_z \hat{S}_z^A \right) \Delta^2 \left(\hat{S}_y^B + g_y \hat{S}_y^A \right)}{\left| \langle \hat{S}_x \rangle \right|^2} \geq 1 \quad (1)$$

where $(\hat{S}_x^\alpha, \hat{S}_y^\alpha, \hat{S}_z^\alpha)$ are the three spin quadratures of parties $\alpha = \{A, B\}$, g_z , and g_y are real parameters (which can be independently optimized) and $\Delta^2(\cdot)$ refers to the variance. When $(g_i = 0)_{i=y,z}$ one recovers the Heisenberg uncertainty relation for region B. This is for example the case in a coherent spin state where there is no correlations between different spins. This criterion emphasizes how measurement results in region B are correlated with measurement results in region A. Indeed, violating ineq.(1) allows one to predict the results of non commuting variables in one region from the knowledge of the measured result in the other region. Furthermore,

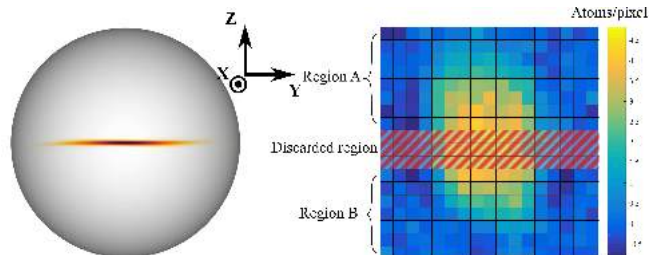


FIG. 1: Left: Wigner function of the spin-squeezed state represented on the Bloch sphere. Right: Absorption image of the atomic density in $|1\rangle$ with the regions A and B defining the two separated spins \hat{S}^A and \hat{S}^B . The discarded region in the center is made large enough (3 pixels wide) so that crosstalks between the two regions due to the imaging process is negligible.

the product of the inferred results uncertainties is smaller than the Heisenberg relation in the steered region.

Although EPR steering has already been demonstrated on optical systems^{5,6} our recent work on massive systems have shown that ineq.(1) could be violated by spatially separated spins.

III. EXPERIMENT DESCRIPTION

The starting point of our experiment is a coherent superposition of two hyperfine internal states $|1\rangle$ and $|2\rangle$, in a Bose-Einstein condensate of ⁸⁷Rb atoms produced on an atom-chip⁷. These two components occupy nearly identical spatial modes and can be effectively described as a collective spin operator \hat{S} . To generate entanglement in between our constituents, we rely on the one-axis twisting Hamiltonian, $\hat{H}_{twist} = \hbar\chi\hat{S}_z^2$, which is an often used model to study spin-squeezed states⁸. In practice, we use state dependent potentials to tune the elastic scattering interaction parameter χ to a non-zero value during a fixed duration. Then, to protect the spin squeezed state against technical phase noise, we rotate the anti-squeezed quadrature along the phase-sensitive axis (see Fig.1). This cloud of atoms is then released and let expand during a 2.2 ms time of flight at the end of which

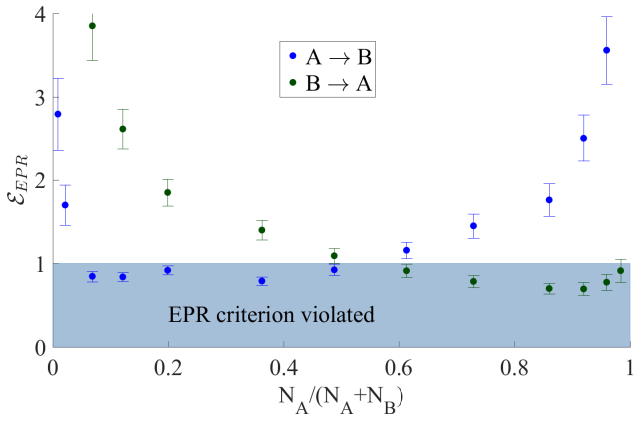


FIG. 2: EPR-steering criteria (left hand side of ineq.(1)) of a vertically split cloud as a function of the splitting ratio $N_A/(N_A + N_B)$ between the two regions. The two scenarios of A steering B ($A \rightarrow B$, blue dots) and B steering A ($B \rightarrow A$, green dots) are shown with their associated 1σ error bars. The criterion is violated (blue shaded region) for a range of splitting ratios around 0.2 and 0.8 respectively.

Rabi rotations can be applied to measure the different spin components. Finally, high resolution absorption images of the two states are taken and different spatial regions A and B, corresponding to the two parties spins, are defined for the whole data-set. In this case, the measurement of the different spin observables \hat{S}_i^α directly corresponds to half of the population difference between the two internal states counted in each regions. A special feature of this detection scheme is that the spatial regions are defined a posteriori, i.e only after the atomic position

is projected. This allows us to define arbitrary spatial patterns but for conciseness, only the one presented on Fig.1 will be discussed.

IV. RESULTS

On Fig.2 we show that the EPR steering inequality is violated in our system for different relative total number of atoms in region A with respect to the total atom number in both regions: $N_A/(N_A + N_B)$. To scan this parameter we change the position of the discarded region which changes the size of the two regions. Furthermore, we observe that both regions can be steered, i.e $\mathcal{E}_{EPR}^{A \rightarrow B} < 1$ and $\mathcal{E}_{EPR}^{B \rightarrow A} < 1$, but for different positions of the discarded region. This asymmetry is probably due to inhomogeneous noise on the absorption images on which we have identified an imaging intensity gradient. This is similar to quantum optics experiments where it has been shown that in the presence of technical noise, an asymmetric splitting is favorable⁹.

V. CONCLUSION

We have shown non-local correlations between spatially separated regions of a many particle massive system. This un-intuitive feature not only provides stringent test to quantum mechanics but it could also be used to measure with increased sensitivity spatially dependent quantities such as electromagnetic field gradients or higher multi-polar moments.

¹ H. M. Wiseman, S. J. Jones, and A. C. Doherty, *Steering, Entanglement, Nonlocality, and the Einstein-Podolsky-Rosen Paradox*, Physical Review Letters **98**, 140402 (2007).
² M. D. Reid, P. D. Drummond, W. P. Bowen, E. G. Cavalcanti, P. K. Lam, H. A. Bachor, U. L. Andersen, and G. Leuchs, *Colloquium*, Reviews of Modern Physics **81**, 1727 (2009).
³ A. Einstein, B. Podolsky, and N. Rosen, *Can Quantum-Mechanical Description of Physical Reality Be Considered Complete?*, Physical Review **47**, 777 (1935).
⁴ E. Schrödinger, *Discussion of Probability Relations between Separated Systems*, Mathematical Proceedings of the Cambridge Philosophical Society **31**, 555 (1935), ISSN 1469-8064, 0305-0041.
⁵ D. J. Saunders, S. J. Jones, H. M. Wiseman, and G. J. Pryde, *Experimental EPR-steering using Bell-local states*, Nature Physics **6**, 845 (2010), ISSN 1745-2473.

⁶ B. Wittmann, S. Ramelow, F. Steinlechner, N. K. Langford, N. Brunner, H. M. Wiseman, R. Ursin, and A. Zeilinger, *Loophole-free Einstein-Podolsky-Rosen experiment via quantum steering*, New Journal of Physics **14**, 053030 (2012), ISSN 1367-2630.
⁷ J. Reichel and V. Vuletic, eds., *Atom Chips* (Wiley-VCH, 2011), 1st ed., ISBN 978-3-527-40755-2.
⁸ L. Pezz, A. Smerzi, M. K. Oberthaler, R. Schmied, and P. Treutlein, *Non-classical states of atomic ensembles: fundamentals and applications in quantum metrology*, arXiv:1609.01609 [quant-ph] (2016), arXiv: 1609.01609.
⁹ K. Wagner, J. Janousek, S. Armstrong, J.-F. Morizur, P. K. Lam, and H.-A. Bachor, *Asymmetric EPR entanglement in continuous variable systems*, Journal of Physics B: Atomic, Molecular and Optical Physics **47**, 225502 (2014), ISSN 0953-4075.

Realization of an atomically thin mirror using monolayer MoSe₂

Aroosa Ijaz,¹ Patrick Back,¹ Sina Zeytinoglu,¹ Martin Kroner,¹ Atac Imamoglu¹

¹*Institute of Quantum Electronics, ETH-Hönggerberg, CH-8093, Zürich, Switzerland*

We were able to show upto 90% extinction of an incident field that is resonant with the exciton transition in a single monolayer of MoSe₂. The corresponding reflection coefficient was found to be 45% which is only limited by the decay rates and sample quality. Additionally, this monolayer is embedded in a charge controlled heterostructure that can be used to realize an electrically tunable atomically-thin mirror. This paves way to applications such as fast programmable spatial light modulators, chiral mirrors, suspended ultra-light mirrors for optomechanical devices and many more.

I. INTRODUCTION

Transition Metal Dichalcogenides (TMDs) have recently gained a lot of interest in multiple research areas in physics including solid state physics and quantum information processing. It basically constitutes of a transition metal atom chemically bonded to two chalcogen atoms (S, Se) in a hexagonal lattice structure. Interestingly, when stripped down to a monolayer, the material exhibits a direct band gap. This occurs at the K points at the edge of the Brillouin zone (usually termed K and -K valleys). Consequently, the time reversal symmetry is broken. The 2D geometry also gives rise to valley dependent selection rules and large exciton binding energies; ~ 0.5 eV¹. Exciton line widths

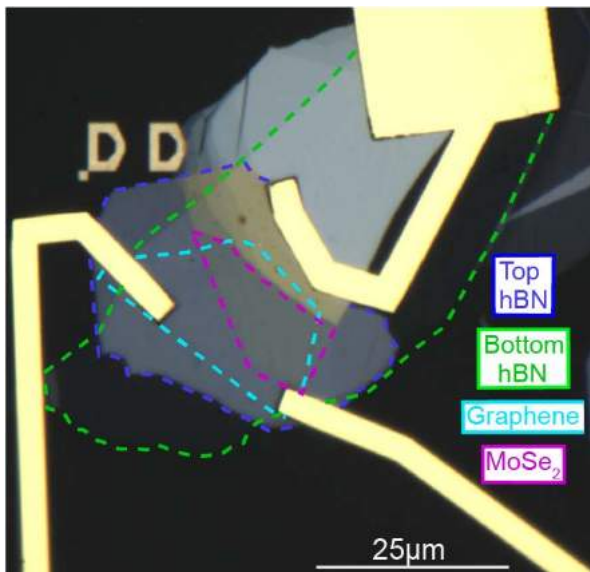


FIG. 1: Micograph of the sample used. A MoSe₂ monolayer is encapsulated in between 33 nm (top) and 7 nm (bottom) thick hBN layers, which are indicated by blue and green dashed lines. To allow for optical transmission measurements the heterostructure is transferred on to a transparent 500 μ m thick fused-silica substrate. To achieve charge control of the MoSe₂, the heterostructure is capped by a graphene bilayer. The graphene and the MoSe₂ are electrically contacted by titanium/gold electrodes.

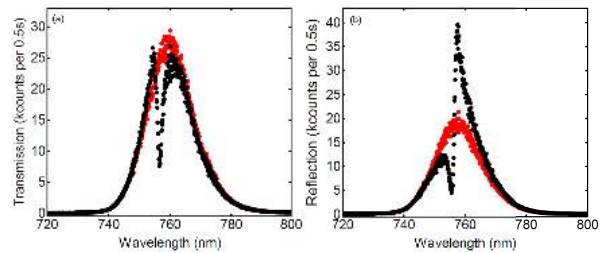


FIG. 2: Transmission and Reflection spectra on (black) and off (red) the flake.

have been reported to be as narrow as 2meV² and dominantly radiative³.

Generally in transmission experiments, when considering a single emitter, extinction refers to the destructive interference between the incident light field (nearly resonant and weak) and the coherent resonance fluorescence from the emitter. When seen in reflection, the interference can look complicated due to system dependent phase differences that fluorescence might acquire with respect to the incident field. Recently, in a theoretical study, we showed that a monolayer TMD material can act as a perfect mirror given weak resonant excitation, fourier-limited exciton line widths and perfect light-dipole coupling⁴. This is true irrespective of the polarization and incidence angle of the incident field due to the two dimensional geometry of our system. Here, we show the experimental realization of that hypothesis.

II. EXPERIMENTAL RESULTS

The sample was prepared by the dry transfer method where a single exfoliated layer of MoSe₂ is sandwiched between two few-layers thick hexa Boron Nitride (hBN). This encapsulation helps improve the optical properties of the TMDs⁵ and reduces the exciton binding energy⁶. The charge environment was tuned using electrical contacts shown in Figure 1.

Both reflection and transmission measurements were carried out in a confocal microscope setup using a special

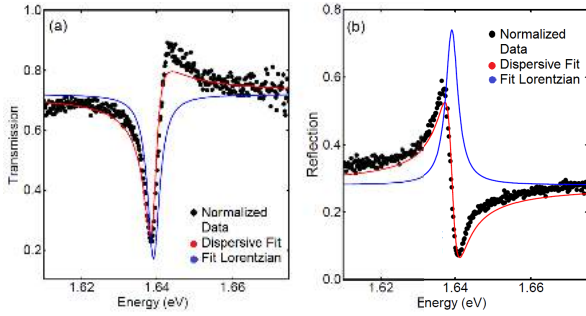


FIG. 3: Normalized spectra and their corresponding Lorentzian fits revealing $\Gamma_{tot} = 3.6meV$.

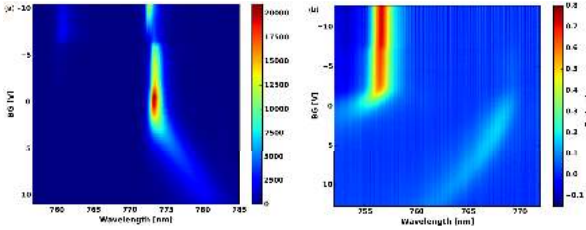


FIG. 4: (a) PL spectra obtained with a 714nm excitation from the sample as the gate voltage is varied. As the electron density is increased, attractive exciton-polaron appears. (b) The corresponding extinction plot showing transfer of oscillator strength as gate voltage is varied.

cryostat with free space optical front and back access. For the excitation, we used either a broad band light emitting diode (LED) centered at 780nm or a tunable single-mode Ti:S laser. To detect photons with nearly zero in-plane momentum, iris were used in detection paths to reduce effective NAs. Due to losses on the windows of the cryostat and the finite coupling/detection efficiency we could not directly measure the absolute reflected and transmitted power. Instead, we used a reference reflection and transmission spectrum of the incident light by moving our excitation spot off the MoSe₂ layer. The spectra at one particular spot on the

sample are shown in Figure 2.

The off-monolayer spectra were used to normalize the data which were then fit with dispersive Lorentzian models as shown in Figure 3. The fits yielded an extinction coefficient of 0.76 ± 0.15 , a reflection coefficient of 0.46 ± 0.09 and $\Gamma_{tot} = 3.6meV$. Across the sample, there was a large variation in exciton resonance wavelength, linewidth and extinction coefficient. This comes from the local variation of impurity and strain profiles. The largest extinction was measured to be 90%. Repeating the measurements at different areas in the sample yielded a radiative decay rate in the range $1.4meV-1.8meV$ which is in good agreement with existing literature³.

When the charge density was changed, the oscillator strength shifted to the attractive exciton-polaron⁵ as shown in Figure 4. In the context of our work, the gate voltage dependence of the optical response of the MoSe₂ monolayer indicates that the atomically-thin mirror can be electrically tuned. This work has been submitted to Science and is currently under peer review.

III. OUTLOOK

Our further experiments include: polarization dependent measurements to establish how good of a chiral mirror can be obtained from monolayer MoSe₂. Additionally, magnetic fields can be applied to lift the k and -k valley spin degeneracy and hence exclude any valley exchange inhomogeneous broadening effects.

Acknowledgments

This work is supported by an ERC Advanced investigator grant (POLTDES), Spin-NANO Marie Skłodowska-Curie Grant Agreement No. 676108 and NCCR QSIT.

¹ A. Chernikov, T. C. Berkelbach, H. M. Hill, A. Rigosi, Y. Li, O. B. Aslan, D. R. Reichman, M. S. Hybertsen, and T. F. Heinz, *Exciton binding energy and nonhydrogenic rydberg series in monolayer WS₂*, Phys. Rev. Lett. **113**, 076802 (2014), URL <http://link.aps.org/doi/10.1103/PhysRevLett.113.076802>.
² F. Cadiz, E. Courtade, C. Robert, G. Wang, Y. Shen, H. Cai, T. Taniguchi, K. Watanabe, H. Carrere, D. Lagarde, et al., *Excitonic linewidth approaching the homogeneous limit in mos2 based van der waals heterostructures : accessing spin-valley dynamics*, arXiv **1702.00323** (2017), 1702.00323, URL <https://arxiv.org/abs/1702.00323>.
³ M. Sidler, P. Back, O. Cotlet, A. Srivastava, T. Fink, M. Kroner, E. Demler, and A. Imamoglu, *Fermi polaron-polaritons in charge-tunable atomically thin semiconduc-*

tors, Nat. Phys. **13**, 255 (2017), ISSN 1745-2473, URL <http://dx.doi.org/10.1038/nphys3949>.

⁴ S. Zeytinoglu, C. Roth, S. Huber, and A. Imamoglu, *Atomically thin semiconductors as nonlinear mirrors*, arXiv **1701.08228** (2017), URL <https://arxiv.org/abs/1701.08228>.

⁵ P. Back, M. Sidler, O. Cotlet, A. Srivastava, N. Take-mura, M. Kroner, and A. Imamoglu, *Giant paramagnetism induced valley polarization of electrons in charge-tunable monolayer mose2*, arXiv **1701.01964** (2017), URL <https://arxiv.org/abs/1701.01964>.

⁶ S. Latini, T. Olsen, and K. S. Thygesen, *Excitons in van der waals heterostructures: The important role of dielectric screening*, Phys. Rev. B **92**, 245123 (2015), URL <https://link.aps.org/doi/10.1103/PhysRevB.92.245123>.